Localization and Mitigation of Radio Frequency Interference for Interferometric Arrays

by

Jan-Willem W. Steeb

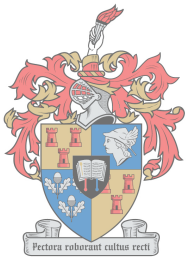

Dissertation presented for the degree of Doctor of Philosophy (Electronic Engineering) in the Faculty of Engineering at Stellenbosch University

Supervisor: Prof. David B. Davidson

Co-supervisor: Prof. Stefan J. Wijnholds

December 2018

The financial assistance of the National Research Foundation (NRF) and the South African Radio Astronomy Observatory (SARAO) towards this research is hereby acknowledged. Opinions expressed and conclusions arrived at, are those of the author and are not necessarily to be attributed to the NRF or SARAO.

Declaration

By submitting this dissertation electronically, I declare that the entirety of the work contained therein is my own, original work, that I am the sole author thereof (save to the extent explicitly otherwise stated), that reproduction and publication thereof by Stellenbosch University will not infringe any third party rights and that I have not previously in its entirety or in part submitted it for obtaining any qualification.

This dissertation includes three original papers published in peer reviewed journals or conference proceedings and two submitted, but not yet published, papers. The development and writing of the papers (published and unpublished) were the principal responsibility of myself and, for each of the cases where this is not the case, a declaration is included in the dissertation indicating the nature and extent of the contributions of co-authors

Date: December 2018 .....

Abstract

Localization and Mitigation of Radio Frequency Interference for Interferometric Arrays

J. W. Steeb

Department of Electrical and Electronic Engineering,
University of Stellenbosch,
Private Bag X1, Matieland 7602, South Africa.

Dissertation: PhD (Eng)

December 2018

Radio telescopes have increased exponentially in sensitivity ever since the first single dish radio telescopes were built in the 1930's. This trend continues with the development of next generation telescopes such as the Square Kilometre Array (SKA). Parallel to the development of radio telescopes, has been the rapid expansion of telecommunication technologies. Consequently, radio telescopes are becoming more sensitive in an environment with ever increasing radio frequency interference (RFI).

The ideal solution to RFI that is detected by a radio telescope is to locate its source and then have it removed. Removal of the source is usually only possible if it is occurring in a protected band or the radio telescope is in a radio quiet zone. Unfortunately, most of the radio spectrum has been allocated to active communication services and not all radio telescopes are in radio quiet zones. The alternative is to mitigate its effect using methods such as spatial RFI mitigation. The contributions of this PhD dissertation are twofold: firstly, a source localization algorithm that takes into account the constraints and advantages of the arrays used for radio astronomy has been developed; and secondly, existing spatial RFI mitigation techniques have been adapted to take into account the bandwidth of the RFI signals.

The computationally efficient localization algorithm that was developed is best suited for interferometric arrays with low array beam sidelobes. Two variants of the algorithm were developed, one that works for sources in the near-field and the other for far-field sources. In the near-field, the computational complexity of the algorithm is linear with search grid size compared to cubic scaling of the state-of-the-art 3-D MUSIC method. The trade-off is that

the proposed algorithm requires a once-off a priori calculation and storing of weighting matrices. In an experiment using a station of the Low Frequency Array (LOFAR) a hexacopter was flown around the array, at a mean radial distance of 190 m, broadcasting a signal. The mean error in distance between the estimated position of the hexacopter and the GPS position of the hexacopter was 2 m for a wavelength of 6.7 m.

The non-narrowband RFI mitigation method developed consists of a second order filter that is used to mitigate powerful RFI with bandwidth sufficient to cause aberrations that are below the noise, but with power that competes with the astronomical sources. The second order filter consists of a first order subspace subtraction filter combined with a flat frequency response model for the RFI source. Taking into account mutual coupling as well as a calibration step to account for unknown complex gains, the algorithm was found to process approximately 1.6 times more bandwidth than using just a first order subspace subtraction filter.

Uittreksel

Lokalisering en Mitigasie van Radiofrekwensie-inmenging vir Interferometriese Skikkings

("Localization and Mitigation of Radio Frequency Interference for Interferometric Arrays")

J. W. Steeb

Departement Elektriese en Elektroniese Ingenieurswese,
Universiteit van Stellenbosch,
Privaatsak X1, Matieland 7602, Suid Afrika.

Proefskrif: PhD (Ing)

Desember 2018

Sedert die eerste enkelskottel radioteleskope in die 1930's gebou is, het die sensitiwiteit van radioteleskope eksponensieël toegeneem. Hierdie tendens gaan voort met die ontwikkeling van volgende generasie teleskope, soos byvoorbeeld die Square Kilometer Array (SKA). In parallel met die ontwikkeling van radioteleskope, het telekommunikasietegnologieë ook vinnig uitgebrei. Gevolglik word radioteleskope meer sensitief in 'n omgewing met toenemende radiofrekwensie-inmenging (RFI).

Die optimale oplossing vir RFI is om die bron daarvan op te spoor en te verwyder. Verwydering van die bron is gewoonlik net moontlik as dit teenwoording is in 'n beskermde band of as die radio teleskoop in 'n radio-stil gebied is. Ongelukkig is meeste van die radio spectrum toegeken aan kommunikasiedienste en nie alle radio teleskope is in radio-stil gebiede nie. Die alternatief om die effek daarvan te mitigeer deur middel van metodes soos ruimtelike RFI-mitigasie. Die bydraes van hierdie doktorale proefskrif is tweeledig: eerstens, die ontwikkeling van 'n bronlokaliseringsalgoritme wat die beperkings en voordele van die skikkings wat gebruik word vir radio astronomie in ag neem en tweedens, die aanpassing van bestaande ruimtelike RFI mitigeringstegnieke om die bandwydte van die RFI seine in ag te neem.

Die berekeningsdoeltreffende lokaliseringsalgoritme wat ontwikkel is, is die beste geskik vir interferometriese skikkings met lae samestelling-bundel sylobbe. Twee weergawes van die algoritme is ontwikkel, die eerste hanteer bronne in die nabyveld en die ander hanteer vêrveld bronne. In die nabyveld

is die berekeningskompleksiteit van die algoritme lineêr met soektogroostergrootte in vergelyking met die kubieke skalering van die 3-D MUSIC-metode. Die nadeel is dat die voorgestelde algoritme 'n eenmalige a priori berekening en stoor van gewigsmatrikse vereis. In 'n eksperiment by 'n stasie van die Low Frequency Array (LOFAR), het 'n heksakopter oor die skikking gevlieg met 'n gemiddelde radiale afstand van 190 m en 'n sein uitgesaai. Die gemiddelde fout in die afstand tussen die beraamde posisie van die heksakopter en die GPS-posisie van die heksakopter was 2 m vir 'n golflengte van 6.7 m.

Die nie-smalband RFI mitigasie metode wat ontwikkel is, fasiliteer die definieering van 'n tweede-orde filter wat gebruik word om kragtige RFI met bandwydte verwante krag onder die geruis, maar met krag wat met die astronomiese bronne kompeteer, te mitigeer. Die tweede order filter bestaan uit 'n eerste orde subruimte verminderingsfilter gekombineer met 'n plat frekwensie responsmodel vir die RFI bron. Met inagneming van wedersydse koppeling asook 'n kalibrasie stap om vir onbekende komplekse antenna aanwinste voorsiening te maak, is gevind dat die algoritme ongeveer 1.6 meer bandwydte kan verwerk as 'n eerste orde subruimte verminderingsfiter.

Acknowledgements

I wish to express my sincere gratitude to Prof. David B. Davidson[1] and Prof. Stefan J. Wijnholds[2]. I have learned a great deal from them during our bi-weekly tri-continental Skype meetings. Their guidance as to which topics to explore as well as where to obtain data was indispensable.

I am grateful for the funding provided by the South African Radio Astronomy Observatory (SARAO), the National Research Foundation of South Africa (NRF) and the Netherlands Organisation for Scientific Research (NWO). Part of this funding enabled me to travel to the Netherlands and collaborate with other scientists and engineers at the Netherlands Institute for Radio Astronomy (ASTRON). In particular, I would like to thank Mr. Menno Norden and Dr. Michiel Brentjens for providing me with radio telescope array data and helping me understand the effects of radio frequency interference on this data. I also appreciate the assistance I received from Dr. Ahmad Sardarabadi regarding factor analysis.

Finally, I am eternally indebted to my parents for their continued support.

[1]Director of Engineering at the International Centre for Radio Astronomy Research (ICRAR), Curtin University in Australia and Professor Extraordinary at Stellenbosch University.

[2]Researcher at the Netherlands Institute for Radio Astronomy (ASTRON), The Netherlands and Associate Professor Extraordinary at Stellenbosch University.

Dedications

Hierdie tesis word opgedra aan my geliefde moeder, Retha.

Contents

Nomenclature

Constants

$\mathrm{c} =$	299792458 m/s
$i =$	$\sqrt{-1}$

Variables

l, m, j, k	Counters and indices	[ ]
$\mathrm{l}, \mathrm{m}, \mathrm{n}$	Directional cosines	[ ]
x, y, z	Cartesian coordinates	[m]

Vectors and Matrices

a	Lower-case letters are scalars
$\mathbf{a}$	Bold lower-case letters are column vectors
$\mathbf{A}$	Bold upper-case letters are matrices
$\mathbf{I}$	Identity matrix
$\mathbf{R}$	Covariance matrix
$\mathbf{B}$	Covariance matrix with no time delay effect
$\mathbf{D}$	Diagonal covariance matrix (signals are uncorrelated)

Subscripts

$\{\cdot\}_{\mathrm{r}}$	RFI (radio frequency interference)
$\{\cdot\}_{\mathrm{c}}$	Cosmic
$\{\cdot\}_{\mathrm{n}}$	Noise

Operators

$\otimes$	Kronecker product
$\odot$	Hadamard product
$\{\cdot\}^T$	Transpose of a matrix
$\{\cdot\}^H$	Hermitian transpose of a matrix
$\mathrm{diag}(\cdot)$	Converts a vector into a diagonal matrix

$\overline{\{\cdot\}}$	Complex conjugate of a scalar
$\|\| \cdot \|\|$	Euclidean norm of a vector
vec$(\cdot)$	Stack columns of a matrix to form a vector
unvec$(\cdot)$	Inverse operation of vec$(\cdot)$
median$(\cdot)$	Median value of the diagonal entries of a matrix

Chapter 1

Introduction

1.1 Overview

On 17 August 2017 the first multi-messenger observation was done of an astronomical event [1]. The gravitational waves generated by a binary neutron star merger was first detected by the LIGO-Virgo detector and, 1.7 s later, by the Fermi Gamma-ray telescope detected gamma-rays from the same location. Observations were then completed across the electromagnetic spectrum, which was made possible due to the pooling of expertise and resources worldwide. Ultimately the goal of astronomy is to chart and understand the entire history of the universe [2]. Radio astronomy forms a core part of achieving this goal. Currently, earth based radio telescopes can observe frequencies as low as 10 MHz with the Low Frequency Array (LOFAR) and as high as 950 GHz with the Atacama Large Millimeter Array (ALMA) [3; 4].

Radio Astronomy is a passive service that ideally would want access to the entire radio spectrum (3 Hz to 3 THz). However, due to the commercial value of the radio spectrum, radio astronomy has to compete for spectrum. For example, the third generation spectrum auction in Germany alone brought in € 50.8 billion for 140 MHz of spectrum [5]. Consequently, radio telescopes are built in remote areas in order to minimize radio frequency interference (RFI) and maximize the amount of bandwidth that can be used for observation. Nevertheless, RFI can still easily be detected due to the high sensitivity of the radio telescope arrays.

Radio telescope sensitivity has increased by five orders of magnitude from 1940 to 2010 [6] and the trend will continue with the Square Kilometre Array (SKA) [2]. The SKA will consist of different radio telescope arrays, each designed for a different band of the radio spectrum. Pathfinder telescopes for the SKA, such as the Netherlands' LOFAR and South Africa's MeerKAT telescope [7], have already been built. The RFI detected by LOFAR is typically 20 to 100 dB stronger than the astronomical sources being observed.

The ideal solution for RFI is to identify the emitting location and have it

switched off. An RFI signal can either be in the far-field (when only direction of arrival can be determined) or near-field (when it is possible to localize the RFI) of the array. If the RFI can not be switched off, the goal becomes to mitigate the effect of the RFI on the astronomical data. Spatial RFI mitigation techniques work by steering a null in the direction of the RFI. However, these techniques currently assume that the RFI signal is narrowband.

1.2 Background

An interferometer is an array of at least two antennas where for each antenna pair the covariance of these antennas' signals is calculated [8, p. 16-18]. The simplest case is an interferometer which consists of two antennas and the incident signal is from a far-field point source, see figure 1.1. Since the source is in the far-field, the signal approaches the array as a plane wave. The amplitude of the calculated covariance will be proportional to the source's flux density and the phase will depend on the point source's frequency and the signal delay due to the distance between the antennas. The spacings between antennas are called baselines. As baseline length increases, so does the angular resolution [9, p. 202].

There exists a three-dimensional Fourier relation between the measured covariance (also called the visibility data) and the intensity distribution on the sky [10]. By increasing the number of antennas, $N_\mathrm{b} = N_\mathrm{e}(N_\mathrm{e} - 1)/2$ baselines are formed, where N_e is the number of antennas. Each baseline then has an associated covariance or visibility. These visibilities form part of the $\mathrm{u}, \mathrm{v}, \mathrm{w}$ space where the plane u, v is normal to the direction of the phase center. Due to finite sampling of the $\mathrm{u}, \mathrm{v}, \mathrm{w}$ space, any algorithm which attempts to create an accurate image (skymap) also requires deconvolution, see for example the CLEAN algorithm [8, p. 427-432].

1.3 Phased and Interferometric Array Data Model

When a signal is detected by an antenna, that signal is a delayed version $x(t - \tau)$ of the signal at its source $x(t)$, where τ is the delay. If the array's frequency channels are sufficiently narrowband, then the time delays can be represented as phase delays. For the j^{th} antenna the delayed signal can be approximated by $x(t - \tau_j) \approx x(t)e^{-i2\pi\nu_0\tau_j}$, where ν_0 is the center frequency of the channel. This condition is satisfied if [11, p. 23]

$$2\pi\Delta\nu\tau_{\max} \ll 1, \tag{1.1}$$

where $\Delta\nu$ is the channel's bandwidth and $\tau_{\max}$ is the delay given by the longest baseline (greatest distance between any two antennas).

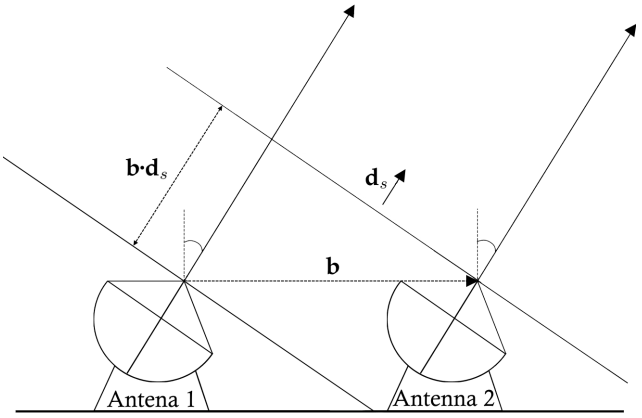

Figure 1.1: Diagram of a two element interferometer where $\mathbf{d}_s$ is the direction of arrival of a planar wavefront (far-field source), $\mathbf{b}$ is the baseline vector and $\frac{\mathbf{b}\cdot\mathbf{d}_s}{c}$ is the geometric delay (the time difference between the antennas receiving the signal).

For an array with N_e antennas the phase delays can be stacked into a vector that is called the geometric delay vector

$$\mathbf{a} = \begin{bmatrix} e^{-i2\pi\nu_0\tau_1} \\ \vdots \\ e^{-i2\pi\nu_0\tau_{N_\mathrm{e}}} \end{bmatrix}. \tag{1.2}$$

Using the geometric delay vector in equation (1.2) the following general model (used in [11–16]) will be considered for the output generated, from a single source $x(t)$ at time t, for one polarization and frequency channel:

$$\mathbf{y}(t) = \mathbf{g} \odot \mathbf{a}\, x(t) + \mathbf{x}_\mathrm{n}(t) \tag{1.3}$$

where

$$\mathbf{y}(t) = \begin{bmatrix} y_1(t) \\ \vdots \\ y_{N_\mathrm{e}}(t) \end{bmatrix} \text{ is the vector of the measured array output signals,}$$

$$\mathbf{g} = \begin{bmatrix} g_1 \\ \vdots \\ g_{N_\mathrm{e}} \end{bmatrix} \text{ is the vector of complex gains for each antenna,}$$

$$\mathbf{x}_\mathrm{n}(t) = \begin{bmatrix} x_{\mathrm{n},1}(t) \\ \vdots \\ x_{\mathrm{n},N_\mathrm{e}}(t) \end{bmatrix} \text{ is the vector of instrumental noise for each antenna.}$$

The complex gains in $\mathbf{g}$ represent the direction independent gains that are assumed to not vary for the time scales considered. Examples of direction

independent effects are path loss, the polarization mismatch factor, the gain of the antennas and atmospheric effects. Direction dependent gains will not be considered, because the non-narrowband RFI mitigation algorithm presented in sections 2.5 and 2.6 is designed to work on a single source. Furthermore, the localization algorithm in sections 2.3 and 2.4 makes use of factor analysis to separate sources.

The model in equation (1.3) can now be expanded for N_c cosmic sources and N_r RFI sources

$$\mathbf{y}(t) = \mathbf{g} \odot (\mathbf{A}_\mathrm{c}\mathbf{x}_\mathrm{c}(t) + \mathbf{A}_\mathrm{r}\mathbf{x}_\mathrm{r}(t)) + \mathbf{x}_\mathrm{n}(t), \tag{1.4}$$

where

$\mathbf{A}_\mathrm{c} = \begin{bmatrix}\mathbf{a}_{\mathrm{c},1} & \cdots & \mathbf{a}_{\mathrm{c},N_\mathrm{c}}\end{bmatrix}$ is the matrix of concatenated geometric delay vectors for the cosmic sources,

$\mathbf{x}_\mathrm{c} = \begin{bmatrix} x_{\mathrm{c},1}(t) \\ \vdots \\ x_{\mathrm{c},N_\mathrm{c}}(t)\end{bmatrix}$ is the vector of cosmic sources,

$\mathbf{A}_\mathrm{r} = \begin{bmatrix}\mathbf{a}_{\mathrm{r},1} & \cdots & \mathbf{a}_{\mathrm{r},N_\mathrm{r}}\end{bmatrix}$ is the matrix of concatenated geometric delay vectors for the RFI sources,

$\mathbf{x}_\mathrm{r}(t) = \begin{bmatrix} x_{\mathrm{r},1}(t) \\ \vdots \\ x_{\mathrm{r},N_\mathrm{r}}(t)\end{bmatrix}$ is the vector of RFI sources.

The model in equation (1.4) is valid for both phased arrays and interferometric arrays. For a phased array the signals are beamformed to simulate a single dish with larger aperture that is electronically steerable. In comparison, for an interferometric array the signals from different antennas are correlated and then used for imaging.

1.3.1 Standard Covariance Matrix Model

The zero lag covariance matrix (the jk^{th} element of the matrix is the covariance of the j^{th} and k^{th} antenna [17, p. 501]) of the vectorized data model in equation (1.4) is given by

$$\mathbf{R} = \mathbb{E}\{\mathbf{y}(t)\mathbf{y}^H(t)\}, \tag{1.5}$$

where $\mathbb{E}$ is the expectation.

Independence is assumed between the cosmic, RFI and noise sources. Therefore, when substituting equation (1.4) into equation (1.5) the expectation of

any non-self multiplication terms are zero and consequently the substitution yields

$$\begin{aligned}\mathbf{R} &= \mathbf{G}(\mathbf{R}_{\mathrm{c}} + \mathbf{R}_{\mathrm{r}})\mathbf{G}^H + \mathbf{R}_{\mathrm{n}} \\ &= \mathbf{G}(\mathbf{A}_{\mathrm{c}}\mathbf{B}_{\mathrm{c}}\mathbf{A}_{\mathrm{c}}^H + \mathbf{A}_{\mathrm{r}}\mathbf{B}_{\mathrm{r}}\mathbf{A}_{\mathrm{r}}^H)\mathbf{G}^H + \mathbf{R}_{\mathrm{n}},\end{aligned} \tag{1.6}$$

where $\mathbf{B}_{\mathrm{c}} = \mathbb{E}\{\mathbf{x}_{\mathrm{c}}(t)\mathbf{x}_{\mathrm{c}}^H(t)\}$, $\mathbf{B}_{\mathrm{r}} = \mathbb{E}\{\mathbf{x}_{\mathrm{r}}(t)\mathbf{x}_{\mathrm{r}}^H(t)\}$, $\mathbf{R}_{\mathrm{n}} = \mathbb{E}\{\mathbf{x}_{\mathrm{n}}(t)\mathbf{x}_{\mathrm{n}}^H(t)\}$, $\mathbf{G} = \mathrm{diag}(\mathbf{g})$, $\mathbf{R}_{\mathrm{c}} = \mathbf{A}_{\mathrm{c}}\mathbf{B}_{\mathrm{c}}\mathbf{A}_{\mathrm{c}}^H$ and $\mathbf{R}_{\mathrm{r}} = \mathbf{A}_{\mathrm{r}}\mathbf{B}_{\mathrm{r}}\mathbf{A}_{\mathrm{r}}^H$. The matrix $\mathbf{B}_{\mathrm{c}} = \mathbf{D}_{\mathrm{c}}$ will be diagonal if the cosmic signals are uncorrelated and the same applies to $\mathbf{B}_{\mathrm{r}} = \mathbf{D}_{\mathrm{r}}$ and $\mathbf{R}_{\mathrm{n}} = \mathbf{D}_{\mathrm{n}}$ if the RFI and noise signals are respectively uncorrelated.

For a single source and no noise the jk^{th} element of the covariance matrix is given by

$$\mathbf{R}_{jk} = g_j\overline{g}_k\sigma^2 a_j\overline{a}_k = g_j\overline{g}_k\sigma^2 e^{-i2\pi\nu_0\tau_{jk}}, \tag{1.7}$$

where σ^2 is the power of the source and $\tau_{jk} = \tau_j - \tau_k$. This covariance matrix is a rank one matrix. If sources are added the number of non-zero eigenvalues will increase.

It is assumed that for short time periods the signals are stationary ergodic processes (the position of the source and its amplitude must remain constant). Therefore, the covariance is constant over this time period. The covariance matrix can then be estimated using

$$\widehat{\mathbf{R}} = \frac{1}{N_{\mathrm{t}}}\sum_{l=1}^{N_{\mathrm{t}}}\mathbf{y}(lT_{\mathrm{s}})\mathbf{y}^H(lT_{\mathrm{s}}), \tag{1.8}$$

where

$\widehat{\mathbf{R}}$ is the estimated covariance matrix,
N_{t} is the number of samples for which the signals are stationary,
T_{s} is the sample time.

The covariance matrix has the following useful properties: $\mathbf{R}$ is Hermitian and is positive semi-definite [18, p. 558].

Many of the spatial RFI mitigation schemes [11; 13–15] that have been developed make use of at least one of the following assumptions (the narrowband and statistical independence assumptions have already been introduced):

- **Point Source**: The RFI signals can be modelled as point sources (a source of electromagnetic radiation that is spatially infinitesimally small).
- **Narrowband**: The channel bandwidth $\Delta\nu$ is sufficiently narrow so that the propagation delay experienced by a signal can be represented as a phase shift.
- **Stationarity**: The cosmic signal is assumed to be a stationary Gaussian process for 10 s to 100 s, while the RFI signal must be stationary for durations less than 100 ms.

- **Gaussian Distributions with Mean Zero**: The cosmic, RFI and noise signals have Gaussian distributions and mean $\mu = 0$, therefore signal power is equal to the variance σ^2.
- **Statistical Independence**: The cosmic, RFI and noise signals are statistically independent and therefore uncorrelated.
- **Identically Distributed Noise**: If the antennas are calibrated, the random noise process in each antenna has the same distribution and consequently, the noise power σ_{n}^2 is approximately the same over short time periods and also for narrow frequency bands.
- **Low Signal Power**: The cosmic sources' contribution must be small in comparison to the noise contribution.
- **Number of RFI Sources**: The number of interferers must be less than the number of antennas for a given frequency and integration time. Also, the RFI must affect at least two dishes.

1.3.2 Near-field Model

The delay between the j^{th} array element and a signal is $\tau_j = ||\mathbf{v} - \mathbf{v}_j||/c$, where $\mathbf{v} = [x, y, z]^T$ and $\mathbf{v}_j = [x_j, y_j, z_j]^T$ are the position vector of the signal source and array element, respectively. Therefore, the geometric delay vector in equation (1.2) becomes [16, p. 32]

$$\mathbf{a} = \begin{bmatrix} e^{-i2\pi\nu_0||\mathbf{v}-\mathbf{v}_1||/c} \\ \vdots \\ e^{-i2\pi\nu_0||\mathbf{v}-\mathbf{v}_{N_{\text{e}}}||/c} \end{bmatrix}. \tag{1.9}$$

Using the near-field geometric delay vector in equation (1.9) the jk^{th} element of a covariance matrix for a single source without noise is then given by

$$\begin{aligned} \mathbf{R}_{jk} &= g_j \overline{g}_k \sigma^2 e^{-i2\pi\nu_0[||\mathbf{v}-\mathbf{v}_j||-||\mathbf{v}-\mathbf{v}_k||]/c} \\ &= g_j \overline{g}_k \sigma^2 e^{-i2\pi\nu_0\left[\sqrt{(x-x_j)^2+(y-y_j)^2+(z-z_j)^2}-\sqrt{(x-x_k)^2+(y-y_k)^2+(z-z_k)^2}\right]/c}. \end{aligned} \tag{1.10}$$

1.3.3 Far-field Model

The spherical wave front of a source in the far-field of the array can be approximated by a plane wave. The far-field distance is defined as [8, p. 601]

$$d_{\text{far}} \gg \frac{B_{\text{max}}^2}{\lambda}, \tag{1.11}$$

where $B_{\max}$ is the longest baseline and λ is the wavelength of the signal. At this distance the difference in path length between the source and the antennas forming the longest baseline, is much smaller than the wavelength. Therefore, all distance information is lost and only direction of arrival information can be recovered.

The following derivation will show how equation (1.9) can be adapted for a far-field source. Using the Taylor expansion of the distance between the signal and the j^{th} array element as well as $\frac{||\mathbf{v}_j||^2}{||\mathbf{v}||^2} \approx 0$, yields

$$\begin{aligned} ||\mathbf{v} - \mathbf{v}_j|| &= \sqrt{||\mathbf{v}||^2 + ||\mathbf{v}_j||^2 - 2\mathbf{v}\cdot\mathbf{v}_j} \\ &\approx ||\mathbf{v}||\sqrt{1 - \frac{2\mathbf{v}\cdot\mathbf{v}_j}{||\mathbf{v}||^2}} \\ &\approx ||\mathbf{v}|| - \frac{\mathbf{v}\cdot\mathbf{v}_j}{||\mathbf{v}||}. \end{aligned} \tag{1.12}$$

Subtracting the distances between the signal and the j^{th} and k^{th} array element, respectively, and using the approximation in equation (1.12) yields

$$||\mathbf{v} - \mathbf{v}_j|| - ||\mathbf{v} - \mathbf{v}_k|| \approx -\frac{\mathbf{v}\cdot\mathbf{v}_j}{||\mathbf{v}||} + \frac{\mathbf{v}\cdot\mathbf{v}_k}{||\mathbf{v}||}. \tag{1.13}$$

Therefore, when the geometric delay vector is multiplied with its Hermitian in the covariance equation (1.7) and the assumption is made that the source is in the far-field, then the phase is only dependent on the direction of arrival. That is, the effect of $||\mathbf{v}||$ on the phase of the geometric delay vector is cancelled out in the covariance matrix. Consequently, the geometric delay vector for a far-field source can be modelled as

$$\mathbf{a} = \begin{bmatrix} e^{i2\pi\nu_0(\mathbf{v}\cdot\mathbf{v}_1)/(c||\mathbf{v}||)} \\ \vdots \\ e^{i2\pi\nu_0(\mathbf{v}\cdot\mathbf{v}_{N_\mathrm{e}})/(c||\mathbf{v}||)} \end{bmatrix} = \begin{bmatrix} e^{i2\pi\nu_0(\mathrm{l}x_1+\mathrm{m}y_1+\mathrm{n}z_1)/c} \\ \vdots \\ e^{i2\pi\nu_0(\mathrm{l}x_{N_\mathrm{e}}+\mathrm{m}y_{N_\mathrm{e}}+\mathrm{n}z_{N_\mathrm{e}})/c} \end{bmatrix}, \tag{1.14}$$

where the directional cosines are defined as

$$\begin{bmatrix} \mathrm{l} \\ \mathrm{m} \\ \mathrm{n} \end{bmatrix} = \frac{\mathbf{v}}{||\mathbf{v}||} = \begin{bmatrix} x/||\mathbf{v}|| \\ y/||\mathbf{v}|| \\ z/||\mathbf{v}|| \end{bmatrix}. \tag{1.15}$$

Using the far-field geometric delay vector in equation (1.14), the jk^{th} element of a covariance matrix for a single source without noise is then given by

$$\begin{aligned} \mathbf{R}_{jk} &= g_j\overline{g}_k\sigma^2 e^{i2\pi\nu_0[\mathbf{v}\cdot\mathbf{v}_j - \mathbf{v}\cdot\mathbf{v}_k]/(c||\mathbf{v}||)} \\ &= g_j\overline{g}_k\sigma^2 e^{i2\pi\nu_0[\mathrm{l}(x_j-x_k)+\mathrm{m}(y_j-y_k)+\mathrm{n}(z_j-z_k)]/c}. \end{aligned} \tag{1.16}$$

1.3.4 Effect of Bandwidth on the Signal Model

If the channel bandwidth is not sufficiently narrow, the dependence of the geometric delay vector on frequency becomes significant. To simulate the effect of signal bandwidth on an array, the layout of a LOFAR Low Band Antenna (LBA) station was used and a signal with a center frequency of 45 MHz. The normalized eigenvalues of the simulated covariance matrix are plotted as a function of fractional bandwidth in figure 1.2 a. At zero fractional bandwidth, there is only one non-zero eigenvalue. As the fractional bandwidth increases, the first eigenvalue decreases and the other eigenvalues become non-zero. The severity of the bandwidth effect on the eigenstructure of the covariance matrix is also dependent on the location of the source. For a planar array, such as a LOFAR station, sources closer to the horizon cause the most distortion of the eigenstructure (see figure 1.2 b).

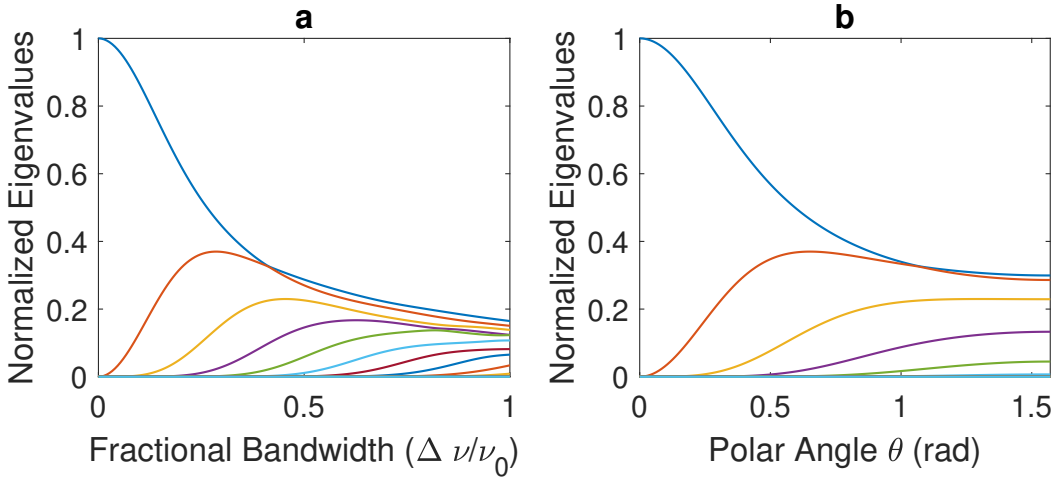

Figure 1.2: **(a)** Plot of normalized eigenvalues of a covariance matrix where the fractional bandwidth of a single source is increased and the source position is fixed. **(b)** Plot of normalized eigenvalues of a covariance matrix where a single source moves from zenith (0 rad) to the horizon (π rad) with a fixed bandwidth. For both plots no noise is present and the layout of a LOFAR low band antenna station is used.

The LOFAR telescope's antennas are optimized to work from 10 to 240 MHz and typically have a channel bandwidth of 195 kHz. If the narrowband criteria in equation (1.1) is used, any signal detected by a LOFAR LBA or High Band Antenna (HBA) core station (with longest baselines 107 m and 159 m, respectively) would be classified as narrowband. However, this criterion is not valid in the case of powerful RFI signals with spectrum that spans the channel. In figure 1.3 a the skymap of such a RFI source is given and appears to be a point source. When the first eigenvalue is nulled the RFI is suppressed by 24.3 dB, as can be seen in the skymap in figure 1.3 b. Two weaker sources adjacent to

the location of the RFI are now visible and are caused by the bandwidth of the RFI source. The power of these two bandwidth-related sources is of the same order of magnitude as those of the visible cosmic sources, in this case Cassiopeia A and Cygnus A. Consequently, a signal will then be classified as non-narrowband if its second eigenvalue is large enough to cause interference with the cosmic sources being studied.

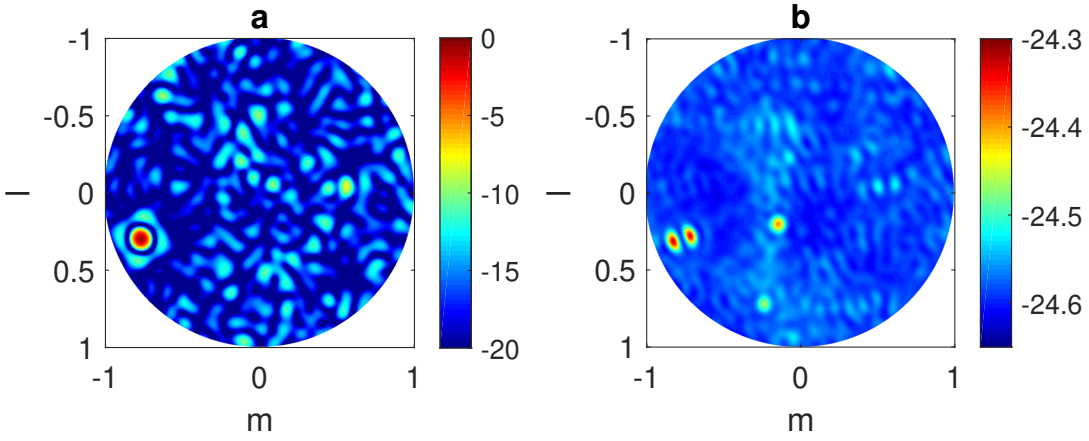

Figure 1.3: **(a)** Skymap of non-narrowband RFI source visible in dB (the RFI source is the 0 dB point). **(b)** Skymap of non-narrowband RFI source where the first eigenvalue of the covaraince matrix has been nulled. Two weaker sources adjacent to the location of the RFI are now visible and are caused by the bandwidth of the RFI source. Cassiopeia A and Cygnus A are also visible as point sources.

1.3.5 Non-identically Distributed Noise

Consider a covariance matrix $\mathbf{R} = \mathbf{R}_\mathrm{r} + \mathbf{R}_\mathrm{r}$ which consists of a non-identically distributed noise covariance matrix $\mathbf{R}_\mathrm{n} = \mathrm{diag}(\sigma^2_{\mathrm{n},1}, \ldots, \sigma^2_{\mathrm{n},N_\mathrm{e}})$ and an RFI covariance matrix $\mathbf{R}_\mathrm{r}$. Since $\mathbf{R}_\mathrm{n}$ is not an identically distributed noise covariance matrix, the eigenvectors of $\mathbf{R}$ and $\mathbf{R}_\mathrm{r}$ will differ [11, p. 64-65]. However, if the power of the RFI is much larger than the noise power ($\sigma^2_{\mathrm{r},i} \gg \sigma^2_{\mathrm{n},i}$), the effect of noise on the covariance matrix's eigenvalues will diminish. Two methods to remove the effect of the noise for cases in which this assumption does not hold, will be presented.

1.3.5.1 Noise Whitening

If an estimate of the noise covariance matrix[1] $\widetilde{\mathbf{R}}_\mathrm{n}$ is available, then the inter-

[1] A tilde is used to distinguish $\widetilde{\mathbf{R}}_\mathrm{n}$ from $\widehat{\mathbf{R}}_\mathrm{n}$ which, is the noise estimate that forms part of $\widehat{\mathbf{R}}$.

ferometer covariance matrix can be whitened [16, p. 34],

$$\begin{aligned}\mathbf{R}_{\mathrm{w}} =& \widetilde{\mathbf{R}}_{\mathrm{n}}^{-\frac{1}{2}}(\mathbf{G}\mathbf{R}_{\mathrm{r}}\mathbf{G}^{H} + \mathbf{R}_{\mathrm{n}})\widetilde{\mathbf{R}}_{\mathrm{n}}^{-\frac{1}{2}} \\ \approx& \widetilde{\mathbf{R}}_{\mathrm{n}}^{-\frac{1}{2}}\mathbf{G}\mathbf{R}_{\mathrm{r}}\mathbf{G}^{H}\widetilde{\mathbf{R}}_{\mathrm{n}}^{-\frac{1}{2}} + \mathbf{I}. \end{aligned} \tag{1.17}$$

The result is that the noise covariance matrix becomes the identity matrix and consequently eigenvalue decomposition can be applied to identify a basis for the RFI vector space. An estimate of the noise can be obtained either by calibration or by examining regions where there are no interference.

1.3.5.2 Factor Analysis

Factor analysis [19, p.211-232] is a statistical method that decomposes a $p \times p$ covariance matrix $\mathbf{R} = \mathbf{Z}\mathbf{Z}^{H} + \mathbf{D}$, where $\mathbf{Z}$ is a $p \times q$ matrix and $\mathbf{D}$ is a $p \times p$ diagonal matrix. This decomposition can be applied to an interferometer's covariance matrix $\mathbf{R}$ [15] in the case where the noise is not calibrated by equating $\mathbf{R}_{\mathrm{r}} = \mathbf{Z}\mathbf{Z}^{H}$ and $\mathbf{R}_{\mathrm{n}} = \mathbf{D}$ (the influence of the cosmic source is considered negligible). Thus

$$\begin{aligned}\mathbf{R} =& \mathbf{Z}\mathbf{Z}^{H} + \mathbf{D} \\ =& \mathbf{R}_{\mathrm{r}} + \mathbf{R}_{\mathrm{n}}. \end{aligned} \tag{1.18}$$

This method places a restriction on the number of factors (that is interferers), namely $q < p - \sqrt{p}$ [15].

1.4 RFI Mitigation Techniques

RFI mitigation by subspace projection for radio astronomy was first proposed in [12], where orthogonal projection with bias correction was introduced. This method requires high interference-to-noise-ratio and relative movement between the interferer and the phase reference position of the array. Further analysis of this method is given in [13–15]. Other projection methods, such as oblique projection are explained in [11]. For the case where there is low interference-to-noise-ratio and relative movement between the interferer and the phase reference position of the array, the method in [20] can be used. Furthermore, low-cost auxiliary antennas can be included to improve performance [21].

1.4.1 Orthogonal Projection

If the column vectors of $\mathbf{A}_{\mathrm{r}}$ are linearly independent, they form a basis for a vector space V_{r}. Therefore, an orthogonal projector can be constructed [18, p.

430] which projects along V_r onto a vector space orthogonal to V_r , namely

$$\mathbf{P} = \mathbf{I} - \mathbf{A}_\mathrm{r}(\mathbf{A}_\mathrm{r}^H\mathbf{A}_\mathrm{r})^{-1}\mathbf{A}_\mathrm{r}^H, \tag{1.19}$$

such that $\mathbf{PA}_\mathrm{r} = \mathbf{0}$. The projector is Hermitian and therefore $\mathbf{P} = \mathbf{P}^H$ [18, p. 433]. Applying the projector to equation (1.6) yields (assuming $\mathbf{G} = \mathbf{I}$)

$$\begin{aligned}\mathbf{PRP} =& \mathbf{PR}_\mathrm{c}\mathbf{P} + \mathbf{PA}_\mathrm{r}\mathbf{B}_\mathrm{r}\mathbf{A}_\mathrm{r}\mathbf{P} + \mathbf{PR}_\mathrm{n}\mathbf{P} \\ =& \mathbf{PR}_\mathrm{c}\mathbf{P} + \mathbf{PR}_\mathrm{n}\mathbf{P} \\ =& \mathbf{PR}_\mathrm{cn}\mathbf{P},\end{aligned} \tag{1.20}$$

where $\mathbf{R}_\mathrm{cn} = \mathbf{R}_\mathrm{c} + \mathbf{R}_\mathrm{n}$. The RFI contribution to the covariance is completely nulled, however, the noise and cosmic signals are biased.

1.4.2 RFI Subspace Estimation

Any basis of the RFI subspace V_r can be used to construct the projector in equation (1.19), not just $\mathbf{A}_\mathrm{r}$. The ability of the orthogonal projector to null the contribution of RFI is dependent on the accuracy of the estimate of a basis set that spans the vector space V_r. When the direction of arrival for the RFI is not known, $\mathbf{A}_\mathrm{r}$ cannot be calculated. However, an orthogonal set of eigenvectors can be found by applying eigenvalue decomposition (EVD) to the covariance matrix, because the covariance matrix is positive definite [18, p. 517]. If it can be assumed that the cosmic signal contribution can be ignored, that the noise is independently and identically distributed and that the RFI signals are uncorrelated, then the EVD of the covariance matrix yields [11, p. 64-65]

$$\begin{aligned}\mathbf{R} \approx& \mathbf{R}_\mathrm{r} + \mathbf{D}_\mathrm{n} \\ =& \begin{bmatrix}\mathbf{M}_\mathrm{r} & \mathbf{K}_\mathrm{r}\end{bmatrix}\begin{bmatrix}\mathbf{D}_\mathrm{r} & \mathbf{0} \\ \mathbf{0} & \mathbf{0}\end{bmatrix}\begin{bmatrix}\mathbf{M}_\mathrm{r}^H \\ \mathbf{K}_\mathrm{r}^H\end{bmatrix} + \sigma_n^2\mathbf{I} \\ =& \begin{bmatrix}\mathbf{M}_\mathrm{r} & \mathbf{K}_\mathrm{r}\end{bmatrix}\mathbf{D}_\mathrm{rn}\begin{bmatrix}\mathbf{M}_\mathrm{r}^H \\ \mathbf{K}_\mathrm{r}^H\end{bmatrix} \\ =& \begin{bmatrix}\mathbf{M}_\mathrm{r} & \mathbf{K}_\mathrm{r}\end{bmatrix}\begin{bmatrix}\mathbf{D}_\mathrm{r} + \sigma_\mathrm{n}^2\mathbf{I}_{N_\mathrm{r}\times N_\mathrm{r}} & \mathbf{0} \\ \mathbf{0} & \sigma_\mathrm{n}^2\mathbf{I}_{(N_\mathrm{e}-N_\mathrm{r})\times(N_\mathrm{e}-N_\mathrm{r})}\end{bmatrix}\begin{bmatrix}\mathbf{M}_\mathrm{r}^H \\ \mathbf{K}_\mathrm{r}^H\end{bmatrix},\end{aligned} \tag{1.21}$$

where

$\mathbf{M}_\mathrm{r}$ is the matrix of eigenvectors that form the range of V_r,
$\mathbf{K}_\mathrm{r}$ is the matrix of eigenvectors that form the kernel of V_r,
$\mathbf{D}_\mathrm{r}$ is the diagonal matrix of eigenvalues $(\lambda_{\mathrm{r},j})$ for $\mathbf{R}_\mathrm{r}$,
$\mathbf{D}_\mathrm{rn}$ is the diagonal matrix of eigenvalues (λ_j) for $\mathbf{R}$.

The column vectors of $\mathbf{M}_\mathrm{r}$ are orthogonal as well as those of $\mathbf{K}_\mathrm{r}$. For the case where there are two or more RFI signals, it is unlikely that $\mathbf{M}_\mathrm{r}$ will be equal to $\mathbf{A}_\mathrm{r}$. Therefore, the vector space V_r is spanned differently and the

eigenvalues $\lambda_{\mathrm{r},j}$ will not be equal to the RFI powers $\sigma^2_{\mathrm{r},j}$ (however the total power will be the same). The noise only affects the eigenvalues of the $\mathbf{R}_\mathrm{r}$ and not its eigenvectors, because the noise is identically distributed [11, p. 65].

The orthogonal projector in equation (1.19) can now be constructed using $\mathbf{M}_\mathrm{r}$, which is identified by the larger eigenvalues in $\mathbf{D}_\mathrm{rn}$. The requirement that $\mathbf{R}_\mathrm{c}$ can be ignored is necessary, since its contribution will influence the eigenvalues and eigenvectors of $\mathbf{R}$. This requirement is made more precise in [14] with the expression

$$|(\mathbf{R}_\mathrm{c})_{jk}| \ll \frac{\sigma_n^2}{\sqrt{N}}, \tag{1.22}$$

where N is the number of samples taken to estimate $\mathbf{R}$.

One simple method [22] to identify the RFI is to count the eigenvalues which exceed three median absolute deviations from the median

$$\lambda_j > 3 \cdot \mathrm{median}(|\mathbf{D}_\mathrm{rn} - \mathrm{median}(\mathbf{D}_\mathrm{rn})|) + \mathrm{median}(\mathbf{D}_\mathrm{rn}), \tag{1.23}$$

where λ_j is the j^{th} eigenvalue contained in $\mathbf{D}_\mathrm{rn}$. Using the median lessens the influence of outliers, that is, the values affected by the RFI. Alternative methods are given in [23–25].

1.4.3 Orthogonal Projection with Bias Correction

For any useful orthogonal projector $\mathbf{P}$, the kernel basis includes the zero vector and at least one non-zero vector. Therefore, $\mathbf{P}$ has a column rank less than the number of columns in $\mathbf{P}$ which consequently makes the matrix singular. The orthogonal projection method bias (see equation (1.20)) can therefore not be corrected by multiplying with the inverted orthogonal projector.

For the orthogonal projection correction scheme [12–15] the number of samples N_t is divided into N_G equally sized groups, where each group consists of $N_{\mathrm{t,st}}$ samples (st denotes short term), that is, $N_\mathrm{t} = N_\mathrm{G} N_{\mathrm{t,st}}$. For a sampling time T_s the overall integration time is $N_\mathrm{t} T_\mathrm{s}$, while $N_{\mathrm{t,st}} T_\mathrm{s}$ is the short term integration time for any of the N_G groups. The following assumptions must also hold:

- The cosmic signals are stationary for $N_\mathrm{t} T_\mathrm{s}$ seconds.
- The RFI signals are stationary for $N_{\mathrm{t,st}} T_\mathrm{s}$ seconds.
- The RFI signals are not stationary for $N_\mathrm{t} T_\mathrm{s}$ seconds.
- $\mathbf{G} = \mathbf{I}$.

The l^{th} short term covariance matrix estimate is given by

$$\widehat{\mathbf{R}}_l = \frac{1}{N_{\mathrm{t,st}}} \sum_{m=(l-1)N_{\mathrm{t,st}}+1}^{lN_{\mathrm{t,st}}} \mathbf{y}(mT_{\mathrm{s}})\mathbf{y}(mT_{\mathrm{s}})^H, \tag{1.24}$$

where $l \in \{1, \cdots, N_{\mathrm{G}}\}$. The covariance matrix estimate can then be written as

$$\widehat{\mathbf{R}} = \frac{1}{N_{\mathrm{G}}} \sum_{l=1}^{N_{\mathrm{G}}} \widehat{\mathbf{R}}_l. \tag{1.25}$$

For each short term integration covariance matrix estimate $\widehat{\mathbf{R}}_l$, an orthogonal RFI projector $\mathbf{P}_l$, can be constructed, since the RFI is assumed stationary over the short term integration time ($N_{\mathrm{t,st}}T_{\mathrm{s}}$). The averaged orthogonal projected covariance matrix estimate is then

$$\begin{aligned}
\widehat{\mathbf{R}}_{\mathrm{orth}} =& \frac{1}{N_{\mathrm{G}}} \sum_{l=1}^{N_{\mathrm{G}}} \mathbf{P}_l \widehat{\mathbf{R}}_l \mathbf{P}_l \\
=& \frac{1}{N_{\mathrm{G}}} \sum_{l=1}^{N_{\mathrm{G}}} \mathbf{P}_l (\widehat{\mathbf{R}}_{\mathrm{c}} + \widehat{\mathbf{R}}_{\mathrm{r},l} + \widehat{\mathbf{R}}_{\mathrm{n}}) \mathbf{P}_l \\
=& \frac{1}{N_{\mathrm{G}}} \sum_{l=1}^{N_{\mathrm{G}}} \mathbf{P}_l (\widehat{\mathbf{R}}_{\mathrm{c}} + \widehat{\mathbf{R}}_{\mathrm{n}}) \mathbf{P}_l \\
=& \frac{1}{N_{\mathrm{G}}} \sum_{l=1}^{N_{\mathrm{G}}} \mathbf{P}_l (\widehat{\mathbf{R}}_{\mathrm{cn}}) \mathbf{P}_l.
\end{aligned} \tag{1.26}$$

Applying the matrix identity

$$\mathrm{vec}(\mathbf{ABC}) \equiv (\mathbf{C}^T \otimes \mathbf{A})\,\mathrm{vec}(\mathbf{B}), \tag{1.27}$$

to equation (1.26) yields

$$\begin{aligned}
\mathrm{vec}(\widehat{\mathbf{R}}_{\mathrm{orth}}) &= \frac{1}{N_{\mathrm{G}}} \sum_{k=1}^{N_{\mathrm{G}}} (\mathbf{P}_l^T \otimes \mathbf{P}_l)\,\mathrm{vec}(\widehat{\mathbf{R}}_{\mathrm{cn}}) \\
&= \left\{ \frac{1}{N_{\mathrm{G}}} \sum_{k=1}^{N_{\mathrm{G}}} (\mathbf{P}_l^T \otimes \mathbf{P}_l) \right\} \mathrm{vec}(\widehat{\mathbf{R}}_{\mathrm{cn}}) \\
&= \mathbf{C}\,\mathrm{vec}(\widehat{\mathbf{R}}_{\mathrm{cn}}).
\end{aligned} \tag{1.28}$$

The RFI is however assumed to be non-stationary over the total integration time $N_{\mathrm{t}}T_{\mathrm{s}}$, therefore, $\mathbf{P}_l$ will vary between the short term integration groups.

The matrix $\mathbf{C}$ becomes non-singular if N_{G} is large enough and the orthogonal projectors vary sufficiently. The corrected covariance matrix is then

$$\widehat{\mathbf{R}}_{\mathrm{cn}} = \mathrm{unvec}(\mathbf{C}^{-1}\,\mathrm{vec}(\widehat{\mathbf{R}}_{\mathrm{orth}})). \tag{1.29}$$

In figure 1.4, a diagram is given showing how the orthogonal projection with bias correction algorithm can be implemented.

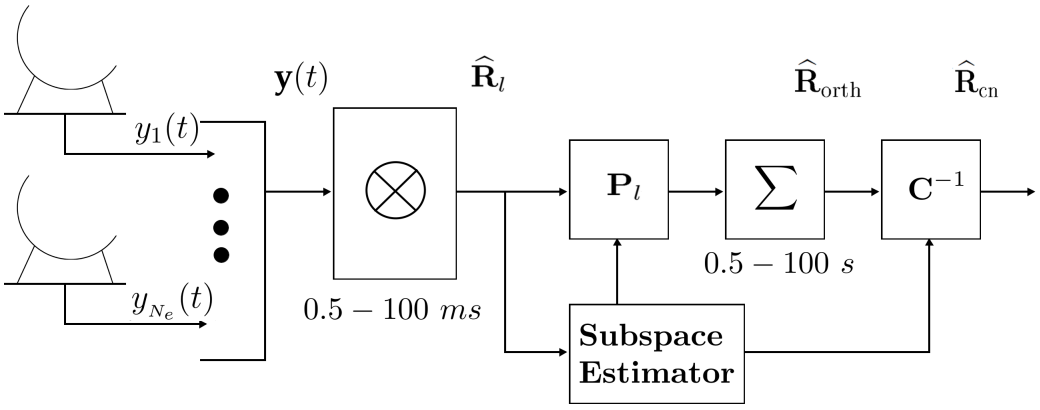

Figure 1.4: Diagram of the orthogonal projection with bias correction algorithm.

1.4.4 Oblique Projection

The oblique projection method projects along the RFI vector space V_{r} onto the cosmic vector space V_{c}. To construct this oblique projector it is required that the column vectors in $[\mathbf{A}_{\mathrm{c}}\mathbf{A}_{\mathrm{r}}]$ are independent ($V_{\mathrm{r}} \cap V_{\mathrm{c}} = \{\mathbf{0}\}$). The oblique projector is given by [11, p. 51]

$$\mathbf{E}_{V_{\mathrm{r}}\to V_{\mathrm{c}}} = \mathbf{A}_{\mathrm{c}}(\mathbf{A}_{\mathrm{c}}^H\mathbf{P}_{V_{\mathrm{r}}}^{\perp}\mathbf{A}_{\mathrm{c}})^{-1}\mathbf{A}_{\mathrm{c}}^H\mathbf{P}_{V_{\mathrm{r}}}^{\perp}, \tag{1.30}$$

where $\mathbf{P}_{V_{\mathrm{r}}}^{\perp}$ is an orthogonal projector that projects along V_{r} onto a vector space that is orthogonal to V_{r}. When an oblique projector is applied the RFI is completely nulled and the cosmic signal is completely recovered, however the noise is biased

$$\begin{aligned}\mathbf{R}_{\mathrm{obl}} &= \mathbf{E}_{V_{\mathrm{r}}\to V_{\mathrm{c}}}\mathbf{R}\mathbf{E}_{V_{\mathrm{r}}\to V_{\mathrm{c}}}^H \\ &= \mathbf{R}_{\mathrm{c}} + \mathbf{E}_{V_{\mathrm{r}}\to V_{\mathrm{c}}}\mathbf{R}_{\mathrm{n}}\mathbf{E}_{V_{\mathrm{r}}\to V_{\mathrm{c}}}^H.\end{aligned} \tag{1.31}$$

For the case when V_{r} and V_{c} are orthogonal, the oblique and orthogonal projectors are equivalent. This method's accuracy depends not only on the RFI subspace estimation, but also on the accuracy of the sources' positions in the model skymap.

1.5 Source Localization Techniques

For near-field sources, it is possible to get the location of the source while, for far-field sources, it is only possible to recover the direction of arrival. Three methods, that can be adapted for both far-field and near-field cases, will be discussed: discrete Fourier transform based method, Minimum Variance Distortionless Response (MVDR) and MUltiple SIgnal Classification (MUSIC). All these methods are computationally expensive, brute force methods; however, no assumptions are made about the array layout.

For the near-field case the vector $\mathbf{v}$ is a set of Cartesian coordinates and $\mathbf{a}$ is the near-field geometric delay (see equation (1.9)). In the far-field case the vector $\mathbf{v}$ is a set of directional cosine coordinates and $\mathbf{a}$ is the far-field geometric delay (see equation (1.14)).

1.5.1 Classical Delay Beamforming Imaging (CDB)

CDB imaging is an algorithm that makes use of a classical delay beamformer ($\mathbf{b}_{\text{CDB}}$) [26, p. 78-79]

$$\mathbf{b}_{\text{CDB}}(\mathbf{v}) = (\mathbf{a}^H(\mathbf{v})\mathbf{a}(\mathbf{v}))^{-1}\mathbf{a}^H(\mathbf{v}). \tag{1.32}$$

The CDB spatial spectrum or CDB skymap is then given by

$$\begin{aligned}\mathbf{J}_{CDB}(\mathbf{v}) &= \mathbb{E}\{\mathbf{b}_{\text{CDB}}(\mathbf{v})\mathbf{x}(t)(\mathbf{b}_{\text{CDB}}(\mathbf{v})\mathbf{x}(t))^H\} \\ &= \mathbf{b}_{\text{CDB}}(\mathbf{v})\mathbf{R}\mathbf{b}^H_{\text{CDB}}(\mathbf{v}) \\ &= \frac{\mathbf{a}^H(\mathbf{v})\mathbf{R}\mathbf{a}(\mathbf{v})}{(\mathbf{a}^H(\mathbf{v})\mathbf{a}(\mathbf{v}))^2}.\end{aligned} \tag{1.33}$$

The algorithm therefore requires that a beamfomer be constructed for every pixel (coordinate of interest). The advantage of this method is that the flux of the source is recovered.

1.5.2 Minimum Variance Distortionless Response Imaging (MVDR)

MVDR imaging is an algorithm which makes use of a beamformer ($\mathbf{b}_{\text{MVDR}}$) that minimizes the output energy of a given position on a skymap [26, p. 96]

$$\mathbf{b}_{\text{MVDR}} = \frac{\mathbf{R}^{-1}\mathbf{a}(\mathbf{v})}{\mathbf{a}^H(\mathbf{v})\mathbf{R}^{-1}\mathbf{a}(\mathbf{v})}. \tag{1.34}$$

The MVDR spatial spectrum or MVDR skymap is given by

$$\begin{aligned}J_{\text{MVDR}}(\mathbf{v}) &= \mathbf{b}^H_{\text{MVDR}}\mathbf{R}\mathbf{b}_{\text{MVDR}} \\ &= \frac{1}{\mathbf{a}(\mathbf{v})\mathbf{R}^{-1}\mathbf{a}^H(\mathbf{v})},\end{aligned} \tag{1.35}$$

where the peaks of $J_{\text{MVDR}}(\mathbf{v})$ are the locations of the sources. The disadvantages of this method are that the covariance matrix must be non-singular and calibration errors lead to underestimation of the source's power.

1.5.3 MUltiple SIgnal Classification Imaging (MUSIC)

The MUSIC algorithm is an algorithm that calculates the MUSIC spatial spectrum or MUSIC skymap [26, p. 80-82]

$$J_{\text{MUSIC}}(\mathbf{v}) = \frac{1}{\mathbf{a}(\mathbf{v})\mathbf{K}_r\mathbf{K}_r^H\mathbf{a}^H(\mathbf{v})}, \tag{1.36}$$

where the peaks of $J_{\text{MUSIC}}(\mathbf{v})$ are the locations of the RFI sources and $\mathbf{K}_r$ is the signal nullspace (see section 1.4.2). The peaks of $J(\mathbf{v})_{\text{MUSIC}}$ occur when $\mathbf{a}(\mathbf{v})$ is approaching orthogonality to $\mathbf{K}_r$. The disadvantage of this method is that the source's nullspace must be correctly estimated.

1.5.4 Current Research in Source Localization

The computational cost of the aforementioned imaging methods are prohibitive. Currently there are numerous computationally more efficient methods that have been developed. Examples include path following [27], polynomial rooting [28], weighted linear prediction [29] and estimation of signal parameters using rotational invariance techniques (ESPRIT) [30; 31]. These methods reduce computational complexity by assuming and then exploiting a uniform linear array layout. In papers [32] and [33] an improvement of the MUSIC algorithm is proposed that replaces searching a dimension with solving the roots of a polynomial. This polynomial arises from calculating a Fourier series which estimates the geometric delay function. This method introduces an estimation error. Furthermore, all these methods assume a narrowband source signal. Methods that can localize wideband signals make use of an initial Fourier transform of the data [34; 35].

1.6 The Low-Frequency Array (LOFAR)

The Low-Frequency Array (LOFAR) is a radio telescope interferometer that was completed in 2012 by ASTRON (the Netherlands Institute for Radio Astronomy) and its international partners [3]. The telescope has stations across Europe with the current (as of October 2018) longest baseline between Birr, Ireland and Łazy, Poland, which is almost 2000 km (see figure 1.5). Additional stations are also planned for Irbene, Latvia and Medicina, Italy. Each station consists of an array of Low Band Antennas (LBA's) and an array of High Band Antennas (HBA's). The HBA's are arranged into tiles that each consist of 16 HBA's. The LBA's are optimized to observe from 10 to 80 MHz and

the HBA's from 120 to 240 MHz. There are 24 core stations around Exloo, the Netherlands where each has one field of 96 LBA's and two fields of 24 HBA tiles, each straddling the LBA's. The 14 remote non-core stations in the Netherlands each consist of one field of 96 LBA's and one field of 48 HBA tiles. In figure 1.6 a satellite image is given of a LOFAR remote station. The 13 international stations (non-Dutch stations) consist of one field of 96 LBA's and one field of 96 HBA tiles. The LBA's and HBA's are both dipole designs and are immovable. To point in a certain direction the antennas in a field are beamformed to synthesize a larger aperture. The beamformed data from each station is sent to the LOFAR Central Processing Facilities in Groningen to be correlated.

One of the most common RFI signals that is detected by the HBA's of LOFAR is digital audio broadcasts (DAB). These broadcasts make use of powerful transmitters and occupy the frequency band from 174 to 228 MHz in the Netherlands. For example, Zendstation Smilde has a DAB transmitter at 253 m altitude and transmits at 3.5 kW. This tower is only 9.16 km from LOFAR station RS409. In figure 1.8 the power spectral density of one of the LOFAR HBA's is plotted and a DAB signal is approximately 95 dB above the noise and occupies the 182.9 to 184.4 MHz band.

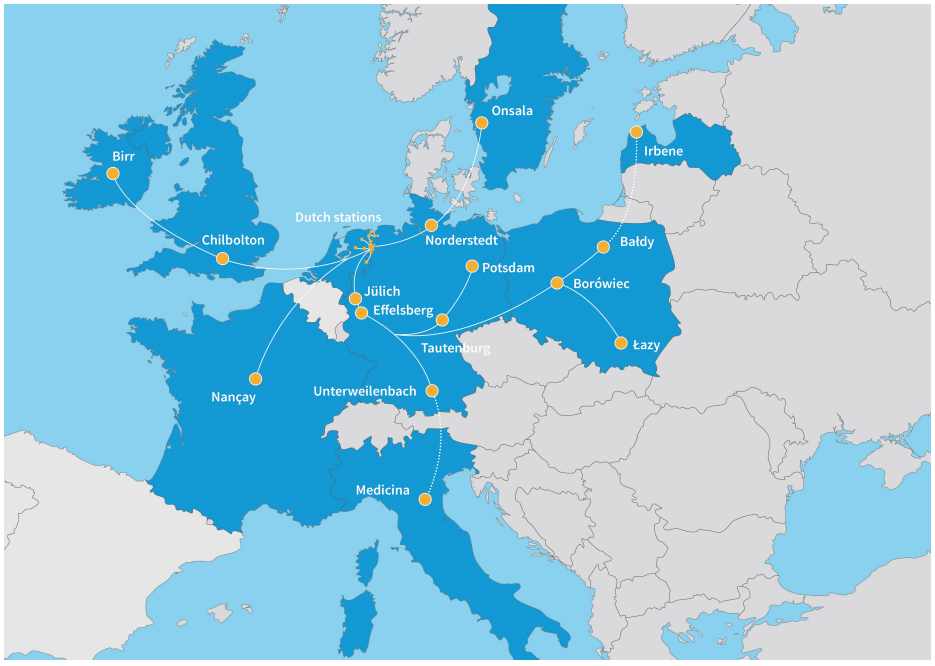

Figure 1.5: Map of LOFAR stations across Europe. Stations that are connected with a dotted line are being built. Image courtesy of Dr. Tammo Jan Dijkema from the Computing Group at ASTRON.

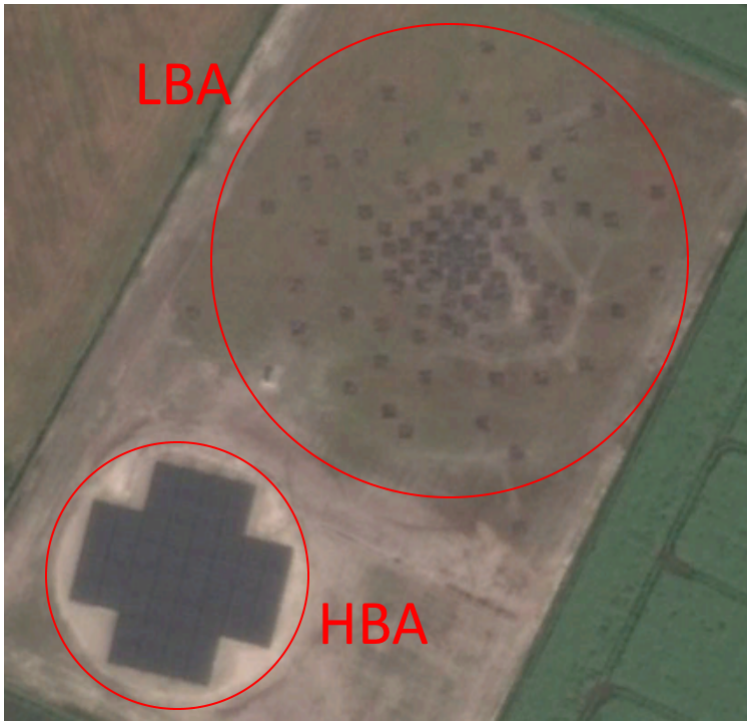

Figure 1.6: Google Earth satellite image of LOFAR remote station RS409 with the HBA and LBA encircled.

1.7 Objectives and Original Contributions

The best solution to RFI is to remove the source. Therefore, the source must be identified and localized. Radio astronomy arrays have the following constraints: the array layout is usually non-uniform in order to maximize uv coverage; RFI sources can not be assumed to be narrowband; RFI sources can be far-field or near-field and the data from the arrays are not calibrated in the direction of the RFI. Thus, most recent methods that make use of uniform linear arrays can not be used. Radio astronomy arrays have the advantages that they have a large number of elements, they measure a wide bandwidth which is broken up into a large number of channels, cosmic source signal powers are far below the instrumental noise level (therefore it will not interfere with RFI source identification) and covariance matrices have to be produced for the science objectives (such as imaging). The next paragraph provides a summary of the contributions to source localization (see the journal paper in section 2.4).

A new computationally efficient localization algorithm has been developed for interferometric arrays with low array beam sidelobes. The algorithm has been adapted to work both in the near-field and far-field (only the direction of arrival can be recovered when the source is in the far-field). The algorithm consists of three stages. The first is a preprocessing stage that attempts to

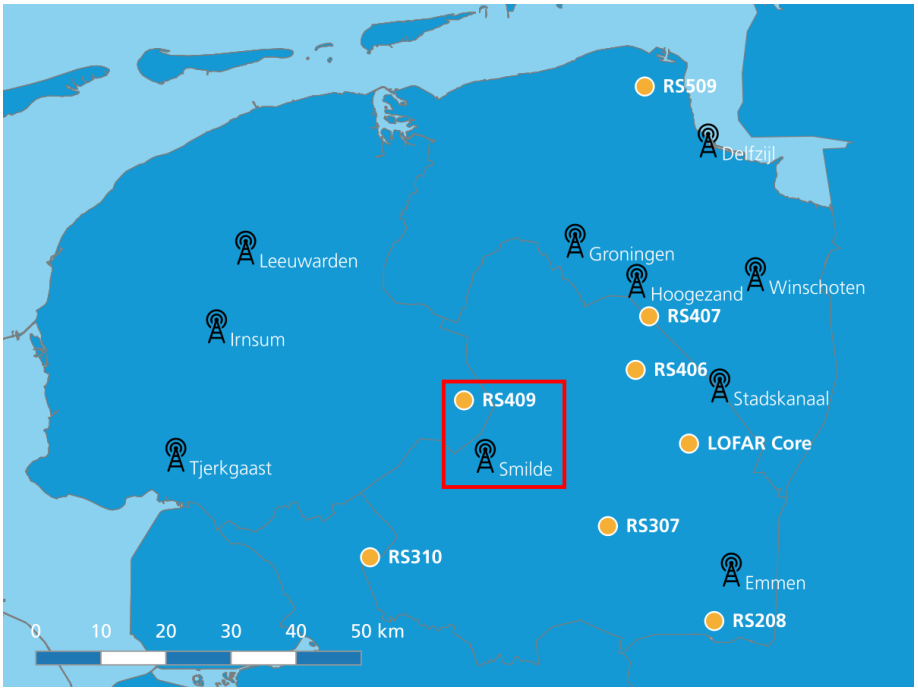

Figure 1.7: Map of LOFAR stations in the Netherlands along with DAB broadcast towers. Zendstation Smilde has a DAB transmitter at 253 m altitude and is only 9.16 km from station RS409. Image courtesy of Dr Tammo Jan Dijkema from the Computing Group at ASTRON.

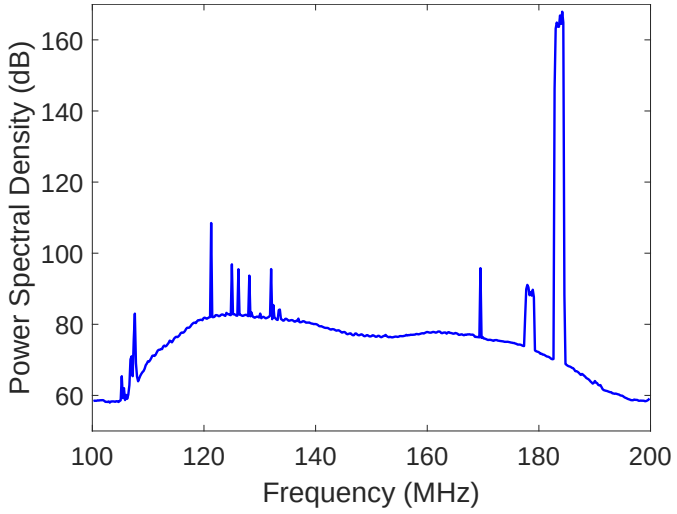

Figure 1.8: Power spectral density of signal received by a HBA in LOFAR station RS409. Reproduced from journal paper in section 2.6

isolate the RFI source by using factor analysis. The second is the integrating-out-variables method that, for the near-field case, changes a three dimensional search to three one dimensional searches by integrating out coordinate variables. This gives a reasonable estimate for the minimum error convergence (MEC) algorithm, which is a fast converging iterative method. The MEC linearizes the single source array covariance matrix model by reformulating it in terms of the estimation error of the source's location. In the near-field, the computational complexity of the algorithm is linear with search grid size compared to cubic scaling of the state-of-the-art 3-D MUSIC method. The trade-off is that the proposed algorithm requires a once-off a priori calculation and storing of weighting matrices. To reduce the storage requirements, one of the weighting matrices can be calculated on the fly using a Taylor expansion of the function to be integrated. To test the algorithm, uncalibrated data from a LOFAR LBA station was used where a hexacopter, with a transmitter, was flown around the array. The result was that the mean distance between the estimated position of the hexacopter and the GPS position of the hexacopter was 2 m at a wavelength of 6.7 m. In figure 1.9 a, b and c plots are given of the GPS and recovered spherical coordinates.

If an RFI source can not be localized or can not be switched off, the alternative is to mitigate its effect using methods such as spatial RFI mitigation (see section 1.4). These methods are able to recover astronomical data from the presence of powerful RFI sources. However, most of the methods assume a narrowband signal which is not always the case. The next paragraph provides a summary of the contributions to RFI mitigation (see the journal papers in sections 2.5 and 2.6).

Two related RFI mitigation algorithms have been developed for non-narrowband RFI signals which assume that the frequency response of the RFI signal is approximately flat. The first algorithm is based on a flat frequency response model and the second is based on an approximation of the flat frequency response model that uses two frequency shifted monochromatic signals, developed by [36]. These models are then combined with a first order subspace subtraction method. The algorithms are of use when the power in the frequency smeared component of an RFI source has a power similar to those of the cosmic sources. In section 2.5 these algorithms are described in detail, as well as an equation which gives the direction of arrival for a far-field non-narrowband signal that causes the greatest distortion of the visibilities. Another equation included gives the appropriate frequency channel bandwidth at which to implement the proposed non-narrowband RFI mitigation algorithms. Array imperfections such as unknown complex gains and mutual coupling are also considered and incorporated into the non-narrowband signal models in section 2.6. The evaluation of the algorithm was done using the layout of a LOFAR High Band Antenna (HBA) station and a digital audio broadcast recorded with a software defined radio. Using only the DAB spectrum and no array imperfections, the proposed algorithms processed six times the band-

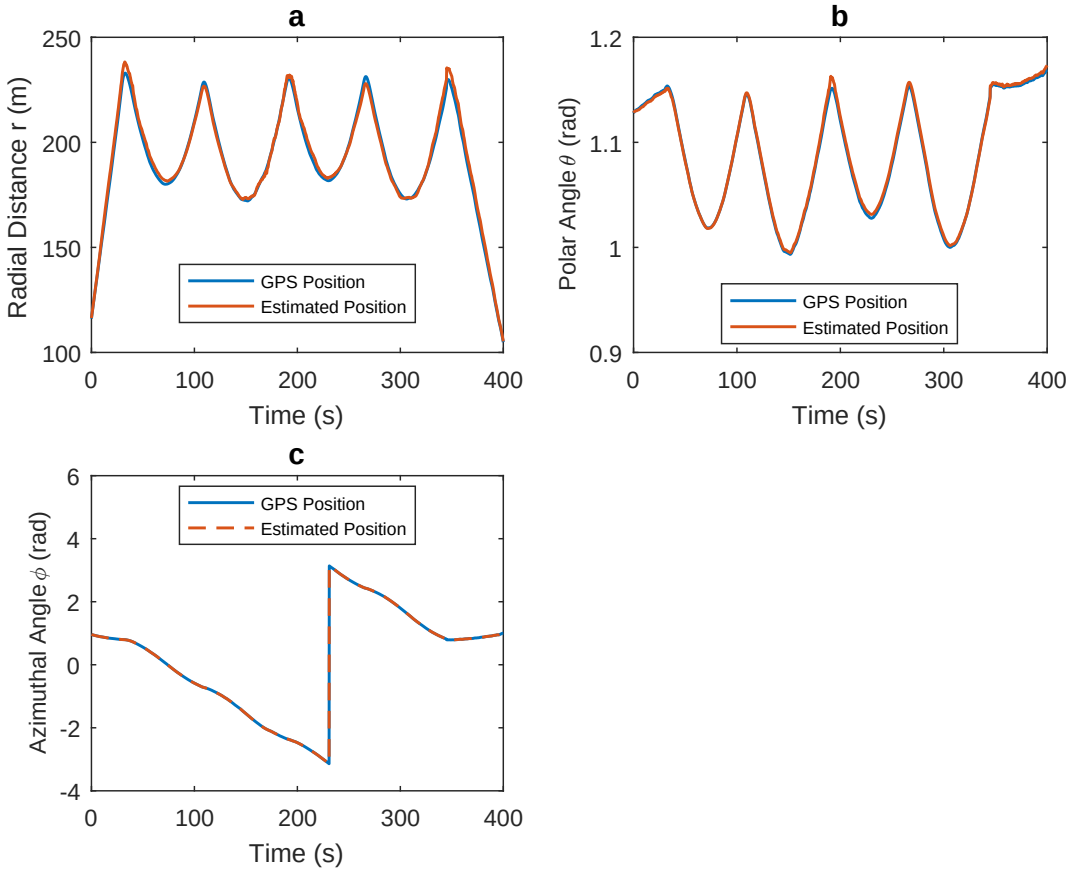

Figure 1.9: **(a)** GPS and estimated radial distances of the hexacopter from the array center, observed over time. **(b)** GPS and estimated polar angles of the hexacopter from the array center, observed over time. **(c)** GPS and estimated azimuthal angles of the hexacopter from the array center, observed over time. Reproduced from journal paper in section 2.4.

width per channel when compared to conventional narrowband techniques. This performance reduces to twice more bandwidth when unknown complex gains are added and then calibrated for. When mutual coupling is also added, the performance declines further to 1.6 more bandwidth that can be processed. In figure 1.10 the bandwidth processing performance for all three cases is plotted. Both algorithms have the same performance for the bandwidths tested, the only difference being that the two frequency shifted monochromatic signals based algorithm is computationally slightly less expensive (see section 2.5).

1.8 List of Appended Papers

1. **Section 2.2: Conference Paper - Spatial Filtering of Near-Field Radio Frequency Interference at a LOFAR LBA Station**
   This paper was presented at the RFI 2016 Conference in Socorro, New

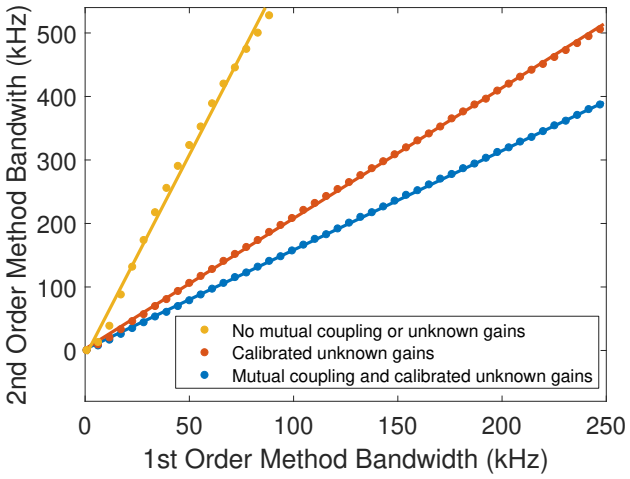

Figure 1.10: To evaluate the proposed algorithms, a DAB signal captured by a software defined radio was used. The DAB signal was delayed by the appropriate amount for each antenna in the LOFAR HBA station RS407. A plot of the bandwidth required by the proposed algorithms as a function of the bandwidth of a first order orthogonal projector to achieve the same attenuation for three cases: there is no mutual coupling or unknown gains, there are unknown gains that have been calibrated for and finally unknown gains that have been calibrated for and mutual coupling. Reproduced from journal paper in section 2.6.

Mexico and published as part of the conference proceedings on IEEE Xplore. Four spatial RFI mitigation techniques are applied to LOFAR LBA data where a hexacopter is broadcasting a signal and moving in the near-field. The different techniques are benchmarked against each other.

2. **Section 2.3: Conference Paper - Computationally Efficient Near-field Radio Frequency Source Localization**
   This paper was presented at the 32nd URSI GASS Conference in Montreal, Canada and published as part of the conference proceedings on IEEE Xplore. In this paper, a new near-field localization algorithm for interferometric arrays with low array beam side-lobes, is presented.

3. **Section 2.4: Journal Paper - Computationally Efficient Source Localization for Radio Interferometric Arrays**
   This journal paper was originally submitted to the student paper competition at the 32nd URSI GASS Conference in Montreal, Canada and was selected as one of the top ten papers. This paper expands the algorithm in section 2.3 by adding far-field source localization, a way to reduce the algorithms memory requirement, improving the algorithms performance for RFI sources on the horizon and a performance comparison with 3-D MUSIC. The source localization algorithm is tested on simulated as well

as real data from a LOFAR LBA station.

4. **Section 2.5: Journal Paper - Mitigation of Non-Narrowband Radio Frequency Interference**
   This journal paper was originally submitted to the student paper competition at the 2nd URSI AT-RASC Conference in Gran Canaria, Spain. The paper won the first prize in the competition and an invitation to publish in the Radio Science Bulletin was extended. The paper has been submitted and is awaiting publication. In this paper, a new non-narrowband RFI mitigation algorithm is presented. An equation is derived which gives the direction of arrival for a far-field non-narrowband signal that causes the greatest distortion of the visibilities. Another equation is derived for the appropriate frequency channel bandwidth at which to implement the proposed non-narrowband RFI mitigation algorithm. The algorithm is tested using real DAB data that is delayed to simulate the effect of a signal being detected by an array.

5. **Section 2.6: Journal Paper - Mitigation of Non-Narrowband Radio Frequency Interference Incorporating Array Imperfections**
   The paper has been submitted to a special issue of the Journal of Astronomical Instrumentation on Interference Mitigation Techniques in Radio Astronomy and is awaiting review. This paper extended the algorithm in section 2.5 by including the effect of unknown complex gains as well as mutual coupling on the signal model. A gain calibration step is also added to the algorithm.

1.9 Conclusion

The overarching aim of the research conducted was to contribute to the localization and mitigation of RFI which contaminates interferometer measurements in radio astronomy.

The near- and far-field localization algorithm developed has computational complexity that is linear with search grid size compared to cubic scaling for 3-D MUSIC. However, it does require the storing of weighting matrices and the array beam side-lobes must be sufficiently low so that the integrating out variables stage finds the correct peak. The algorithm predominantly makes use of simple linear algebra operations, therefore, in future work, the algorithm can be parallelized. Furthermore, a quantitative criterion can be developed to determine for which arrays the algorithm would work.

The non-narrowband RFI mitigation algorithm developed is a second order filter that consists of a first order subspace subtraction method with a non-narrowband signal model. In the simulations conducted, the non-narrowband RFI mitigation algorithm had superior performance relative to the first and

second order subspace subtraction methods. The algorithm was also improved by including a calibration step. Furthermore, the effect of mutual coupling was studied and, in future work, it should be explored whether the algorithm can be extended to take mutual coupling into account. One limitation of the algorithm is that it is designed for signals with a relatively flat frequency response (such as DAB signals). Therefore, the non-narrowband signal model can, in future, be updated for signals with different frequency responses.

Bibliography

[1] Abbott, B. P., e.a.: Gw170817: Observation of gravitational waves from a binary neutron star inspiral. *Phys. Rev. Lett.*, vol. 119, p. 161101, Oct 2017.
Available at: `https://link.aps.org/doi/10.1103/PhysRevLett.119.161101`

[2] Dewdney, P.E., Hall, P.J., Schilizzi, R.T. and Lazio, T.J.L.W.: The Square Kilometre Array. *Proceedings of the IEEE*, vol. 97, no. 8, pp. 1482–1496, August 2009.

[3] van Haarlem, M. P., e.a.: LOFAR: The Low Frequency Array. *Astronomy & Astrophysics*, vol. 556, pp. 1–53, 2013.

[4] Wootten, A. and Thompson, A.R.: The Atacama Large Millimeter/Submillimeter Array. *Proceedings of the IEEE*, vol. 97, no. 8, pp. 1463–1471, Aug 2009. ISSN 0018-9219.

[5] Grimm, V., Riedel, F. and Wolfstetter, E.: The third generation (UMTS) spectrum auction in Germany. *CESifo Working Paper Series*, vol. 584, 2001.
Available at: `https://ssrn.com/abstract=287846`

[6] Ekers, R.: The history of the Square Kilometre Array (SKA) born global. *Proceedings of Resolving The Sky Radio Interferometry: Past, Present and Future*, pp. 1–11, December 2012.
Available at: `https://arxiv.org/abs/1212.3497`

[7] Davidson, D.B.: MeerKAT and SKA phase 1. *ISAPE2012*, pp. 1279–1282, 2012.

[8] Thompson, A.R., Moran, J.M. and Swenson, G.W.: *Interferometry and Synthesis in Radioastronomy*. 2nd edn. Wiley, 2001.

[9] Wilson, T., Rohlfs, K. and Huttemeister, S.: *Tools of Radio Astronomy*. Springer, 2009.

[10] Cornwell, T. and Perley, R.: Radio-interferometric imaging of very large fields. *Astronomy and Astrophysics*, vol. 261, pp. 353–364, 1992.

[11] Hellbourg, G.: *Radio Frequency Interference Spatial Processing for Modern Radio Telescopes*. Ph.D. thesis, University of Orleans, 2014.

[12] Leshem, A., van der Veen, A.J. and Boonstra, A.: Multichannel interference mitigation techniques in radio astronomy. *Astrophys. J. Suppl*, vol. 131, pp. 355–374, 2000.

[13] Raza, J., Boonstra, A. and van der Veen, A.: Spatial filtering of RF interference in radio astronomy. *IEEE Signal Processing Letters*, vol. 9, no. 2, pp. 64–67, February 2002.

[14] van der Tol, S. and van der Veen, A.: Performance analysis of spatial filtering of RF interference in radio astronomy. *IEEE Transactions on Signal Processing*, vol. 53, no. 3, pp. 896–910, February 2005.

[15] van der Veen, A., Leshem, A. and Boonstra, A.: Signal processing for radio astronomical arrays. *IEEE Sensor Array and Multichannel Signal Processing Workshop*, pp. 1–10, July 2004.

[16] Boonstra, A.: *Radio Frequency Interference Mitigation in Radio Astronomy.* Ph.D. thesis, Delft University of Technology, 2005.

[17] Kay, S.: *Fundamentals of Statistical Signal Processing, Volume I: Estimation Theory.* Prentice-Hall, 1993.

[18] Meyer, C.D.: *Matrix Analysis and Applied Linear Algebra.* SIAM: Society for Industrial and Applied Mathematics, 2001.

[19] Harman, H.H.: *Modern Factor Analysis.* The University of Chicago Press, 1968.

[20] Landon, J., Brian, J.D. and Warnick, K.F.: Model-based subspace projection beamforming for deep interference nulling. *IEEE Transactions on Signal Processing*, 2012.

[21] Lisha, L. and Warnick, K.F.: Auxiliary antenna-assisted interference mitigation for radio astronomy arrays. *IEEE Transactions on Signal Processing*, 2005.

[22] Wagner, J.: C++ beamformer library with RFI mitigation. Tech. Rep., Max Planck Institute for Radio Astronomy, 2011.

[23] Akaike, H.: Information theory and an extension of the maximum likelihood principle. *Proc. 2nd Int. Symp. Inf. Theory*, pp. 267–281, 1973.

[24] Wax, M. and Ziskind, I.: Detection of the number of coherent signals by the MDL principle. *IEEE Trans. Acoust., Speech, Signal Process.*, vol. 37, no. 7, pp. 1190–1196, Aug 1989.

[25] Bartlett, M.S.: Tests of significance in factor analysis. *British Journal of Statistical Psychology*, vol. 3, pp. 77–85, 1950.

[26] Balanis, C.A. and Ioannides, P.I.: *Introduction to smart antennas.* Morgan & Claypool Publishers, 2007.

[27] Starer, D. and Nehorai, A.: Passive localization of near-field sources by path following. *IEEE Transactions on Signal Processing*, vol. 42, no. 3, pp. 677–680, 1994.

[28] Weiss, A.J. and Friedlander, B.: Range and bearing estimation using polynomial rooting. *IEEE Journal of Oceanic Engineering*, vol. 18, no. 2, pp. 130–137, 1993.

[29] Grosicki, E., Abed-Meraim, K. and Hua, Y.: A weighted linear prediction method for near-field source localization. *IEEE Transactions on Signal Processing*, vol. 53, no. 10, pp. 3651–3660, 2005.

[30] Yuen, N. and Friedlander, B.: Performance analysis of higher order ESPRIT for localization of near-field sources. *IEEE Transactions on Signal Processing*, vol. 46, no. 3, pp. 709–719, 1998.

[31] Challa, R. and Shamsunder, S.: High-order subspace-based algorithms for passive localization of near-field sources. *Conference Record of The Twenty-Ninth Asilomar Conference on Signals, Systems and Computers*, vol. 2, pp. 777–781, 1995.

[32] Huang, Y.D. and Barkat, M.: Multiple source localization by passive sensor array. *IEEE Transactions on Antennas and Propagation*, vol. 39, no. 7, pp. 968–975, 1991.

[33] Hung, H., Chang, S. and Wu, C.: 3-d MUSIC with polynomial rooting for near-field source localization. In: *IEEE International Conference on Acoustics, Speech, and Signal Processing Conference Proceedings*, vol. 6, pp. 3065–3068. 1996.

[34] Chen, J.C., Hudson, R.E. and Yao, K.: Maximum-likelihood source localization and unknown sensor location estimation for wideband signals in the near-field. *IEEE Transactions on Signal Processing*, vol. 50, no. 8, pp. 1843–1854, 2002.

[35] Tung, T.L., Yao, K., Chen, D., Hudson, R.E. and Reed, C.W.: Source localization and spatial filtering using wideband MUSIC and maximum power beamforming for multimedia applications. *1999 IEEE Workshop on Signal Processing Systems. SiPS 99. Design and Implementation (Cat. No.99TH8461)*, pp. 625–634, 1999.

[36] Zatman, M.: How narrow is narrowband? *IEE Proceedings-Radar, Sonar and Navigation*, vol. 2, no. 145, pp. 85–91, 1998.

Chapter 2

Papers

2.1 IEEE Copyright

As required by IEEE policy, the following conditions apply to IEEE copyrighted material: in reference to IEEE copyrighted material which is used with permission in this thesis, the IEEE does not endorse any of Stellenbosch University's products or services. Internal or personal use of this material is permitted. If interested in reprinting/republishing IEEE copyrighted material for advertising or promotional purposes or for creating new collective works for resale or redistribution, please go to `http://www.ieee.org/publications\_standards/publications/rights/rights\_link.html` to learn how to obtain a License from RightsLink. If applicable, University Microfilms and/or ProQuest Library, or the Archives of Canada may supply single copies of the dissertation.

2.2 Conference Paper - Spatial Filtering of Near-Field Radio Frequency Interference at a LOFAR LBA Station

SPATIAL FILTERING OF NEAR-FIELD RADIO FREQUENCY INTERFERENCE AT A LOFAR LBA STATION

Jan-Willem W. Steeb, David B. Davidson *

Department of Electrical and Electronic Engineering
Stellenbosch University
Stellenbosch, South Africa
davidson@sun.ac.za

Stefan J. Wijnholds

R&D Department
ASTRON
Dwingeloo, The Netherlands
wijnholds@astron.nl
and Dept E&E Eng,
Stellenbosch University

ABSTRACT

In preparation for the SKA, many new RFI (radio frequency interference) mitigation algorithms have been developed. However, these algorithms usually assume that the RFI source is in the far-field and that the array is calibrated. In this paper, the recovery of astronomical signals from uncalibrated RFI-corrupted LOFAR visibility data using spatial filtering methods are presented. For this demonstration, a near-field continuous-wave RFI source was generated by a hexacopter that was flown around one of the LOFAR LBA (low-band antenna) arrays. Four spatial filtering methods were applied to the RFI contaminated data: orthogonal projection, orthogonal projection with subspace bias correction, oblique projection and subspace subtraction. Overall, orthogonal projection with subspace bias correction performed the best, however it requires that the RFI source moves relative to the array and it is computationally expensive. Oblique projection performs similar to orthogonal projection with subspace bias correction when point sources are to be recovered and is furthermore considerably less computationally expensive. Subspace subtraction is a suitable alternative if a large field of view is to be recovered at a relatively low computational cost.

Index Terms— RFI mitigation, LOFAR, near-field RFI, spatial filtering.

1. INTRODUCTION

LOFAR is part of a new generation of radio telescope arrays with large bandwidths, high sensitivity and resolution. To obtain high resolutions long baselines are required and therefore most RFI sources will be in the near-field. Consequently, powerful near-field RFI presents a serious challenge. In this paper the application of spatial RFI mitigation techniques to uncalibrated data which has been corrupted with a near-field source is presented. The experimental setup is explained, followed by a description of the mathematical model and applied RFI mitigation techniques. Finally, the experimental results are given.

2. EXPERIMENTAL SETUP

For this demonstration, a near-field continuous-wave RFI source was generated by a hexacopter that was flown around the LOFAR LBA (low-band antenna) array CS302. A signifcant feature of this test is that the hexacopter's flight path was within the array's near-field. The Rayleigh distance for a LOFAR station is approximately 1900 m for a given longest baseline of approximately 85 m and a wavelength of 6.74 m (the sub-band with centre frequency 44.5095 MHz was used).

3. MODEL

The following general model (used in [1, 2, 3, 4, 5]) is considered for the output generated at time t by an antenna array that consists of N_e elements, for one polarization and frequency channel:

$$\mathbf{y}(t) = \mathbf{g} \odot (\mathbf{x}_c(t) + \mathbf{x}_r(t)) + \mathbf{x}_n(t) \quad (1)$$

*This work is supported by SKA South Africa, the South African Research Chairs Initiative of the Department of Science and Technology, the National Research Foundation, and a Marie Curie International Research Staff Exchange Scheme Fellowship within the 7th European Community Framework Programme MIDPREP, Grant Agreement PIRSES-GA-2013-612599.
The authors would like to thank Millad Sardarabadi for the fruitful discussions and useful feedback.

where
- $\mathbf{y}(t)$ is an $N_e \times 1$ vector of measured array output signals,
- $\mathbf{g}$ is the vector of complex gains for each antenna,
- $\odot$ Hadamard product,
- $\mathbf{x}_c(t)$ is the vector where each element is the sum of N_c delayed cosmic signals for a given antenna,
- $\mathbf{x}_r(t)$ is the vector where each element is the sum of N_r delayed RFI signals for a given antenna,
- $\mathbf{x}_n(t)$ is the vector of instrumental noise for each antenna.

The gains $\mathbf{g}$ are unknown, since the array is assumed to be uncalibrated.

The frequency channel is assumed to be sufficiently narrowband, so that the time delays τ can be represented as phase delays. Therefore, a delayed signal can be approximated by $s(t-\tau) \approx s(t)e^{-i2\pi\nu_0\tau}$, where ν_0 is the centre frequency of the channel. This condition is satisfied for the array, if $2\pi\Delta\nu\tau_{max} \ll 1$, where $\Delta\nu$ is the signal's bandwidth and τ_{max} is the delay given by the longest baseline (greatest distance between any two antennas) [6].

The phase delays for the k^{th} RFI source can be stacked into a vector that is called the geometric delay vector

$$\mathbf{a}_{r_k} = \begin{bmatrix} e^{-i2\pi\nu_0\tau_{1r_k}} \\ \vdots \\ e^{-i2\pi\nu_0\tau_{N_e r_k}} \end{bmatrix}. \tag{2}$$

An $N_e \times N_r$ matrix can now be constructed from the geometric delay vectors, $\mathbf{A}_r = [\mathbf{a}_{r_1} \dots \mathbf{a}_{r_{N_r}}]^T$ (the same applies for the cosmic signals, $\mathbf{A}_c = [\mathbf{a}_{c_1} \dots \mathbf{a}_{c_{N_c}}]^T$), and therefore the model in equation 1 can be written as

$$\mathbf{y}(t) = \mathbf{g} \odot (\mathbf{A}_c\mathbf{s}_c(t) + \mathbf{A}_r\mathbf{s}_r(t)) + \mathbf{x}_n(t), \tag{3}$$

where $\mathbf{s}_c(t)$ and $\mathbf{s}_r(t)$ are respectively, the vectors of the cosmic and RFI signals without delays.

The zero lag covariance matrix (the ij^{th} element of the matrix is the covariance of the i^{th} and j^{th} antenna [7, p. 501]) of the vectorised data model in equation 1 is given by

$$\mathbf{R} = \mathbb{E}\{\mathbf{y}(t)\mathbf{y}^H(t)\}, \tag{4}$$

where $\mathbb{E}$ is the expectation, ^{H} is the Hermitian transpose or complex conjugate transpose and it is assumed that for a given time period none of the signals change position. Therefore, the covariance is constant over this time period as long as the signals are themselves stationary.

Independence between the cosmic, RFI and noise sources is assumed, therefore, when substituting equation 3 into equation 4 the expectation of any non-self multiplication terms is zero and consequently the substitution yields

$$\begin{aligned} \mathbf{R} &= \mathbf{G}(\mathbf{R}_c + \mathbf{R}_r)\mathbf{G}^H + \mathbf{R}_n \\ &= \mathbf{G}(\mathbf{A}_c\mathbf{B}_c\mathbf{A}_c^H + \mathbf{A}_r\mathbf{B}_r\mathbf{A}_r^H)\mathbf{G}^H + \mathbf{R}_n, \end{aligned} \tag{5}$$

where $\mathbf{B}_c = \mathbb{E}\{\mathbf{s}_c(t)\mathbf{s}_c^H(t)\}$, $\mathbf{B}_r = \mathbb{E}\{\mathbf{s}_r(t)\mathbf{s}_r^H(t)\}$, $\mathbf{R}_n = \mathbb{E}\{\mathbf{x}_n(t)\mathbf{x}_n^H(t)\}$ and $\mathbf{G}$ is the diagonal matrix of $\mathbf{g}$. The matrices $\mathbf{B}_c$ will be diagonal if the cosmic signals are uncorrelated and the same applies to $\mathbf{B}_r$ and $\mathbf{R}_n$ if the RFI and noise signals are, respectively, uncorrelated. Since the signals are spatially and temporally stationary, the covariance matrix is estimated by

$$\widehat{\mathbf{R}} = \frac{1}{N_t}\sum_{i=1}^{N_t}\mathbf{y}(iT_s)\mathbf{y}^H(iT_s), \tag{6}$$

where
- $\widehat{\mathbf{R}}$ is the estimated covariance matrix,
- N_t is the number of samples for which the signals are stationary,
- T_s is the sample time.

The covariance matrix has the following useful properties: $\mathbf{R}$ is Hermitian and is positive semi-definite [8, p. 558].

4. SPATIAL RFI MITIGATION

4.1. Orthogonal Projection

If the columns of $\mathbf{A}_r$ are linearly independent, they form a basis for a vector space V_r. Therefore, an orthogonal projector can be constructed [8, p. 430] which projects along V_r onto a vector space orthogonal to V_r , namely

$$\mathbf{P} = \mathbf{I} - \mathbf{A}_r(\mathbf{A}_r^H\mathbf{A}_r)^{-1}\mathbf{A}_r^H, \tag{7}$$

such that $\mathbf{PA}_r = \mathbf{0}$. The projector is Hermitian and therefore $\mathbf{P} = \mathbf{P}^H$ [8, p. 433]. Applying the projector to equation 5 yields (assuming $\mathbf{G} = \mathbf{I}$)

$$\begin{aligned} \mathbf{PRP} =& \mathbf{PR}_c\mathbf{P} + \mathbf{PA}_r\mathbf{B}_r\mathbf{A}_r^H\mathbf{P} + \mathbf{PR}_n\mathbf{P} \\ =& \mathbf{PR}_c\mathbf{P} + \mathbf{PR}_n\mathbf{P} \\ =& \mathbf{PR}_{cn}\mathbf{P}. \end{aligned} \tag{8}$$

The RFI contribution to the covariance is completely nulled; however, the noise and cosmic signals are biased.

4.2. Orthogonal Projection with Subspace Bias Correction

For any useful orthogonal projector $\mathbf{P}$ the kernel basis includes the zero vector and at least one non-zero vector, therefore, $\mathbf{P}$ has a column rank less than the number of columns in $\mathbf{P}$ which consequently makes the matrix singular. The orthogonal projection method bias (see equation 8) can therefore not be corrected by multiplying with the inverted orthogonal projector.

For the orthogonal projection correction scheme ([2, 3, 4]) the number of samples N_t is divided into N_G equally sized groups, where each group consists of N_{st} samples (st denotes short term), that is, $N_t = N_G N_{st}$. For a sampling time T_s the overall integration time is $N_t T_s$, while $N_{st}T_s$ is the short term integration time for any of the N_G groups. The following assumptions must also hold:

- The cosmic signals are stationary for $N_t T_s$ seconds.
- The RFI signals are stationary for $N_{st} T_s$ seconds.
- The RFI signals are not stationary for $N_t T_s$ seconds.

The k^{th} short term covariance matrix estimate is given by

$$\widehat{\mathbf{R}}_k = \frac{1}{N_{st}} \sum_{n=(k-1)N_{st}+1}^{kN_{st}} \mathbf{y}(nT_s)\mathbf{y}(nT_s)^H \tag{9}$$

where $k \in \{1, \cdots, N_G\}$. The covariance matrix estimate can then be written as

$$\widehat{\mathbf{R}} = \frac{1}{N_G} \sum_{k=1}^{N_G} \widehat{\mathbf{R}}_k. \tag{10}$$

For each short term integration covariance matrix estimate $\widehat{\mathbf{R}}_k$, an orthogonal RFI projector $\mathbf{P}_k$, can be constructed, since the RFI is assumed stationary over the short term integration time ($N_{st} T_s$). The averaged orthogonal projected covariance matrix estimate is then

$$\begin{aligned}
\widehat{\mathbf{R}}_{orth} =& \frac{1}{N_G} \sum_{k=1}^{N_G} \mathbf{P}_k \widehat{\mathbf{R}}_k \mathbf{P}_k \\
=& \frac{1}{N_G} \sum_{k=1}^{N_G} \mathbf{P}_k (\widehat{\mathbf{R}}_c + \widehat{\mathbf{R}}_{k,r} + \widehat{\mathbf{R}}_n) \mathbf{P}_k \\
=& \frac{1}{N_G} \sum_{k=1}^{N_G} \mathbf{P}_k (\widehat{\mathbf{R}}_c + \widehat{\mathbf{R}}_n) \mathbf{P}_k \\
=& \frac{1}{N_G} \sum_{k=1}^{N_G} \mathbf{P}_k (\widehat{\mathbf{R}}_{cn}) \mathbf{P}_k.
\end{aligned} \tag{11}$$

Applying the matrix identity

$$\mathbf{vec}(\mathbf{ABC}) \equiv (\mathbf{C}^T \otimes \mathbf{A})\mathbf{vec}(\mathbf{B}), \tag{12}$$

where $\mathbf{vec}(\cdot)$ indicates the stacking of column vectors of a matrix and $\otimes$ the Kronecker product, to equation 11 yields

$$\begin{aligned}
\mathbf{vec}(\widehat{\mathbf{R}}_{orth}) &= \frac{1}{N_G} \sum_{k=1}^{N_G} (\mathbf{P}_k^T \otimes \mathbf{P}_k) \mathbf{vec}(\widehat{\mathbf{R}}_{cn}) \\
&= \left\{ \frac{1}{N_G} \sum_{k=1}^{N_G} (\mathbf{P}_k^T \otimes \mathbf{P}_k) \right\} \mathbf{vec}(\widehat{\mathbf{R}}_{cn}) \\
&= \mathbf{C}\mathbf{vec}(\widehat{\mathbf{R}}_{cn}).
\end{aligned} \tag{13}$$

The RFI is however assumed to be non-stationary over the total integration time $N_t T_s$, therefore, $\mathbf{P}_k$ will vary between the short term integration groups. The matrix $\mathbf{C}$ becomes non-singular if N_G is large enough and the orthogonal projectors vary sufficiently. The corrected covariance matrix is then

$$\widehat{\mathbf{R}}_{cn} = \mathbf{unvec}(\mathbf{C}^{-1}\mathbf{vec}(\widehat{\mathbf{R}}_{orth})), \tag{14}$$

where the $\mathbf{unvec}(\cdot)$ operator is the inverse of the $\mathbf{vec}(\cdot)$ operator in equation 12.

4.3. Oblique Projection

The oblique projection method projects along the RFI vector space V_r onto the cosmic vector space V_c. To construct this oblique projector it is required that the column vectors in $[\mathbf{A}_c \mathbf{A}_r]$ are independent ($V_r \cap V_c = \{\mathbf{0}\}$). The oblique projector is given by [1, p. 51]

$$\boldsymbol{E}_{V_r \to V_c} = \mathbf{A}_c (\mathbf{A}_c^H \mathbf{P}_{V_r}^{\perp} \mathbf{A}_c)^{-1} \mathbf{A}_c^H \mathbf{P}_{V_r}^{\perp}, \tag{15}$$

where $\mathbf{P}_{V_r}^{\perp}$ is an orthogonal projector which projects along V_r onto a vector space that is orthogonal to V_r. When an oblique projector is applied, the RFI is nulled and the cosmic signal is recovered, however the noise is biased

$$\begin{aligned}
\mathbf{R}_{obl} &= \boldsymbol{E}_{V_r \to V_c} \mathbf{R} \boldsymbol{E}_{V_r \to V_c}^H \\
&= \mathbf{R}_c + \boldsymbol{E}_{V_r \to V_c} \mathbf{R}_n \boldsymbol{E}_{V_r \to V_c}^H.
\end{aligned} \tag{16}$$

For the case when V_r and V_c are orthogonal, the oblique and orthogonal projectors are equivalent. The basis for V_c can be constructed from either a skymap or choosing an area of interest that does not contain the RFI.

4.4. Subspace Subtraction

If the power and the geometric delay vectors of the RFI sources are known, then the effect of the RFI sources can be subtracted [5, p. 115]

$$\mathbf{R}_{cn} = \mathbf{R} - \sum_{i=1}^{N_r} \sigma_i^2 \mathbf{a}_i \mathbf{a}_i^H. \tag{17}$$

The power of the RFI source and a basis for the geometric delay vectors can be estimated by using factor analysis, see section 4.5.

4.5. RFI Subspace Estimation

Any basis of the RFI subspace V_r can be used to construct the aforementioned projectors, not just $\mathbf{A}_r$. The ability of the projection and subtraction methods to null the contribution of RFI is dependent on the accuracy of the estimate of a basis set that spans the vector space V_r. When the direction of arrival of the RFI is not known, $\mathbf{A}_r$ cannot be calculated. However, an orthogonal set of eigenvectors can be found by applying eigenvalue decomposition (EVD) to the covariance matrix, because the covariance matrix is positive semi-definite [8, p. 517]. If it can be assumed that the cosmic signal contribution can be ignored, that the noise is independently and identically distributed and that the RFI signals are uncorrelated, then the EVD of the covariance matrix yields [1, p. 64-65]

$$
\begin{aligned}
\mathbf{R} \approx & \mathbf{R}_r + \mathbf{D}_n \\
= & \begin{bmatrix} \mathbf{M}_r & \mathbf{K}_r \end{bmatrix} \begin{bmatrix} \mathbf{D}_r & \mathbf{0} \\ \mathbf{0} & \mathbf{0} \end{bmatrix} \begin{bmatrix} \mathbf{M}_r^H \\ \mathbf{K}_r^H \end{bmatrix} + \sigma_n^2 \mathbf{I} \\
= & \begin{bmatrix} \mathbf{M}_r & \mathbf{K}_r \end{bmatrix} \mathbf{D}_{rn} \begin{bmatrix} \mathbf{M}_r^H \\ \mathbf{K}_r^H \end{bmatrix} \\
= & \begin{bmatrix} \mathbf{M}_r & \mathbf{K}_r \end{bmatrix} \begin{bmatrix} \mathbf{D}_r + \sigma_n^2 \mathbf{I}_{N_r} & \mathbf{0} \\ \mathbf{0} & \sigma_n^2 \mathbf{I}_{N_e - N_r} \end{bmatrix} \begin{bmatrix} \mathbf{M}_r^H \\ \mathbf{K}_r^H \end{bmatrix}, \quad (18)
\end{aligned}
$$

where

$\mathbf{M}_r$ is the eigenvectors that form the range of V_r,
$\mathbf{K}_r$ is the eigenvectors that form the kernel of V_r,
$\mathbf{D}_r$ is the matrix of eigenvalues ($\lambda_{r,j}$) for $\mathbf{R}_r$,
$\mathbf{D}_{rn}$ is the matrix of eigenvalues (λ_j) for $\mathbf{R}$.

The column vectors of $\mathbf{M}_r$ are orthogonal as well as those of $\mathbf{K}_r$. For the case where there are two or more RFI signals it is unlikely that $\mathbf{M}_r$ will be equal to $\mathbf{A}_r$. Therefore, the vector space V_r is spanned differently and the eigenvalues $\lambda_{r,j}$ will not be equal to the RFI powers $\sigma_{r,j}^2$ (however the total power will be the same). The noise only affects the eigenvalues of $\mathbf{R}_r$ but not its eigenvectors, because the noise is identically distributed [1, p. 65].

The orthogonal projector in equation 7 can now be constructed using $\mathbf{M}_r$, which is identified by the larger eigenvalues in $\mathbf{D}_{rn}$. One simple method [9] to identify the RFI is to count the eigenvalues which exceed three median absolute deviations from the median

$$
\lambda_j > 3 \cdot \text{median}(|\mathbf{D}_{rn} - \text{median}(\mathbf{D}_{rn})|) + \text{median}(\mathbf{D}_{rn}), \quad (19)
$$

where λ_j is the j^{th} eigenvalue contained in $\mathbf{D}_{rn}$. Using the median lessens the influence of outliers, that is, the values affected by the RFI. Alternative methods are given in [10, 11, 12].

If the noise is not identically distributed, then adding the noise covariance matrix $\mathbf{R}_n = \mathbf{diag}(\sigma_{n,1}^2, \ldots, \sigma_{n,n_e}^2)$ to the RFI covariance matrix $\mathbf{R}_r$ causes the eigenvectors[1] of the sum to change [1, p. 64-65].

When the instrumental noise is not calibrated for an interferometer, factor analysis [13] can be used. Factor analysis is a statistical method that decomposes a $p \times p$ covariance matrix, that is, $\mathbf{R} = \mathbf{Z}\mathbf{Z}^H + \mathbf{D}$, where $\mathbf{Z}$ is a $p \times q$ matrix and $\mathbf{D}$ is a $p \times p$ diagonal matrix. Applying this decomposition to an interferometer's covariance (the influence of the cosmic source is considered negligible) yields

$$
\begin{aligned}
\mathbf{R} = & \mathbf{Z}\mathbf{Z}^H + \mathbf{D} \\
= & \mathbf{R}_r + \mathbf{R}_n. \quad (20)
\end{aligned}
$$

This method places a restriction on the number of factors (that is interferers), namely $q < (p - \sqrt{p})$ [4, 13].

[1] However, if the power of the RFI is much larger than the noise power ($\sigma_{r,i}^2 \gg \sigma_{n,i}^2$), the effect of noise on the RFI covariance matrix's eigenvalues will diminish.

5. EXPERIMENTAL RESULTS

To show the effect of the spatial RFI mitigation methods, full sky dirty images were created by classical delay beamforming [1, p. 36] on each pixel. In figure 1 the RFI source is clearly seen at the top and its intensity is chosen as the 0 dB point. Data was also saved when the hexacopter was switched off and a ground truth image was created, see figure 2. In the ground truth image Cassiopeia A (the brightest source) and Cygnus A are clearly seen. When the orthogonal projector is applied it is seen in figure 3 that the strong cosmic sources are recovered, however, there is a null in the position where the RFI source was. Orthogonal projection with subspace bias correction recovers the information that was lost due to the orthogonal projection, as seen in figure 4. For the oblique projector a skymap was chosen that consists of Cassiopeia A and Cygnus A, see figure 5. The oblique projector recovers what was specified in the skymap and nulls everything else. Subspace subtraction seems to perform similarly to orthogonal projection with bias correction, however the reliability of the information recovered in the position of the RFI can be questioned, since this method effectively replaces the null with noise, see figure 6.

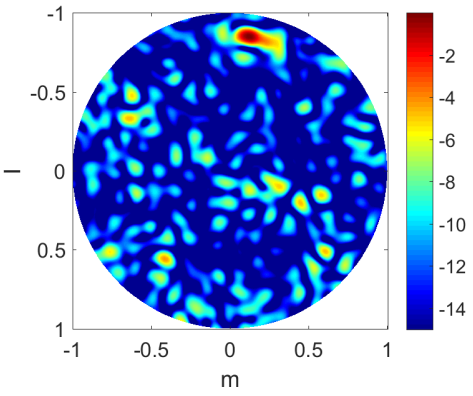

Fig. 1: Full skymap with RFI source visible at the top right in dB. All other sources are drowned in the sidelobe response of the RFI source. The power of the cosmic sources are at least 39 dB below that of the RFI source. The scale is set to saturate at -15 dB so that the RFI source is clearly visible.

As a figure of merit the Mean Absolute Percentage Error was chosen

$$
\mathbf{MAPE} = 100 \sum_i^{N_e} \sum_j^{N_e} \frac{|\widehat{\mathbf{R}}_{proj,i,j} - \widehat{\mathbf{R}}_{clean,i,j}|}{|\widehat{\mathbf{R}}_{clean,i,j}|} \quad (21)
$$

where $\widehat{\mathbf{R}}_{proj,i,j}$ is the ij^{th} element of the covariance matrices recovered with a spatial filtering method and $\widehat{\mathbf{R}}_{clean}$ is the ij^{th} element of the covariance matrix estimated from the data where the hexacopter is switched off. The results are given in

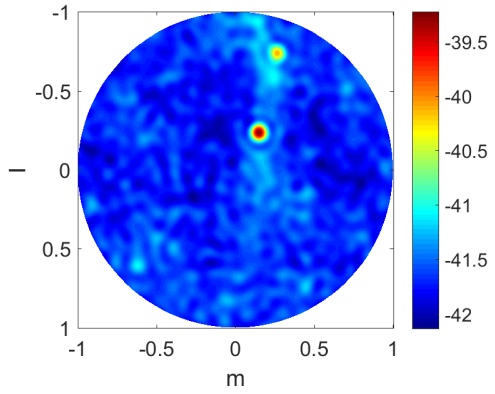

Fig. 2: Full skymap without RFI source in dB.

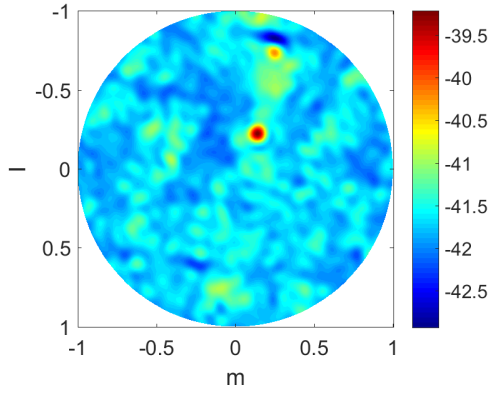

Fig. 3: Full skymap with RFI source removed using orthogonal projection in dB.

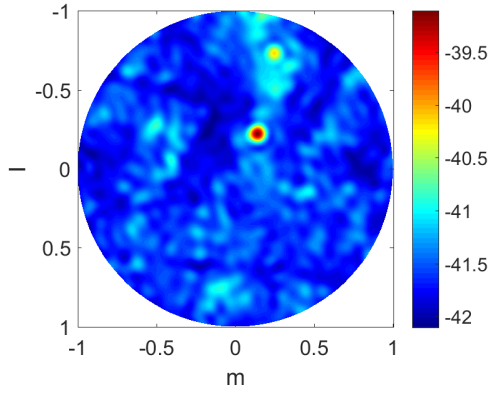

Fig. 4: Full skymap with RFI source removed using orthogonal projection with bias correction in dB.

a bar graph in figure 7. To make the comparison more meaningful the MAPE is also calculated between two different time step covariance matrices for when the hexacopter is switched

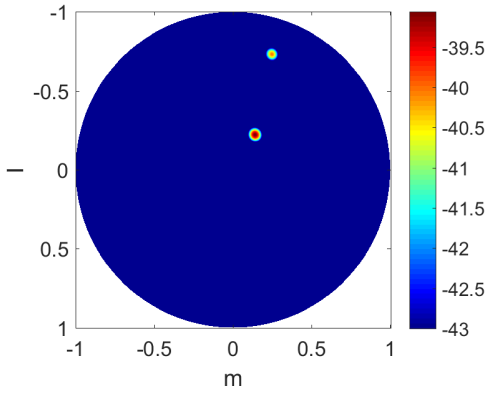

Fig. 5: Full skymap with RFI source removed using Oblique Projection in dB. The scale is set to saturate at -43 dB so that the recovered sources are clearly visible.

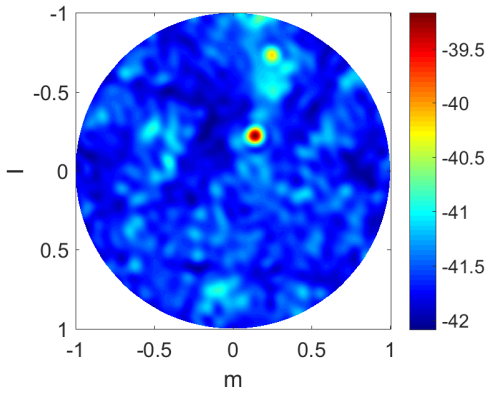

Fig. 6: Full skymap with RFI source removed using subspace subtraction.

off (this is labelled as clean). Any mitigation method that has a MAPE close to the clean MAPE is considered to have recovered the ground truth successfully. The orthogonal projector with subspace bias correction performs the best, however it is computationally the most expensive. The subspace subtraction method also performs well in recovering the ground truth. The oblique projector performs the poorest, since it was implemented only to recover the two bright cosmic sources.

To measure the ability of the mitigation methods to recover a source's power, the power of Cassiopia A in the RFI mitigated images is compared to that of the RFI free sky image, see figure 8. The percentage error in power is also calculated between two different time step images for when the hexacopter is switched off (this is labelled as clean). The oblique projector and orthogonal projection with subspace bias correction methods performs the best. However, all of the methods produced results with recovered power within 3.5% of the estimate of the source's power.

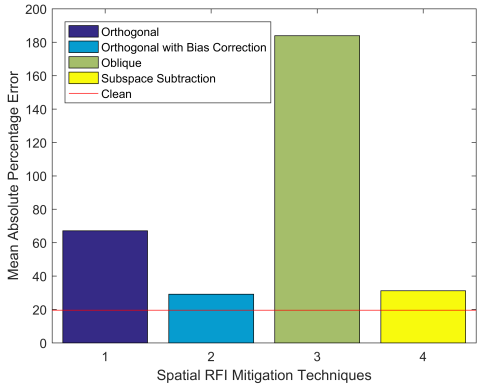

Fig. 7: MAPE of Spatial RFI Mitigation Techniques Covariance Matrices relative to RFI Free Covariance Matrix.

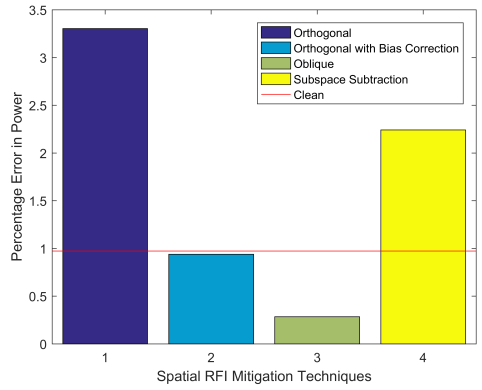

Fig. 8: Percentage error of power for Cassiopeia A.

6. CONCLUSION

The hexacopter signal was 40 dB above the cosmic signals and saturated the entire skymap. All the projection methods that were implemented are able to remove the hexacopter signal and approximately recover the ground truth. If it is assumed that factor analysis is used to determine the RFI subspace, then subspace subtraction has the lowest computational cost (since no projector needs to be constructed) followed by orthogonal projection. The oblique projector which includes first calculating the orthogonal projector and then the oblique projector has an increased computational cost. The orthogonal projector with subspace bias correction has the highest computational cost, because the correction matrix $\mathbf{C}$ must be calculated and inverted. Orthogonal projection with bias correction performs the best in recovering the entire image (this is especially useful when the RFI source is in the desired field of view). The oblique projector performs well when a region is to be recovered where the RFI source is not located.

7. REFERENCES

[1] G. Hellbourg, *Radio Frequency Interference Spatial Processing for Modern Radio Telescopes*, Ph.D. thesis, University of Orleans, 2014.

[2] J. Raza, A. Boonstra, and A. van der Veen, "Spatial filtering of RF interference in radio astronomy," *IEEE SIGNAL PROCESSING LETTERS*, vol. 9, no. 2, pp. 64–67, February 2002.

[3] S. van der Tol and A. van der Veen, "Performance analysis of spatial filtering of RF interference in radio astronomy," *IEEE TRANSACTIONS ON SIGNAL PROCESSING*, vol. 53, no. 3, pp. 896–910, February 2005.

[4] A. van der Veen, A. Leshem, and A. Boonstra, "Signal processing for radio astronomical arrays," *IEEE Sensor Array and Multichannel Signal Processing Workshop*, pp. 1–10, July 2004.

[5] A. J. Boonstra, *Radio Frequency Interference Mitigation in Radio Astronomy*, Ph.D. thesis, Delft University of Technology, 2005.

[6] M. Zatman, "How narrow is narrowband?," *IEEE Proceedings-Radar, Sonar and Navigation*, vol. 2, no. 145, pp. 85–91, 1998.

[7] S. Kay, *Fundamentals of Statistical Signal Processing, Volume I: Estimation Theory*, Prentice-Hall, 1993.

[8] C. D. Meyer, *Matrix Analysis and Applied Linear Algebra*, SIAM: Society for Industrial and Applied Mathematics, 2001.

[9] J. Wagner, "C++ beamformer library with rfi mitigation," Tech. Rep., Max Planck Institute for Radio Astronomy, 2011.

[10] H. Akaike, "Information theory and an extension of the maximum likelihood principle," *Proc. 2nd Int. Symp. Inf. Theory*, pp. 267–281, 1973.

[11] M. Wax and I. Ziskind, "Detection of the number of coherent signals by the mdl principle," *IEEE Trans. Acoust., Speech, Signal Process.*, vol. 37, no. 7, pp. 1190–1196, Aug. 1989.

[12] M. S. Bartlett, "Tests of significance in factor analysis," *British J. Psych.*, vol. 3, pp. 77–85, 1950.

[13] A. M. Sardarabadi, *Covariance Matching Techniques for Radio Astronomy Calibration and Imaging*, Ph.D. thesis, Delft University of Technology, 2016.

2.3 Conference Paper - Computationally Efficient Near-field Radio Frequency Source Localization

32nd URSI GASS, Montreal, 19–26 August 2017

Computationally Efficient Near-field Radio Frequency Source Localisation

Jan-Willem W. Steeb*(1), David B. Davidson(1), and Stefan J. Wijnholds(2)(1)
(1) Department of Electrical & Electronic Engineering, Stellenbosch University, South Africa
(2) Netherlands Institute for Radio Astronomy (ASTRON), The Netherlands

Abstract

Radio frequency interference (RFI) is an ever-increasing problem for remote sensing and radio astronomy, with radio telescope arrays especially vulnerable to RFI. Localising the RFI source is the first step to dealing with the culprit system. In this paper, a new near-field localisation algorithm for interferometric arrays with low array beam side lobes, is presented. The computational complexity of the algorithm is linear with search grid size compared to the 3D MUSIC method which scales with the cube of search grid size. The trade-off is that the algorithm requires a once-off a priori calculation and storing of weighting matrices. The proposed algorithm has the same accuracy as 3D MUSIC.

1 Introduction

Radio frequency interference (RFI) is an important issue in many areas of scientific research, for example in remote sensing and radio astronomy. The ideal solution is to identify the location of the RFI and then remove it. For arrays with a high sensitivity or a large spatial extend, near-field sources are of particular interest. This is particularly true for large radio astronomical arrays such as the Low Frequency Array (LOFAR) [1] and the Square Kilometre Array (SKA) [2], which span entire continents and therefore detect many RFI signals from TV and radio broadcast towers and even satellites in their near-field. This makes these arrays an excellent proving ground for near-field RFI localisation and mitigation methods.

Current near-field source localisation algorithms either make use of brute force methods (such as MUSIC [7, p. 80-82] where the entire solution space is searched) or exploit the array layout (a common layout is a uniform linear array). Methods that exploit a uniform linear array layout include path following [3] and polynomial rooting [4].

For radio astronomy arrays, brute force methods are computationally expensive due to the large near-field area caused by long baselines. Furthermore, to obtain as much information as possible for imaging (optimising the UV coverage) the array layouts are non-uniform and non-linear. However, radio astronomy interferometric arrays have the advantage that the array beam has low side lobe levels. Therefore, a novel computationally efficient near-field source localisation algorithm is presented which is designed for irregular interferometric arrays and takes advantage of low array beam side lobes.

In this paper, the following notation is used:

$\mathbf{A}$	Bold upper-case letters are matrices. The jk^{th} element is indicated by $\mathbf{A}_{jk}$.
$\mathbf{a}$	Bold lower-case letters are column vectors. The j^{th} element is indicated by $\mathbf{a}_j$.
$\mathbf{I}$	Identity matrix.
$\|\|\cdot\|\|$	Norm of a vector.
$\text{Tr}(\cdot)$	Trace of a matrix.
$\text{diag}(\cdot)$	Converts a vector into a diagonal matrix.
$\angle$	Phase of a complex number.
i	Square root of -1.
c	Speed of light.
$\{\cdot\}^H$	Hermitian transpose of a matrix.
$\{\cdot\}^T$	Transpose of a matrix.
$\{\cdot\}^*$	Complex conjugate of a scalar.
$\Re(\cdot)$	Real part of a complex number.
$\Im(\cdot)$	Imaginary part of a complex number.

2 Data Model

The scenario that is considered is where an array is observing astronomical sources and the measurements are contaminated by a single near-field RFI source. This will later be generalised to multiple RFI sources. The assumption is made that the power of the RFI source is considerably higher than the power from the astronomical sources, therefore the astronomical sources are omitted from the model. Direction dependent effects such as path loss, polarisation mismatch factor, the gain of the antennas and atmospheric effects are not considered. Furthermore, direction independent effects such as the receiver electronics, in particular the low noise amplifiers, are also not considered.

To keep the model simple the output of the array will only be considered for a single frequency channel and polarisation. If the array consists of N_e elements, then at time t the voltage output can be expressed as [5]

$$\mathbf{y}(t) = \mathbf{x}_s(t) + \mathbf{x}_n(t), \tag{1}$$

where $\mathbf{y}(t) = [y_1(t), \ldots, y_{N_e}(t)]^T$ is the vector of the measured array output signals, $\mathbf{x}_s(t) = [s(t-\tau_1), \ldots, s(t-\tau_{N_e})]^T$ is the vector of the delayed RFI signal and $\mathbf{x}_n(t) =$

$[n_1(t),\ldots,n_{N_e}(t)]^T$ is the vector of instrumental noise for each antenna.

For the j^{th} antenna, τ_j is the delay between the source location and the array element and is given by $\tau_j = ||\mathbf{v}_s - \mathbf{v}_j||/c$ where $\mathbf{v}_s$ and $\mathbf{v}_j$ are the position vectors of the RFI source and antenna, respectively. The delayed signal can be approximated by $s(t-\tau_j) \approx s(t)e^{-i2\pi\nu\tau_j}$, where ν is the centre frequency of the channel. This condition is satisfied if $2\pi\Delta\nu\tau_{max} \ll 1$ [6], where $\Delta\nu$ is the signal's bandwidth and τ_{max} is the delay given by the longest baseline (greatest distance between any two antennas). The phase delays of the source can be stacked into a vector that is called the geometric delay vector $\mathbf{a}(\mathbf{v}_s) = [e^{i2\pi\nu\tau_1},\ldots,e^{i2\pi\nu\tau_{Ne}}]^T$. Therefore, the model in equation (1) can be written as

$$\mathbf{y}(t) = \mathbf{a}(\mathbf{v}_s)s(t) + \mathbf{x}_n(t). \tag{2}$$

To create images, interferometric radio astronomy arrays need the covariance matrix of the signals $\mathbf{R} = \mathbb{E}\{\mathbf{y}(t)\mathbf{y}^H(t)\}$, where $\mathbb{E}$ is the expectation. Independence is assumed between the RFI source and the noise, therefore, the covariance matrix of equation (2) is $\mathbf{R} = \mathbf{R}_s + \mathbf{R}_n = \mathbf{a}(\mathbf{v}_s)\sigma_s^2\mathbf{a}^H(\mathbf{v}_s) + \mathbf{R}_n$ where $\sigma_s^2 = \mathbb{E}\{s(t)s^*(t)\}$ is the power of the RFI signal. If N_s RFI signals are present, then the covariance matrix is the sum of the covariance matrices ($\mathbf{R}_{s,j}$) for each signal

$$\begin{aligned}\mathbf{R} &= \sum_{j=1}^{N_s}\mathbf{R}_{s,j} + \mathbf{R}_n = \mathbf{R}_\Sigma + \mathbf{R}_n \\ &= \mathbf{A}(\mathbf{V}_s)\mathbf{S}\mathbf{A}^H(\mathbf{V}_s) + \mathbf{R}_n,\end{aligned} \tag{3}$$

because all the operators used are linear, where $\mathbf{A}(\mathbf{V}_s) = [\mathbf{a}(\mathbf{v}_{s,1}),\ldots,\mathbf{a}(\mathbf{v}_{s,N_s})]$, $\mathbf{V}_s = [\mathbf{v}_{s,1},\ldots,\mathbf{v}_{s,N_e}]$ and $\mathbf{S} = \text{diag}([\sigma^2_{s,1},\ldots,\sigma^2_{s,N_e}])$. A classical delay beamformer can be used to create a dirty image from the covariance matrix by calculating for every voxel [7, p. 88]

$$J(\mathbf{v}) = \frac{\mathbf{a}^H(\mathbf{v})\mathbf{R}\mathbf{a}(\mathbf{v})}{(N_e)^2}. \tag{4}$$

A peak in this image indicates the position of a source.

3 Proposed Source Localisation Algorithm

The proposed algorithm consists of three stages. The first is preprocessing, which attempts to remove instrumental noise signals and isolate individual RFI sources. This is followed by the intergrating-out-variables method which exploits the low side lobes and produces a good estimate. This is then used as the initial guess for a fast converging iterative method in the final step.

3.1 Stage 1: Preprocessing

The objective of the preprocessing step is to reduce the effect of the instrumental noise signals and isolate individual RFI sources. As the instrumental noise signals of the antennas are not identically distributed, the noise powers in $\mathbf{R}_n$ will differ. However, the assumption is made that the instrumental noise signals of the antennas are independent, therefore $\mathbf{R}_n$ is a diagonal matrix.

To remove the effect of $\mathbf{R}_n$ on $\mathbf{R}$ a statistical method such as factor analysis [8, p.211-232] can be used, which decomposes the $N_e \times N_e$ covariance matrix into $\mathbf{R} = \mathbf{Z}\mathbf{Z}^H + \mathbf{D}$, where $\mathbf{Z}$ is an $N_e \times Q$ matrix and $\mathbf{D}$ is a diagonal $N_e \times N_e$ matrix. If the method is applied successfully $\mathbf{D} \approx \mathbf{R}_n$ and therefore $\mathbf{Z}\mathbf{Z}^H \approx \mathbf{R}_\Sigma$ (see equation (3)). If the columns of $\mathbf{A}(\mathbf{V}_s)$ are linearly independent and $N_s < N_e$, then $Q = N_s$. For the method to converge an upper limit on the number of factors Q, namely $Q < (N_e - \sqrt{N_e})$, is imposed [5].

The columns of $\mathbf{Z}$ are now used to construct new covariance matrices $\mathbf{R}_{f,j} = \mathbf{Z}(:,j)\mathbf{Z}^H(:,j)$. Consequently, the sources are divided between these covariance matrices and in the ideal case, where the columns of $\mathbf{A}(\mathbf{V}_s)$ are orthogonal, each $\mathbf{R}_{f,j}$ will match with an $\mathbf{R}_{s,j}$. In most radio astronomy data sets a single snapshot covariance matrix is affected by one or two RFI sources and even though the columns of $\mathbf{A}(\mathbf{V}_s)$ may not be orthogonal the separation is sufficient that each $\mathbf{R}_{f,j}$ will contain the majority of one source's power. LOFAR data indicates that unwanted direction and direction independent effects have the greatest effect on the amplitude of the elements of $\mathbf{R}_{f,j}$. This effect can be removed by considering only the phase information, $e^{i\angle\mathbf{R}_{f,j}}$.

3.2 Stage 2: Integrating-out-variables

Let the matrix $\mathbf{W} = e^{i\angle\mathbf{R}_{f,j}}$, where $e^{i\angle\mathbf{R}_{f,j}}$ is a result from the preprocessing step. Since $\mathbf{W}$ is Hermitian with no amplitude information, all the information is contained in the top (or bottom) triangular part of $\mathbf{W}$. There is a total of $N_b = (N_e^2 - N_e)/2$ elements in both the triangular parts which is equal to the number of antenna combinations (also called baselines). By stacking the transposed rows of the top triangular part of $\mathbf{W}$, an $N_b \times 1$ vector $\boldsymbol{\beta}$ is created. The classical delay beamformer spectrum can then be rewritten as a sum (omitting the dependency on $\mathbf{v}$)

$$J = \text{Tr}(\mathbf{R}) + 2\sum_{p=1}^{N_b}\left[\Re(\boldsymbol{\beta}_p)\cos(\boldsymbol{\zeta}_p) + \Im(\boldsymbol{\beta}_p)\sin(\boldsymbol{\zeta}_p)\right], \tag{5}$$

where vector $\boldsymbol{\zeta}$ contains the stacked (similar to $\boldsymbol{\beta}$) angle differences $\gamma_j - \gamma_k$ and $\gamma_j = \frac{2\pi\nu}{c}||\mathbf{v} - \mathbf{v}_j||$, where $\mathbf{v}_j$ is the position of the j^{th} antenna. The traditional method to find the location of the source requires that a beamformer must be constructed for every voxel in the near-field (where the number of voxels is dependent on the resolution as well as the size of the near-field). This problem therefore has computational complexity $\mathcal{O}(N_r \times N_\theta \times N_\phi)$.

To reduce the computational complexity of finding a source location from cubic to linear, the proposed method integrates out variables and then only varies one variable to find

the peak. The trigonometric functions in equation (5) can not be analytically integrated, therefore the integration is done numerically once a priori and is stored (the trade off is therefore that the storage requirement increases). The algorithm notation is: N_ϕ is the number of ϕ values in vector $\boldsymbol{\phi}$, N_θ is the number of θ values in vector $\boldsymbol{\theta}$, N_r is the number of r values in vector $\mathbf{r}$ and r_{nf} is the radius of the near-field. Two weighting matrices are calculated a priori:

- $\mathbf{W}_1$ with dimension $2 \times N_b \times N_\phi$: for $\cos(\boldsymbol{\zeta})$ and $\sin(\boldsymbol{\zeta})$, vary $\phi \in [-\pi, \pi]$ and integrate out $\theta \in [0, \pi/2]$[1] and $r \in [0, r_{nf}]$.
- $\mathbf{W}_2$ with dimension $2 \times N_b \times N_\phi \times N_\theta$: for $\cos(\boldsymbol{\zeta})$ and $\sin(\boldsymbol{\zeta})$, vary $\phi \in [-\pi, \pi]$ and vary $\theta \in [0, \pi/2]$[1] and integrate out $r \in [0, r_{nf}]$.

The weighting matrices $\mathbf{W}_1$ and $\mathbf{W}_2$ are calculated only once for a given array and frequency. The steps of the algorithm are:

- Calculate

$$f_1(\boldsymbol{\phi}(k)) = \sum_{p=1}^{N_b} \left[\Re(\boldsymbol{\beta}_p)\mathbf{W}_1(1,p,k) + \Im(\boldsymbol{\beta}_p)\mathbf{W}_1(2,p,k)\right], \tag{6}$$

  for $k = 1, \ldots, N_\phi$. Find the peak of f_1 and the corresponding index i_ϕ of $\boldsymbol{\phi}$.
- Use index i_ϕ to fix ϕ and find the peak of

$$f_2(\boldsymbol{\theta}(k)) = \sum_{p=1}^{N_b} \Big[\Re(\boldsymbol{\beta}_p)\mathbf{W}_2(1,p,i_\phi,k) + \Im(\boldsymbol{\beta}_p)\mathbf{W}_2(2,p,i_\phi,k)\Big], \tag{7}$$

  for $k = 1, \ldots, N_\theta$. Find the peak of f_2 and the corresponding index i_θ of $\boldsymbol{\theta}$.
- Use i_ϕ and i_θ to fix ϕ and θ, respectively, and use one dimensional classical delay beamforming imaging to obtain a value for r. If the recovered value is not close to 1, return to the first step and choose the next highest peak (and repeat this N_i times until the threshold is met or there are no more peaks).

The position obtained is just an estimate and the accuracy is dependent on how low the side lobe levels are. This method only needs to search an $(N_r + N_\theta + N_\phi)$ array N_i times, while 3D MUSIC must search a 3 dimensional grid $(N_r \times N_\theta \times N_\phi)$. In the simulation results it is shown that N_i is almost always equal to 1.

3.3 Stage 3: Minimum Error Convergence

The proposed convergence algorithm uses the same concepts as those found in [9] which are used for antenna position calibration. The core idea is that $\mathbf{a}(\mathbf{v})\mathbf{a}^H(\mathbf{v})$ can be linearised if the error of the estimate of $\mathbf{v}_s$ is sufficiently small. If it is assumed that the effect of $\mathbf{G}(\mathbf{V}_s)$ can be discounted and only one source is present then

$$\angle \mathbf{W}_{jk} = \frac{2\pi\nu}{c}(||\mathbf{v}_s - \mathbf{v}_j|| - ||\mathbf{v}_s - \mathbf{v}_k||) + 2\pi m_{jk}, \tag{8}$$

where m_{jk} is an integer that represents the phase ambiguity. Let $\boldsymbol{\delta}_i = \mathbf{v}_s^o - \mathbf{v}_j$, where $\mathbf{v}_s^o$ is an estimate of the RFI position and let the error $\boldsymbol{\varepsilon} = \mathbf{v}_s^o - \mathbf{v}_s$ (assumed small). Then the Taylor expansion yields

$$\begin{aligned} ||\mathbf{v}_s - \mathbf{v}_j|| = ||\boldsymbol{\delta}_j - \boldsymbol{\varepsilon}|| &= \sqrt{||\boldsymbol{\delta}_j||^2 + ||\boldsymbol{\varepsilon}||^2 - 2\boldsymbol{\delta}_j \cdot \boldsymbol{\varepsilon}} \\ &\approx ||\boldsymbol{\delta}_j|| - \frac{\boldsymbol{\delta}_j \cdot \boldsymbol{\varepsilon}}{||\boldsymbol{\delta}_j||}. \end{aligned} \tag{9}$$

Using the approximation in equation (9), define

$$\begin{aligned} \mathbf{B}_{jk} &= \left(\frac{-\boldsymbol{\delta}_j}{||\boldsymbol{\delta}_j||} + \frac{\boldsymbol{\delta}_k}{||\boldsymbol{\delta}_k||}\right) \cdot \boldsymbol{\varepsilon} \\ &\approx \angle\left[\mathbf{W}_{jk} e^{\frac{-i2\pi\nu}{c}(||\boldsymbol{\delta}_j|| - ||\boldsymbol{\delta}_k||)}\right] \frac{c}{2\pi\nu}, \end{aligned} \tag{10}$$

which only holds if $\boldsymbol{\varepsilon}$ is sufficiently small so that the phase ambiguity m_{jk} is zero. By stacking the transposed rows of the top triangular part of $\mathbf{B}$, an $N_b \times 1$ vector can be created

$$\mathbf{b} = \mathbf{M}\boldsymbol{\varepsilon}, \tag{11}$$

where $\mathbf{M}$ is an $N_b \times 3$ matrix consisting of the stacked $\left(\frac{-\boldsymbol{\delta}_j}{||\boldsymbol{\delta}_j||} + \frac{\boldsymbol{\delta}_k}{||\boldsymbol{\delta}_k||}\right)$ vectors. Equation (11) is then used to define the least squares (LS) problem $\widehat{\boldsymbol{\varepsilon}} = \underset{\boldsymbol{\varepsilon}}{\operatorname{argmin}} ||\mathbf{b} - \mathbf{M}\boldsymbol{\varepsilon}||^2$. The optimal solution in an LS sense is then

$$\widehat{\boldsymbol{\varepsilon}} = (\mathbf{M}^H\mathbf{M})^{-1}\mathbf{M}^H\mathbf{b}. \tag{12}$$

When equation (12) is used to calculate $\hat{\boldsymbol{\varepsilon}}$ iteratively and the estimate $\mathbf{v}_s^o := \mathbf{v}_s^o - \widehat{\boldsymbol{\varepsilon}}$ is updated, the estimate $\mathbf{v}_s^o$ will converge to $\mathbf{v}_s$ if the initial estimate for $\mathbf{v}_s$ is within the main lobe of the beamformer.

4 Simulation in the Near-field

To evaluate the proposed algorithm, a simulation was done using the layout of the 48 coplanar antennas from the LOFAR CS302 station Low Band Antenna (LBA) subsystem (see figure 1). A uniform distribution was used to generate 5000 random source positions which lie outside the aforementioned array, but within the array near-field. From the positions, covariance matrices were generated and the algorithm was applied to each one. For only 2.1 % of the covariance matrices did the integrating-out-variables method have to iterate more than once.

For 95 % of the runs, the algorithm took less than 1.5 s (the median of all runs was 1.16 s and the maximum 9 s). This gives a speed-up in the order of 8000 compared to the 3D MUSIC method when both methods were run on the same hardware, had the same resolution and were not parallelised.

[1] Only one hemisphere needs to be considered for an Earth based array.

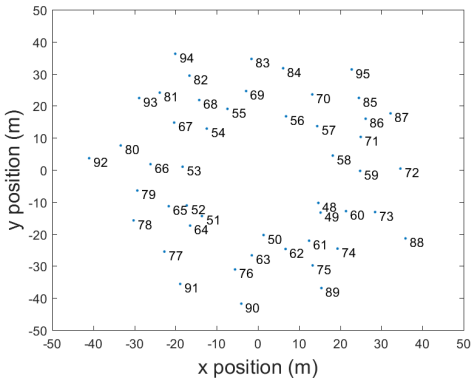

Figure 1. Array layout of the LOFAR CS302 Low Band Antenna subsystem.

To measure the accuracy of the algorithm, the euclidean distance (now called the distance error) between the position of each source and its corresponding estimated position was calculated. The integrating-out-variables stage yielded a median distance error of 2.19 *m* with a median average deviation of 1.19 *m* (see figure 2). After the convergence stage, the median as well as spread of the distance errors are drastically reduced to effectively 0. Only 1.24% of the distance errors are non-zero, however all are smaller than 3.2 *m*. These outliers all lie within 0.06 *rad* of the horizon, lie further than 170 *m* from the array centre and the error appears in the z direction (the direction orthogonal to the plane that the array lies in). This occurs because the array is planar and therefore has less resolution in the z direction for sources further away from the array and closer to the horizon (a similar loss in accuracy also occurs when using the 3D MUSIC algorithm).

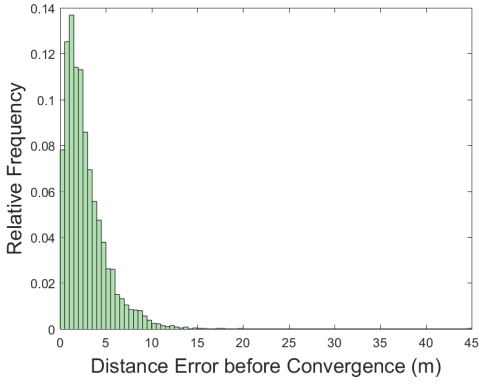

Figure 2. Relative frequency histogram of the distance error before the convergence stage for 5000 runs.

5 Conclusion

A new near-field localisation algorithm for interferometric arrays with low array beam side lobes is proposed. The algorithm is validated using simulations and has a similar accuracy to the 3D MUSIC algorithm. The advantage of the proposed algorithm is that the computational complexity is reduced from $\mathcal{O}(N_r \times N_\theta \times N_\phi)$ to $\mathcal{O}(N_r + N_\theta + N_\phi)$. The drawback is that the algorithm introduces weighting matrices that have to be calculated once a priori and stored. The algorithm has the same accuracy as 3D MUSIC. These results strongly indicate the accuracy and precision of the proposed algorithm to locate RFI sources.

6 Acknowledgements

This work is funded and supported by IBM, ASTRON, the Dutch Ministry of Economic Affairs and the Province of Drenthe, SKA-SA, the SA Research Chairs Initiative of the DST, the NRF, and a Marie Curie IRSES Fellowship within the 7th EC Framework Programme MIDPREP.

References

[1] M. P. van Haarlem et al., "LOFAR: The Low Frequency Array," *Astronomy & Astrophysics*, **556**, A2, August 2013, pp. 1–53, doi:10.1051/0004-6361/201220873.

[2] P. E. Dewdney, P. J. Hall, R. T. Schilizzi, and T. J. L. W. Lazio, "The Square Kilometre Array," *Proceedings of the IEEE*, **97**, 8, August 2009, pp. 1483-1496, doi:10.1109/JPROC.2009.2021005.

[3] D. Starer and A. Nehorai, "Passive Localization of Near-Field Sources by Path Following," *IEEE Transactions on Signal Processing*, **42**, 3, March 1994, pp. 677–680, doi:10.1109/78.277864.

[4] A. J. Weiss and B. Friedlander, "Range and Bearing Estimation Using Polynomial Rooting," *IEEE Journal of Oceanic Engineering*, **18**, 2, April 1993, pp. 130–137, doi:10.1109/48.219532.

[5] A. van der Veen, A. Leshem and A. Boonstra, "Signal Processing for Radio Astronomical Arrays," *Processing Workshop Proceedings, Sensor Array and Multichannel Signal*, July 2004, pp. 1–10, doi:10.1109/SAM.2004.1502901.

[6] M. Zatman, "How narrow is narrowband?," *IEE Proceedings-Radar, Sonar and Navigation*, **145**, 2, April 1998, pp. 85–91, doi:10.1049/ip-rsn:19981670.

[7] C. A. Balanis and P. I. Ioannides, *Introduction to Smart Antennas*, Morgan & Claypool Publishers, 2007.

[8] H. H. Hatman, *Modern Factor Analysis*, University of Chicago Press, 1976.

[9] S. J. Wijnholds, G. Pupillo, P. Bolli and G. Virone, "UAV-Aided Calibration for Commissioning of Phased Array Radio Telescopes," *URSI AP-RASC*, August 2016, pp. 228–231, doi:10.1109/URSIAP-RASC.2016.7601375.

2.4 Journal Paper - Computationally Efficient Source Localization for Radio Interferometric Arrays

AGU PUBLICATIONS

Radio Science

RESEARCH ARTICLE
10.1002/2017RS006513

Key Points:
- We present a source localization algorithm for arbitrary arrays working in near field and far field
- The scaling of the algorithm is linear with search grid size instead of cubic as 3-D MUSIC
- The accuracy of the algorithm is validated using simulations and data from the LOFAR telescope

Correspondence to:
J.-W. Steeb,
jwsteeb@gmail.com

Citation:
Steeb, J.-W., Davidson, D. B., & Wijnholds, S. J. (2018). Computationally efficient radio frequency source localization for radio interferometric arrays. *Radio Science*, *53*, 242–256. https://doi.org/10.1002/2017RS006513

Received 7 DEC 2017
Accepted 2 FEB 2018
Accepted article online 8 FEB 2018
Published online 2 MAR 2018

Computationally Efficient Radio Frequency Source Localization for Radio Interferometric Arrays

J.-W. Steeb[1], David B. Davidson[1,2], and Stefan J. Wijnholds[1,3]

[1]Department of Electrical and Electronic Engineering, Stellenbosch University, Stellenbosch, South Africa, [2]Curtin Institute of Radio Astronomy, Curtin University, Bentley, Western Australia, Australia, [3]Netherlands Institute for Radio Astronomy (ASTRON), Dwingeloo, The Netherlands

Abstract Radio frequency interference (RFI) is an ever-increasing problem for remote sensing and radio astronomy, with radio telescope arrays especially vulnerable to RFI. Localizing the RFI source is the first step to dealing with the culprit system. In this paper, a new localization algorithm for interferometric arrays with low array beam sidelobes is presented. The algorithm has been adapted to work both in the near field and far field (only the direction of arrival can be recovered when the source is in the far field). In the near field the computational complexity of the algorithm is linear with search grid size compared to cubic scaling of the state-of-the-art 3-D MUltiple SIgnal Classification (MUSIC) method. The new method is as accurate as 3-D MUSIC. The trade-off is that the proposed algorithm requires a once-off a priori calculation and storing of weighting matrices. The accuracy of the algorithm is validated using data generated by low-frequency array while a hexacopter was flying around it and broadcasting a continuous-wave signal. For the flight, the mean distance between the differential GPS positions and the corresponding estimated positions of the hexacopter is 2 m at a wavelength of 6.7 m.

1. Introduction

Radio frequency interference (RFI) is an important issue in many areas of scientific research, for example, in remote sensing and radio astronomy. The ideal solution is to identify the location of the RFI and then remove it. Localization can be done using either the scientific instrument detecting the RFI or additional equipment. This paper will focus on using radio astronomy interferometric arrays to localize RFI signals. If the RFI source cannot be removed, spatial RFI mitigation methods such as found in Sardarabadi et al. (2015) and van der Tol and van der Veen (2005) can be implemented.

An RFI signal can be in either the near field or far field of a sensor array. For sources in the far field only the direction of arrival information can be recovered. Current source localization algorithms either make use of brute force methods (such as MUSIC; Balanis & Ioannides, 2007, p. 80–82) where the entire solution space is searched) or exploit the array layout (a common layout is a uniform linear array). Methods that exploit a uniform linear array layout include path following (Starer & Nehorai, 1994), polynomial rooting (Weiss & Friedlander, 1993), weighted linear prediction (Grosicki et al., 2005), and estimation of signal parameters using rotational invariance techniques (Challa & Shamsunder, 1995; Yuen & Friedlander, 1998). In Huang and Barkat (1991) and Hung et al. (1996), an improvement of the MUSIC algorithm is proposed, which replaces searching a dimension with solving the roots of a polynomial. This polynomial arises from calculating a Fourier series which estimates the geometric delay function, but this method introduces an estimation error.

For radio astronomy arrays, brute force methods are computationally expensive due to the high resolution caused by long baselines. Furthermore, to obtain as much information as possible for imaging (optimizing the spatial sampling) the array layouts are nonuniform and nonlinear. However, radio astronomy interferometric arrays have the advantage that the array beam has low sidelobe levels. Therefore, a novel computationally efficient source localization algorithm is presented which is designed for irregular interferometric arrays and takes advantage of low array beam sidelobes.

To evaluate the proposed localization algorithm, 48 of the outer antennas in the low-band antenna (LBA) station CS302 of the low-frequency array (LOFAR) (van Haarlem et al., 2013) were used. A satellite image of CS302 is given in Figure 1 as well as a plot of the LBAs used.

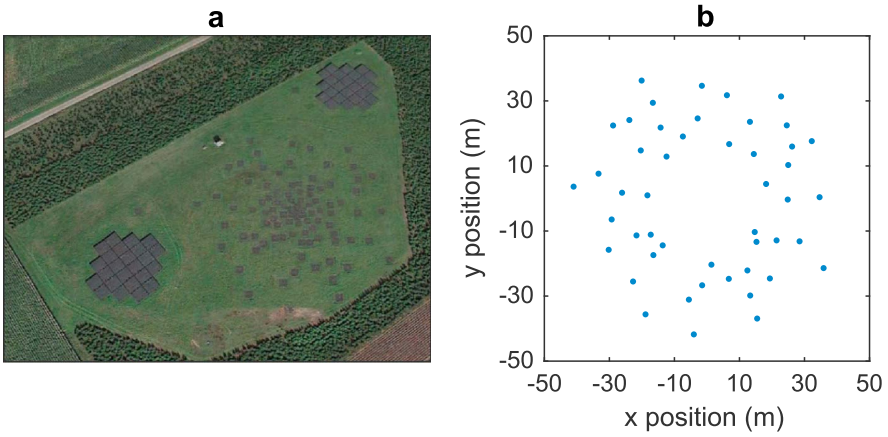

Figure 1. (a) Satellite image of low-frequency array station CS302 with a low-band antenna array in the middle and two high-band antenna arrays flanking it. (b) Array layout of the LOFAR CS302 low-band antenna subsystem.

2. Data Model

We consider the scenario where an array is observing astronomical sources and the measurements are contaminated by a single RFI source. This is later generalized to multiple RFI sources. The assumption is made that the power of the RFI source is considerably higher than the power of the astronomical sources. Therefore, the astronomical sources are omitted from the model. RFI signals are also affected by direction dependent effects such as path loss, polarization mismatch factor, the gain of the antennas, and atmospheric effects. Furthermore, direction-independent effects include the receiver electronics, in particular the low noise amplifiers. These effects are usually removed by calibration; however, accurate calibration is not possible in the presence of strong RFI. For the jth antenna these effects are contained in the complex gain $g_j(\mathbf{v}_s)$ which is a function of the position vector of the RFI source $\mathbf{v}_s = \left[x_s, y_s, z_s\right]^T$.

To keep the model simple, the output of the array will only be considered for a single-frequency channel and polarization. The single-frequency assumption is reasonable as radio telescopes are usually designed in such a way that their individual frequency channels satisfy the narrowband assumption. Wideband signals, such as Digital audio broadcasting, will simply be split over multiple channels, for each of which the signal can be treated as a single-frequency signal. If the array consists of N_e elements, then at time t the voltage output can be expressed as (van der Tol & van der Veen, 2005; van der Veen et al., 2004)

$$\mathbf{y}(t) = \mathbf{x}_s(t) + \mathbf{x}_n(t), \tag{1}$$

where $\mathbf{y}(t) = \left[y_1(t), \ldots, y_{N_e}(t)\right]^T$ is the vector of measured array output signals, $\mathbf{x}_n(t) = \left[n_1(t), \ldots, n_{N_e}(t)\right]^T$ is the vector of instrumental noise for each antenna, and $\mathbf{x}_s(t)$ is the vector describing the RFI signal, which experiences a delay for each antenna. This term is described in detail below.

For the jth antenna, τ_j is the delay between the source location and the array element. If the delayed signal $s(t-\tau_j)$ is to be used in the formulation of a covariance matrix model (see equation (6)), it can be approximated by $s(t-\tau_j) \approx s(t)e^{-i2\pi\nu\tau_j}$, where ν is the center frequency of the channel. This can be done, since only the delay differences between antennas $\tau_{jk} = \tau_j - \tau_k$ are of importance in the covariance matrix model (see equation (6)) in conjunction with equation (2). This approximation is possible if the signal is sufficiently narrowband, that is, $2\pi\Delta\nu\tau_{max} \ll 1$ (Zatman, 1998), where $\Delta\nu$ is the signal's bandwidth and $\tau_{max} = \tau_j - \tau_k$ such that the jth and kth antenna have the longest baseline (distance between antennas) and a straight line can be traced through the source and the two antennas. The phase delays of the source can be stacked into a vector that is called the geometric delay vector

$$\mathbf{a}(\mathbf{v}_s) = \begin{bmatrix} e^{-i2\pi\nu\tau_1} \\ \vdots \\ e^{-i2\pi\nu\tau_{N_e}} \end{bmatrix}. \tag{2}$$

When the RFI source is in the near field, the jth delay is given by $\tau_j = ||\mathbf{v}_s - \mathbf{v}_j||/c$, where $\mathbf{v}_j = \left[x_j, y_j, z_j\right]$ is the position vector of the antenna. For the far-field case, the jth delay is given by $\tau_j = -\left(\mathbf{v}_{s,ff}^T \mathbf{v}_j\right)/c$, where

$\mathbf{v}_{s,ff}^T = \left[\sin(\theta_s)\cos(\phi_s), \sin(\theta_s)\sin(\phi_s), \cos(\theta_s)\right]^T$ is a direction vector. The angles θ_s and ϕ_s are respectively the polar and azimuthal angles of the RFI source. The model in equation (1) can be rewritten, using $\mathbf{a}(\mathbf{v}_s)$ and $\mathbf{g}(\mathbf{v}_s)$, as

$$\mathbf{y}(t) = \mathbf{a}(\mathbf{v}_s) \odot \mathbf{g}(\mathbf{v}_s)s(t) + \mathbf{x}_n(t), \tag{3}$$

where $\mathbf{g}(\mathbf{v}_s) = \left[g_1(\mathbf{v}_s), \ldots, g_{N_e}(\mathbf{v}_s)\right]^T$ is a vector that contains the complex gain for each antenna. To create images, radio interferometric arrays use the covariance matrix of the signals

$$\mathbf{R} = \mathbb{E}\{\mathbf{y}(t)\mathbf{y}^H(t)\}. \tag{4}$$

This matrix can only be estimated by assuming that all signals are stationary for short time periods, that is,

$$\hat{\mathbf{R}} = \frac{1}{N_t}\sum_{l=1}^{N_t} \mathbf{y}(lT_s)\mathbf{y}^H(lT_s), \tag{5}$$

where $\hat{\mathbf{R}}$ is the estimated covariance matrix, N_t is the number of samples for which the signals are stationary, and T_s is the sample time.

The covariance matrix and its estimate are Hermitian (complex symmetric) where the *kj*th element of the matrix is the correlation of the *k*th and *j*th antenna and the *kj*th element and *jk*th element are complex conjugates of each other.

Independence is assumed between the RFI source and the noise. Therefore, when substituting equation (3) into equation (4), the expectation of any nonself multiplication term is zero and consequently the substitution yields

$$\begin{aligned}\mathbf{R} &= \mathbf{R}_s + \mathbf{R}_n \\ &= (\mathbf{a}(\mathbf{v}_s) \odot \mathbf{g}(\mathbf{v}_s))\sigma_s^2(\mathbf{g}(\mathbf{v}_s) \odot \mathbf{a}(\mathbf{v}_s))^H + \mathbf{R}_n,\end{aligned} \tag{6}$$

where $\sigma_s^2 = \mathbb{E}\{s(t)s^*(t)\}$ is the power of the RFI signal, since the signal has zero mean. If N_s RFI signals are present, the covariance matrix is the sum of the covariance matrices ($\mathbf{R}_{s,j}$) for each signal

$$\begin{aligned}\mathbf{R} &= \sum_{j=1}^{N_s} \mathbf{R}_{s,j} + \mathbf{R}_n \\ &= \mathbf{R}_\Sigma + \mathbf{R}_n \\ &= (\mathbf{A}(\mathbf{V}_s) \odot \mathbf{G}(\mathbf{V}_s))\mathbf{S}(\mathbf{G}(\mathbf{V}_s) \odot \mathbf{A}(\mathbf{V}_s))^H + \mathbf{R}_n,\end{aligned} \tag{7}$$

because all the operators used are linear, where $\mathbf{A}(\mathbf{V}_s) = \left[\mathbf{a}\left(\mathbf{v}_{s,1}\right), \ldots, \mathbf{a}\left(\mathbf{v}_{s,N_s}\right)\right]$, $\mathbf{G}(\mathbf{V}_s) = \left[\mathbf{g}\left(\mathbf{v}_{s,1}\right), \ldots, \mathbf{g}\left(\mathbf{v}_{s,N_s}\right)\right]$, $\mathbf{V}_s = \left[\mathbf{v}_{s,1}, \ldots, \mathbf{v}_{s,N_s}\right]$ and $\mathbf{S} = \mathrm{diag}\left(\left[\sigma_{s,1}^2, \ldots, \sigma_{s,N_s}^2\right]\right)$.

A classical delay beamformer (CDB) $\mathbf{b}_{CDB}(\mathbf{v}) = (\mathbf{a}^H(\mathbf{v})\mathbf{a}(\mathbf{v}))^{-1}\mathbf{a}^H(\mathbf{v})$ can be used to create a dirty image (Thompson et al., 2004, p. 427–430) from the covariance matrix by calculating for every voxel (Balanis & Ioannides, 2007, p. 78)

$$\begin{aligned}J(\mathbf{v}) &= \mathbb{E}\left\{\mathbf{b}_{CDB}(\mathbf{v})\mathbf{y}(t)(\mathbf{b}_{CDB}(\mathbf{v})\mathbf{y}(t))^H\right\} \\ &= \mathbf{b}_{CDB}(\mathbf{v})\mathbf{R}\mathbf{b}_{CDB}^H(\mathbf{v}) \\ &= \frac{1}{N_e^2}\mathbf{a}^H(\mathbf{v})\mathbf{R}\mathbf{a}(\mathbf{v}).\end{aligned} \tag{8}$$

A peak in this image indicates the position of a source.

3. Proposed Source Localization Algorithm

Before the localization algorithm is applied, the RFI must be detected, for which methods described in (van der Tol & van der Veen, 2005) and van der Veen et al. (2004) can be used. The proposed localization algorithm consists of three stages. The first is preprocessing, which attempts to remove instrumental noise signals and isolate individual RFI sources. This is followed by the integrating-out-variables method which exploits the low sidelobes and which produces a reasonable estimate. This estimate is then used as the initial guess for a fast converging iterative method in the final step.

3.1. Stage 1: Preprocessing

The objective of the preprocessing step is to reduce the effect of the instrumental noise signals and isolate individual RFI sources. It is assumed that the power of the RFI signals is above the noise. As the instrumental noise signal may be different for different antennas, the noise powers in $\mathbf{R}_n$ will differ. However, the assumption is made that the instrumental noise signals of the antennas are independent; therefore, $\mathbf{R}_n$ is a diagonal matrix.

To remove the effect of $\mathbf{R}_n$ on $\mathbf{R}$, a statistical method such as complex factor analysis (Sardarabadi, 2016, p. 31–60) can be used, which decomposes the $N_e \times N_e$ covariance matrix into $\mathbf{R} = \mathbf{Z}\mathbf{Z}^H + \mathbf{D}$, where $\mathbf{Z}$ is an $N_e \times N_f$ matrix and $\mathbf{D}$ is a diagonal $N_e \times N_e$ matrix. If the method is applied successfully, $\mathbf{D} \approx \mathbf{R}_n$, and therefore $\mathbf{Z}\mathbf{Z}^H \approx \mathbf{R}_\Sigma$ (see equation (7)). If the columns of $\mathbf{A}(\mathbf{V}_s) \odot \mathbf{G}(\mathbf{V}_s)$ are linearly independent and $N_s < N_e$, then $N_f = N_s$. For the method to converge, an upper limit on the number of factors N_f, namely, $N_f < \left(N_e - \sqrt{N_e}\right)$, is imposed (van der Veen et al., 2004). The columns of $\mathbf{Z}$ are now used to construct a set of new covariance matrices

$$\begin{aligned} \mathbf{R}_{f,1} &= \mathbf{Z}(:,1)\mathbf{Z}^H(:,1), \\ &\vdots \\ \mathbf{R}_{f,N_s} &= \mathbf{Z}(:,N_s)\mathbf{Z}^H(:,N_s). \end{aligned}$$

Consequently, the sources are separated in these covariance matrices and in the ideal case, where the columns of $\mathbf{A}(\mathbf{V}_s) \odot \mathbf{G}(\mathbf{V}_s)$ are orthogonal, each $\mathbf{R}_{f,j}$ will match with an $\mathbf{R}_{s,j}$. In most radio astronomy data sets, a single snapshot covariance matrix is affected by only one or two RFI sources and, even though the columns of $\mathbf{A}(\mathbf{V}_s) \odot \mathbf{G}(\mathbf{V}_s)$ may not be orthogonal, the separation is sufficient for each $\mathbf{R}_{f,j}$ to contain the majority of one source's power.

The largest gain differences between the near-field signal received by multiple elements are caused by path loss differences which only affect the amplitudes of the gains. This effect can be removed by considering only the phase information.

3.2. Stage 2: Integrating Out Variables

Let the matrix $\mathbf{U} = e^{j\angle \mathbf{R}_{f,j}}$, where $e^{j\angle \mathbf{R}_{f,j}}$ is a result from the preprocessing step. Since $\mathbf{U}$ is Hermitian with no amplitude information, all the information is contained in the top (or bottom) triangular part of $\mathbf{U}$. There is a total of $N_b = (N_e^2 - N_e)/2$ elements in both the triangular parts, which is equal to the number of antenna combinations (also called baselines). By stacking the transposed rows of the top triangular part of $\mathbf{U}$, an $N_b \times 1$ vector $\boldsymbol{\beta}$ is created. If the top triangular part of $\mathbf{U}$ is used, then the relationship between the pth element of $\boldsymbol{\beta}$ and the jkth element of $\mathbf{U}$ is $p = (j-1)N_e - 0.5(j^2 + j) + k$, where $j \in \{1, \ldots, N_e - 1\}$ and $k \in \{j+1, \ldots, N_e\}$.

The classical delay beamformer spectrum (see equation (8)) for $\mathbf{U}$ can then be rewritten as a sum (the dependency on $\mathbf{v}_s$ will be omitted to make the notation more concise)

$$J = \frac{1}{N_e} + \frac{2}{N_e^2} \sum_{p=1}^{N_b} \Re\left[\beta_p e^{-i\zeta_p}\right], \tag{9}$$

where vector $\boldsymbol{\zeta}$ contains the stacked (similar to $\boldsymbol{\beta}$) angle differences $\gamma_j - \gamma_k$ and

$$\begin{aligned} \gamma_j &= \frac{-2\pi\nu}{c} ||\mathbf{v} - \mathbf{v}_j|| \\ &= \frac{-2\pi\nu}{c} \sqrt{r^2 - 2r(\sin(\theta)\cos(\phi)x_j + \sin(\theta)\sin(\phi)y_j + \cos(\theta)z_j) + r_j^2}. \end{aligned} \tag{10}$$

The coordinates of the voxel have been written in spherical coordinates (r, θ, ϕ) and (x_j, y_j, z_j) is the position of the jth antenna. The traditional method to find the location of the source requires that a beamformer must be constructed for every voxel in the near field, where the number of voxels is dependent on the resolution as well as the size of the near field. This problem therefore has computational complexity $\mathcal{O}(N_r \times N_\theta \times N_\phi)$, where N_r, N_θ, N_ϕ are, respectively, the number of r, θ, and ϕ values.

To reduce the computational complexity of finding a source location from cubic to linear, the proposed method integrates out variables and then only varies one variable to find the peak. The complex exponential function in equation (9) cannot be analytically integrated. Therefore, the integration is done numerically once a priori and is stored (the trade-off is therefore that the storage requirement increases). The algorithm notation is $\boldsymbol{\phi}$ is an $N_\phi \times 1$ vector of ϕ values, $\boldsymbol{\theta}$ is an $N_\theta \times 1$ vector of θ values, $\mathbf{r}$ is an $N_r \times 1$ vector of r values, r_a is the minimum radius wherein all the array elements lie and $r_{nf} = b_{max}^2 \nu_0 / c$ is the radius at which the transition

from radiating near field to far field starts (Thompson et al., 2004, p. 601), and b_{max} is the length of the longest baseline. Two weighting matrices are calculated a priori:

1. First weighting matrix

$$\mathbf{W}_1(p,n) = \int_0^{\pi/2} \int_{r_a}^{r_{nf}} e^{-i\zeta_p(\phi_n)} \mathrm{d}r\mathrm{d}\theta, \tag{11}$$

   with dimension $N_b \times N_\phi$ and $\phi_n \in [-\pi, \pi]$. The θ integral is over 0 to $\pi/2$, because only one hemisphere needs to be considered for an Earth-based array.
2. Second weighting matrix:

$$\mathbf{W}_2(p,m,n) = \int_{r_a}^{r_{nf}} e^{-i\zeta_p(\theta_m,\phi_n)} \mathrm{d}r, \tag{12}$$

   with dimension $N_b \times N_\theta \times N_\phi$, $\phi_n \in [-\pi, \pi]$ and $\theta_m \in [0, \pi/2]$.

The weighting matrices $\mathbf{W}_1$ and $\mathbf{W}_2$ are calculated only once for a given array and frequency. The steps of the algorithm are as follows:

1. Calculate

$$f_1(\boldsymbol{\phi}(n)) = \sum_{p=1}^{N_b} \Re\left[\beta_p \mathbf{W}_1(p,n)\right], \tag{13}$$

   for $n = 1, \ldots, N_\phi$. Find the peak of f_1 and the corresponding index n_ϕ of $\boldsymbol{\phi}$.
2. Use index n_ϕ to fix ϕ and find the peak of

$$f_2(\theta(m)) = \sum_{p=1}^{N_b} \Re\left[\beta_p \mathbf{W}_2(p,m,n_\phi)\right], \tag{14}$$

   for $m = 1, \ldots, N_\theta$. Find the peak of f_2 and the corresponding index m_θ of $\boldsymbol{\theta}$.
3. Use n_ϕ and m_θ to fix ϕ and θ, respectively, and use normalized one-dimensional classical delay beamforming imaging (see equation (8)) to obtain a value for r. If the recovered value is not close to 1, return to the first step and choose the next highest peak (and repeat this N_i times until the threshold is met or there are no more peaks).

The position obtained is just an estimate, and the accuracy is dependent on how low the sidelobe levels are. This method only needs to search an $(N_r + N_\theta + N_\phi)$ array N_i times, while 3-D MUSIC must search a three-dimensional grid $(N_r \times N_\theta \times N_\phi)$. In our simulations, we found that N_i is almost always equal to 1.

3.2.1. Stage 2: Storage Requirement Reduction

For each iteration of stage 2 of the algorithm, all values in matrix $\mathbf{W}_1$ are used; however, only an N_ϕ^{th} part of $\mathbf{W}_2$ is used, since n_ϕ is fixed. The memory requirement can be reduced by calculating the required weights on the fly. For the jk baseline and fixed values for θ and ϕ the required integral is

$$\mathbf{W}_2(p,m,n_\phi) = \int_{r_a}^{r_{nf}} e^{-i[\gamma_j(r)-\gamma_k(r)]} \mathrm{d}r. \tag{15}$$

This integral cannot be analytically solved, and solving it numerically is computationally expensive. Defining $d_j = -2(\sin(\theta)\cos(\phi)x_j + \sin(\theta)\sin(\phi)y_j + \cos(\theta)z_j)$ and applying the Taylor expansion to equation (10) yields

$$\begin{aligned}\gamma_j &= \frac{-2\pi\nu}{c}\sqrt{r^2 + d_j r + r_j^2} \\ &= \frac{-2\pi\nu}{c} r\sqrt{1 + \frac{d_j r + r_j^2}{r^2}} \\ &\approx \frac{-2\pi\nu}{c}\left[r + \frac{d_j}{2} + \frac{4r_j^2 - d_j^2}{8r}\right],\end{aligned} \tag{16}$$

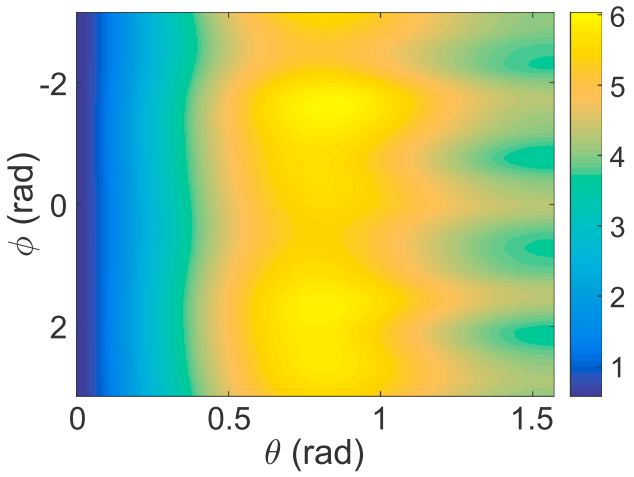

Figure 2. Plot of the mean absolute percentage error of $\widetilde{\mathbf{W}}_2$ as a function of θ and ϕ (see equation (19)). Low-frequency array station's CS302 layout was used at a frequency of 44.5 MHz.

with the assumption that $r^2 > d_j r + r_j^2$ (which is valid since the integral starts outside the array). The argument of the complex exponential is then approximated by

$$\begin{aligned}\gamma_j - \gamma_k &\approx \frac{-2\pi\nu}{c}\left[\frac{d_j - d_k}{2} + \frac{4(r_j^2 - r_k^2) - (d_j^2 - d_k^2)}{8r}\right] \\ &= a + \frac{b}{r},\end{aligned} \tag{17}$$

where

$$\begin{aligned}a &= -\pi\nu c^{-1}\left[d_j - d_k\right], \\ b &= -\frac{1}{4}\pi\nu c^{-1}\left[4\left(r_j^2 - r_k^2\right) - \left(d_j^2 - d_k^2\right)\right].\end{aligned}$$

Using the approximation in equation (17), the integral in equation (15) can be solved by using the exponential integral function

$$\begin{aligned}\mathbf{W}_2(p,n,m) \approx \widetilde{\mathbf{W}}_2(p,n,m) &= \int_{r_a}^{r_{nf}} e^{-i[a+b/r]}\mathrm{d}sr \\ &= e^{-ia}\left[ib\mathrm{E}_1\left(\frac{ib}{r_a}\right) - ib\mathrm{E}_1\left(\frac{ib}{r_{nf}}\right) - r_a e^{-ib/r_a} + r_{nf}e^{-ib/r_{nf}}\right],\end{aligned} \tag{18}$$

where $|\angle\frac{ib}{r_a}| = |\angle\frac{ib}{r_{nf}}| = \frac{\pi}{2}$, because both arguments are only complex. A comparison of the compute time of MATLAB's global adaptive quadrature method and equation (18) showed a 7 times speedup, at a frequency of 44.5 MHz using the LOFAR station's CS302 layout (a desktop computer with an Intel Core i5-2500k chip was used). To measure the accuracy of the approximation, the mean absolute percentage error is used

$$\mathbf{M}(n,m) = 100\sum_{p=1}^{N_b}\left|\frac{\mathbf{W}_2(p,n,m) - \widetilde{\mathbf{W}}_2(p,n,m)}{N_b\mathbf{W}_2(p,n,m)}\right|. \tag{19}$$

In Figure 2 a plot of $\mathbf{M}$ is given with a maximum mean absolute percentage error of 6% which occurs at approximately $\theta = \pi/4$.

3.2.2. Stage 2: Far-Field Approach

For the far-field case the classical delay beamformer (see equation (9)) is also used; however, it is a function of $\mathbf{v}_{s,ff}$ and equation (10) is now given by

$$\begin{aligned}\gamma_j &= \frac{2\pi\nu}{c}\mathbf{v}_{s,ff}^T\mathbf{v}_j \\ &= \frac{2\pi\nu}{c}\left(\sin(\theta)\cos(\phi)x_j + \sin(\theta)\sin(\phi)y_j + \cos(\theta)z_j\right).\end{aligned} \tag{20}$$

Since equation (20) is a function of (θ, ϕ), only θ has to be integrated out to generate a weighting matrix. The complex exponential that is integrated can be solved in terms of special functions if $\theta \in [0, 2\pi]$ (instead of $\theta \in [0, \pi/2]$) as follows

$$\begin{aligned}\mathbf{W}_{1,\mathrm{ff}}(p,n) &= \int_0^{2\pi} e^{-i\zeta_p(\phi_n)}\mathrm{d}\theta = \int_0^{2\pi} e^{-i[\gamma_j(\phi_n)-\gamma_k(\phi_n)]}\mathrm{d}\theta \\ &= \int_0^{2\pi} e^{-i[a\sin(\theta)+b\cos(\theta)]}\mathrm{d}\theta \\ &= 2\pi I_0\left(\sqrt{-a^2-b^2}\right),\end{aligned} \tag{21}$$

where

$$\begin{aligned}a &= i2\pi\nu c^{-1}\left(\cos(\phi_n)\left(x_j-x_k\right)+\sin(\phi_n)\left(y_j-y_k\right)\right), \\ b &= i2\pi\nu c^{-1}\left(z_j-z_k\right).\end{aligned}$$

Integrating over 2π will cause a mirror image when plotting $f_{1,\mathrm{ff}}(\boldsymbol{\phi}(k))$ as given by equation (23). Therefore, each peak will have to be investigated. In the special case that the array is planar, that is, $z_j = 0$, it is possible to do the integral over $\pi/2$

$$\begin{aligned}\mathbf{W}_{1,\mathrm{ff}}(p,n) &= \int_0^{\pi/2} e^{-ia\sin(\theta)}\mathrm{d}\theta \\ &= \frac{\pi}{2}\left[J_0(a)+iH_0(a)\right].\end{aligned} \tag{22}$$

The weighting matrix $\mathbf{W}_{1,\mathrm{ff}}$ is calculated only once for a given array and frequency. The steps of the algorithm are as follows:

1. Calculate

$$f_{1,\mathrm{ff}}(\boldsymbol{\phi}(n)) = \sum_{p=1}^{N_\mathrm{b}} \Re\left[\beta_p \mathbf{W}_{1,\mathrm{ff}}(p,n)\right], \tag{23}$$

   for $n = 1, \ldots, N_\phi$. Find the peak of $f_{1,\mathrm{ff}}$ and the corresponding index n_ϕ of $\boldsymbol{\phi}$.
2. Use n_ϕ to fix ϕ and use normalized one-dimensional near-field classical delay beamforming imaging (see equation (8)) to obtain a value for θ. If the recovered value is not close to 1, return to the first step and choose the next highest peak (and repeat this N_i times until the threshold is met or there are no more peaks).

This method only needs to search an $(N_\theta + N_\phi)$ array N_i times, while 2-D MUSIC must search a two-dimensional grid $(N_\theta \times N_\phi)$.

3.3. Stage 3: Minimum Error Convergence

The proposed convergence algorithm uses the same concepts as those found in Wijnholds et al. (2016), which are used for antenna position calibration. The core idea is that $\mathbf{a}(\mathbf{v})\mathbf{a}^H(\mathbf{v})$ can be linearized if the error of the estimate of $\mathbf{v}_\mathrm{s}$ is sufficiently small. If it is assumed that the effect of $\mathbf{G}(\mathbf{V}_\mathrm{s})$ can be discounted and only one source is present, then

$$\angle\mathbf{U}_{jk} = \frac{-2\pi\nu}{c}\left(||\mathbf{v}_\mathrm{s}-\mathbf{v}_j|| - ||\mathbf{v}_\mathrm{s}-\mathbf{v}_k||\right) + 2\pi m_{jk}, \tag{24}$$

where m_{jk} is an integer that represents the phase ambiguity. Let $\boldsymbol{\delta}_j = \mathbf{v}_\mathrm{s}^o - \mathbf{v}_j$, where $\mathbf{v}_\mathrm{s}^o$ is an estimate of the RFI position. Assume that the error $\boldsymbol{\epsilon} = \mathbf{v}_\mathrm{s}^o - \mathbf{v}_\mathrm{s}$ is small, then the Taylor expansion yields

$$\begin{aligned}||\mathbf{v}_\mathrm{s}-\mathbf{v}_j|| = ||\boldsymbol{\delta}_j-\boldsymbol{\epsilon}|| &= \sqrt{||\boldsymbol{\delta}_j||^2 + ||\boldsymbol{\epsilon}||^2 - 2\boldsymbol{\delta}_j^T\boldsymbol{\epsilon}} \\ &\approx \sqrt{||\boldsymbol{\delta}_j||^2 - 2\boldsymbol{\delta}_j^T\boldsymbol{\epsilon}} \\ &= ||\boldsymbol{\delta}_j||\sqrt{1-\frac{2\boldsymbol{\delta}_j^T\boldsymbol{\epsilon}}{||\boldsymbol{\delta}_j||^2}} \\ &\approx ||\boldsymbol{\delta}_j|| - \frac{\boldsymbol{\delta}_j^T\boldsymbol{\epsilon}}{||\boldsymbol{\delta}_j||}.\end{aligned} \tag{25}$$

Substituting equation (25) into equation (24) yields a linear equation in terms of $\boldsymbol{\epsilon}$

$$\angle \mathbf{U}_{jk} \approx \frac{-2\pi\nu}{c}\left[||\boldsymbol{\delta}_j|| - ||\boldsymbol{\delta}_k|| + \left(\frac{-\boldsymbol{\delta}_j}{||\boldsymbol{\delta}_j||} + \frac{\boldsymbol{\delta}_k}{||\boldsymbol{\delta}_k||}\right)^T \boldsymbol{\epsilon}\right] + 2\pi m_{jk}. \tag{26}$$

Using the approximation in equation (26), define

$$\mathbf{B}_{jk} = \left(\frac{-\boldsymbol{\delta}_j}{||\boldsymbol{\delta}_j||} + \frac{\boldsymbol{\delta}_k}{||\boldsymbol{\delta}_k||}\right)^T \boldsymbol{\epsilon} \approx \angle\left[\mathbf{U}_{jk} e^{\frac{i2\pi\nu}{c}(||\boldsymbol{\delta}_j|| - ||\boldsymbol{\delta}_k||)}\right]\frac{-c}{2\pi\nu}, \tag{27}$$

which only holds if $\boldsymbol{\epsilon}$ is sufficiently small so that the phase ambiguity m_{jk} is zero. By stacking the transposed rows of the top triangular part of $\mathbf{B}$, an $N_b \times 1$ vector can be created

$$\mathbf{b} = \mathbf{M}\boldsymbol{\epsilon}, \tag{28}$$

where $\mathbf{M}$ is an $N_b \times 3$ matrix consisting of the stacked $\left(\frac{-\boldsymbol{\delta}_j}{||\boldsymbol{\delta}_j||} + \frac{\boldsymbol{\delta}_k}{||\boldsymbol{\delta}_k||}\right)$ vectors. Equation (28) is used to define the least squares (LS) problem $\hat{\boldsymbol{\epsilon}} = \arg\min_{\boldsymbol{\epsilon}} ||\mathbf{b} - \mathbf{M}\boldsymbol{\epsilon}||^2$. The optimal solution in an LS sense is

$$\hat{\boldsymbol{\epsilon}} = (\mathbf{M}^H\mathbf{M})^{-1}\mathbf{M}^H\mathbf{b}. \tag{29}$$

When equation (29) is used to calculate $\hat{\boldsymbol{\epsilon}}$ iteratively and the estimate $\mathbf{v}_s^o := \mathbf{v}_s^o - \hat{\boldsymbol{\epsilon}}$ is updated, the estimate $\mathbf{v}_s^o$ converges to $\mathbf{v}_s$ if the initial estimate of $\mathbf{v}_s$ is within the main lobe of the beamformer.

3.3.1. Stage 3: *z* Direction Search Correction Step

The minimum convergence algorithm may not always converge correctly if the source lies close to the horizon for a planar array (due to the low resolution). Convergence can be improved by doing one-dimensional classical delay beamforming imaging (see equation (8)) in the z direction, after the first attempt of the minimum convergence algorithm. The new estimate of z is then used to complete a second run of the minimum convergence algorithm.

3.3.2. Stage 3: Far-Field Approach

When the source is in the far field, a Taylor expansion is not necessary (see equation (25)), because the model for the phase is already linear

$$\begin{aligned}\angle \mathbf{U}_{jk} &= \frac{2\pi\nu}{c}\left(\mathbf{v}_j - \mathbf{v}_k\right)^T \mathbf{v}_{s,ff} + 2\pi m_{jk} \\ &= \frac{2\pi\nu}{c}\left(\mathbf{v}_j - \mathbf{v}_k\right)^T \left(\mathbf{v}_{s,ff}^o - \boldsymbol{\epsilon}\right) + 2\pi m_{jk},\end{aligned} \tag{30}$$

where $\mathbf{v}_{s,ff}^o$ is the estimate of the direction vector of the RFI and $\boldsymbol{\epsilon} = \mathbf{v}_{s,ff}^o - \mathbf{v}_{s,ff}$. Using the approximation in equation (30), define

$$\begin{aligned}\mathbf{B}_{jk} &= \angle\left[\mathbf{U}_{jk} e^{\frac{-i2\pi\nu}{c}\left(\mathbf{v}_j - \mathbf{v}_k\right)^T \mathbf{v}_{s,ff}^o}\right]\frac{c}{2\pi\nu} \\ &= \left(\mathbf{v}_j - \mathbf{v}_k\right)^T \boldsymbol{\epsilon}.\end{aligned} \tag{31}$$

The least squares method outlined in equations (28) and (29) can be used to improve the estimate $\mathbf{v}_{s,ff}^o$.

4. High-Level Overview of Proposed Algorithm

Figure 3 contains a Unified Modeling Language (UML) activity diagram of the algorithm used to distinguish between far-field and near-field sources. Initially, it is assumed that no previous RFI source was found (prev_found = 0) and that the first source to be detected lies within the far field (far_field = 1). The initial far-field assumption is made because the far-field version of the algorithm is computationally less expensive. If the far-field algorithm fails to converge ([conv == 0]), the near-field algorithm is attempted. It is also possible that the far-field algorithm converges for a near-field source; consequently, a one-dimensional classical delay beamforming imaging (1-D Search r) is done to check if the radial distance is larger than r_{nf}. If RFI was previously localized, then just the minimum error convergence stage is attempted using the previously found RFI coordinates as an initial estimate, thereby reducing computational cost and enabling the algorithm to track moving RFI sources. For the hexacopter data (see Section 7), using the tracking feature reduced the total computational time from 556 s to 5.2 s.

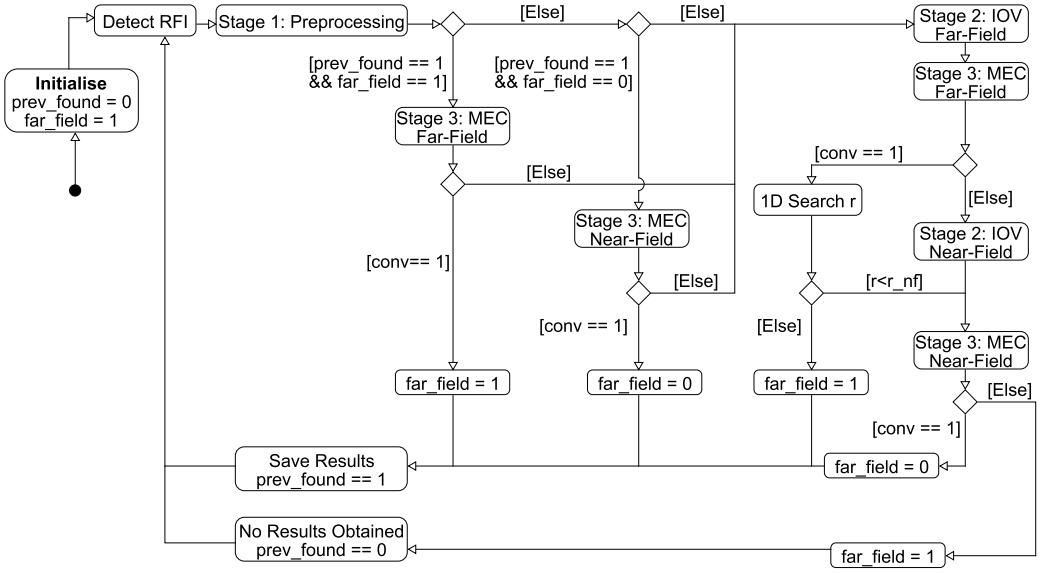

Figure 3. UML activity diagram of the proposed algorithm. MEC = minimum error convergence; IOV = integrating out variables; RFI = radio frequency interference.

5. Simulation in the Near Field

To evaluate the proposed algorithm, a simulation was done using the layout of the 48 coplanar antennas from the LOFAR CS302 station LBA subsystem (see Figure 1b) at a frequency of 44.5 MHz. A uniform distribution was used to generate 5,000 random source positions which lie outside the aforementioned array, but within the array near field. From the positions, covariance matrices were generated where the complex gains were set to $\mathbf{g}(\mathbf{V}_s) = \mathbf{1}$ and the algorithm was applied to each one. The case where the complex gains are not unity is discussed in section 7.

For only 1.46 % of the covariance matrices did the integrating-out-variables method have to iterate more than once. The reason for this is that for some directions, the beamformer has sidelobes that create peaks in f_1 that are greater than the peak at the source's angle ϕ_s. In Figure 4 plots of the number of peaks of f_1 that had to be tested as a function of the spherical coordinates of the source are given. These plots show that the region most susceptible to distortion is the reactive near field, which transitions to the radiating near field at about 200 m from the array.

For 98% of the runs, the algorithm took less than 0.2 s (the mean of all runs is 0.18 s and the maximum 1.5 s), see the histogram in Figure 5a. The relative frequency histogram in Figure 5b shows that for 98% of the runs the convergence algorithm took four or five iterations.

To measure the accuracy of the algorithm, the Euclidean distance (now called the distance error) between the position of each source ($\mathbf{v}_s$) and its corresponding estimated position ($\tilde{\mathbf{v}}_s$) was calculated. For the ith run, the Euclidean distance is then $\mathbf{d}_i = ||\mathbf{v}_{s,i} - \tilde{\mathbf{v}}_{s,i}||$. The mean distance error and mean absolute deviation for the simulation are given, respectively, by

$$\text{MDE} = \sum_i^{N_r} \frac{\mathbf{d}_i}{N_r}, \tag{32}$$

$$\text{MAD} = \sum_i^{N_r} \frac{|\mathbf{d}_i - \text{mean}(\mathbf{d})|}{N_r}, \tag{33}$$

where N_r is the number runs. The integrating-out-variables stage yielded a mean distance error of 7.57 m with a mean absolute deviation of 6.08 m (see Figure 5c). After the convergence step, without the z direction search correction step, only 0.92% of the distance errors are nonzero, see Figure 5d. These outliers all lie within 0.04 rad of the horizon and lie farther than 170 m from the array center, and the error appears in the z direction (the direction orthogonal to the plane that the array lies in). This occurs because the array is planar,

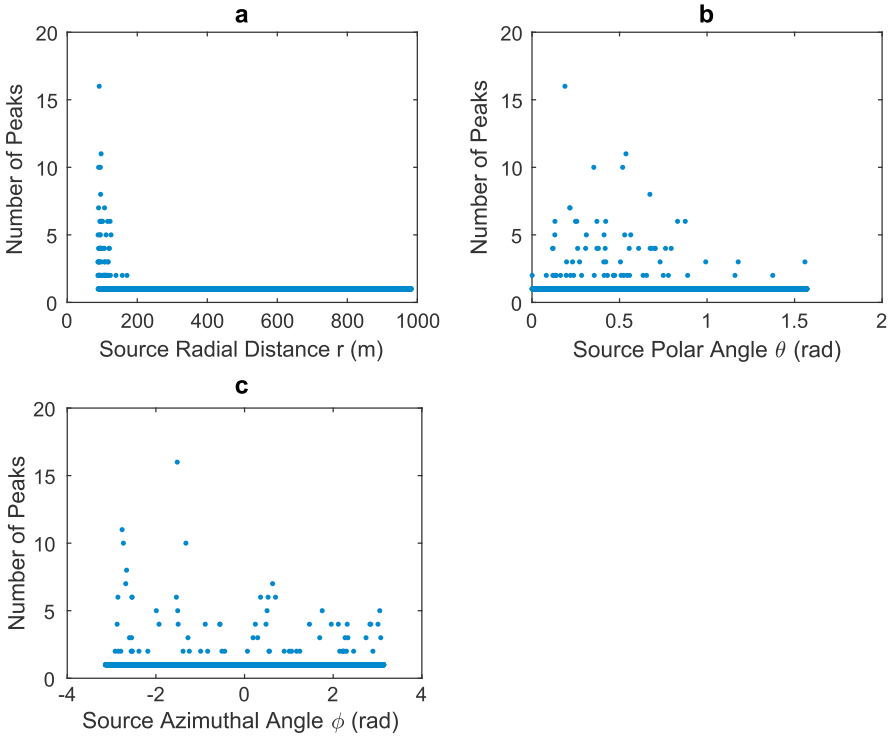

Figure 4. The number of peaks of f_1 which had to be tested before the threshold condition was met, (a) as function of the radial distance of the source, (b) as a function of the polar angle of the source, and (c) as a function of the azimuthal angle of the source.

and therefore, it is more difficult to resolve the *z* coordinate for sources further away from the array and closer to the horizon. After the convergence stage, with a *z* direction search correction step (see section 3.3.1), the mean and the spread of the distance errors are reduced to 0 (this is only possible because there is no noise or calibration errors in the simulated system).

6. Calibration Error Performance

To test the effect of direction-independent calibration errors on the algorithm, a normal distribution was used to generate phases to calculate **g** (see equation (6)). The distribution has mean 0 and the standard deviation was varied between 0 and $\pi/3$ radians. At the final standard deviation of $\pi/3$, 99.73% of the values lie within a π rad band around the mean. For each standard deviation a thousand realizations for each antenna were calculated. In Figure 6a two plots are given for the averaged results of the thousand realizations. The first shows that the averaged normalized CDB spectrum deteriorates as a function of standard deviation, while the second plot shows that the mean distance error increases linearly. The threshold of a successful estimation was set to a mean distance error of 135 m (this is the mean distance error value where the averaged normalized CDB spectrum is at half power and the standard deviation is the same). In Figure 6b, the proportion or simulated probability of an incorrect estimation is approximately zero for standard deviation in $[0, \pi/12]$. However, for standard deviation in $(\pi/12, \pi/3]$ the simulated probability increases approximately linearly from 0 to 0.43.

7. Testing of the Algorithm on Data From a LOFAR Station

The algorithm is further validated by using data generated by 48 LBAs from LOFAR station CS302 when a hexacopter was flown around the array broadcasting continuous-wave signals with different frequencies (Bolli et al., 2017). The time series data of the subband with center frequency 44.5 MHz was selected, and every 0.2 s the data was correlated for 20 ms (this short correlation time was chosen so that the hexacopter could be assumed stationary). Furthermore, the hexacopter recorded its location using differential GPS (accuracy ~1 cm) and this information was used to calculate the distance errors (GPS data were recorded every 0.2 s). The main difference between the simulation and real data is that the complex gains $\mathbf{G}(\mathbf{V}_s)$ are no longer 1,

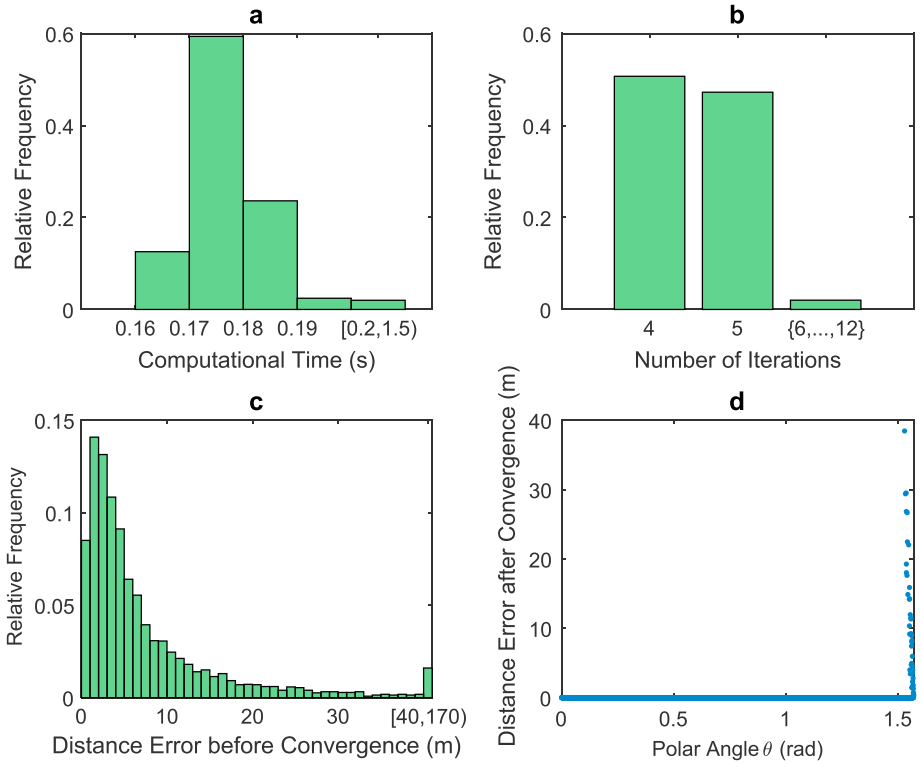

Figure 5. (a) Relative frequency histogram of the computational time for 5,000 runs. (b) Relative frequency histogram of the number of iterations required by the convergence stage for 5,000 runs. (c) Relative frequency histogram of the distance error before the convergence stage for 5,000 runs. (d) Distance error after the convergence stage as a function of polar angle θ for 5,000 runs without a z direction search correction step (see section 3.3.1).

since the array is not calibrated. After the convergence stage the mean distance error reduced from 4 m to 2 m (with mean absolute deviation of 1.16 m) which is less than the wavelength of 6.7 m, see Figure 7a. The mean distance error for the hexacopter data, before the convergence stage, is smaller than that of the simulation. This is due to the simulation containing sources with locations that are more challenging for stage 2 to resolve. However, after the convergence stage the simulation showed no error in the estimated location.

The distance error plot in Figure 7a forms an oscillating curve and has a pattern similar to the plot of the radial distance that the hexacopter is from the array. This is due to the effect of antenna gain errors on the covariance

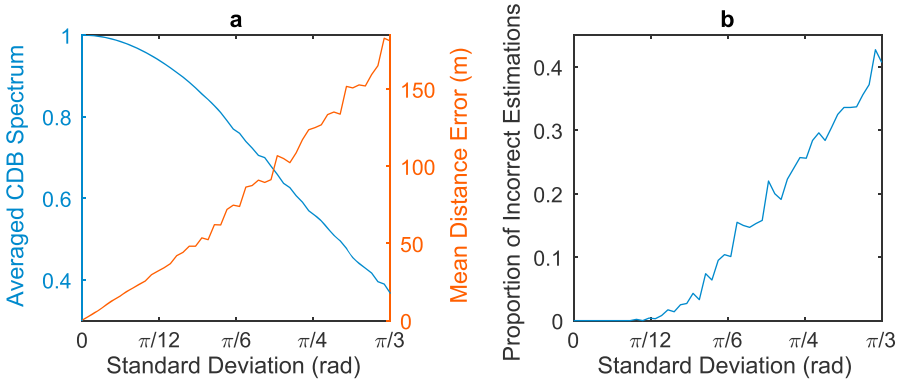

Figure 6. (a) Plots of averaged normalized classical delay beamformer (CDB) spectrum and mean distance error, respectively, as a function of standard deviation. (b) Simulated probability for incorrect estimation of radio frequency interference location plotted against standard deviation.

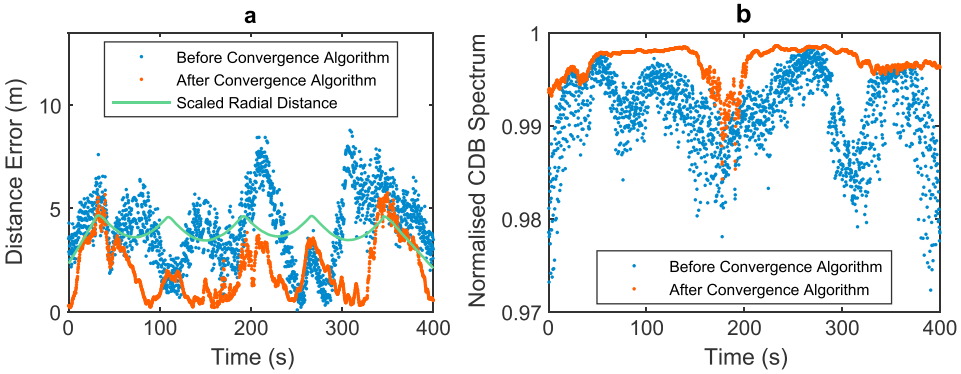

Figure 7. (a) Distance errors before and after the convergence stage for 2,000 sample covariance matrices, observed over time. The scaled plot of the hexacopter radial distances has a pattern similar to that of the distance error plots. (b) The normalized CDB spectrum before the convergence stage and after the convergence stage, observed over time.

matrix, which increases the distance error as the radial distance of the hexacopter increases. Another measure of performance is to calculate the normalized classical delay beamformer spectrum, where a score of 1 means that the model perfectly describes the sampled covariance matrix which has been modified to contain only phase information for one source, see **U** in section 3.1. In Figure 7b it is shown that the convergence stage increases the accuracy of the model. In Figure 8, plots are given for the GPS and estimated coordinates of the hexacopter over time and these show how closely the estimated values follow the GPS values.

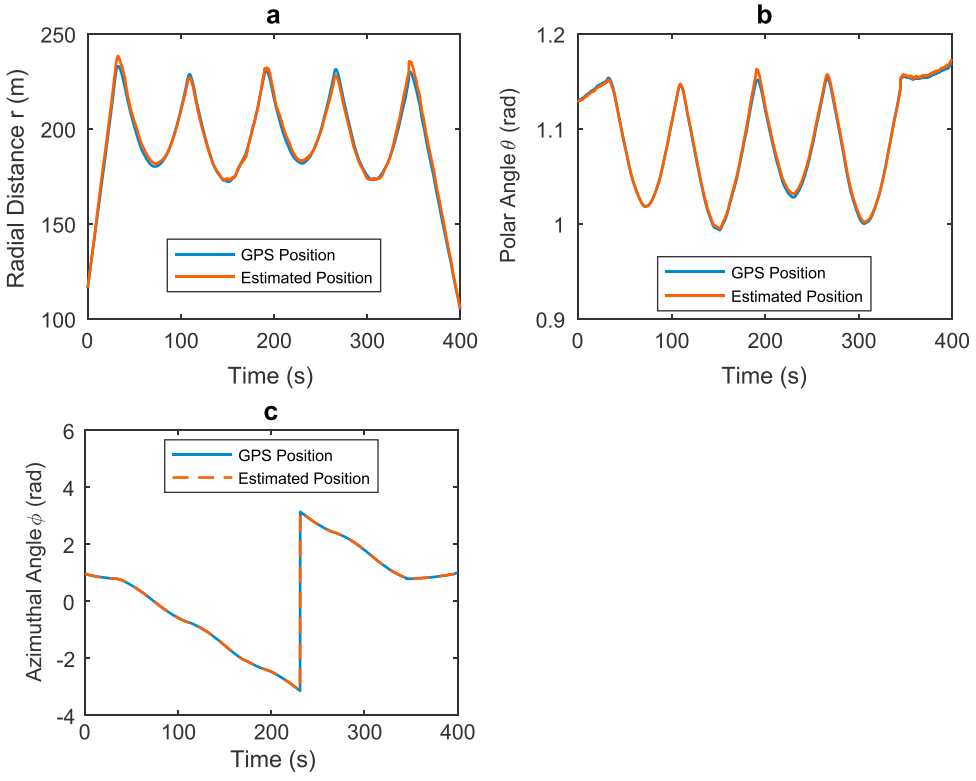

Figure 8. (a) GPS and estimated radial distances of the hexacopter from the array center, observed over time. (b) GPS and estimated polar angles of the hexacopter from the array center, observed over time. (c) GPS and estimated azimuthal angles of the hexacopter from the array center, observed over time.

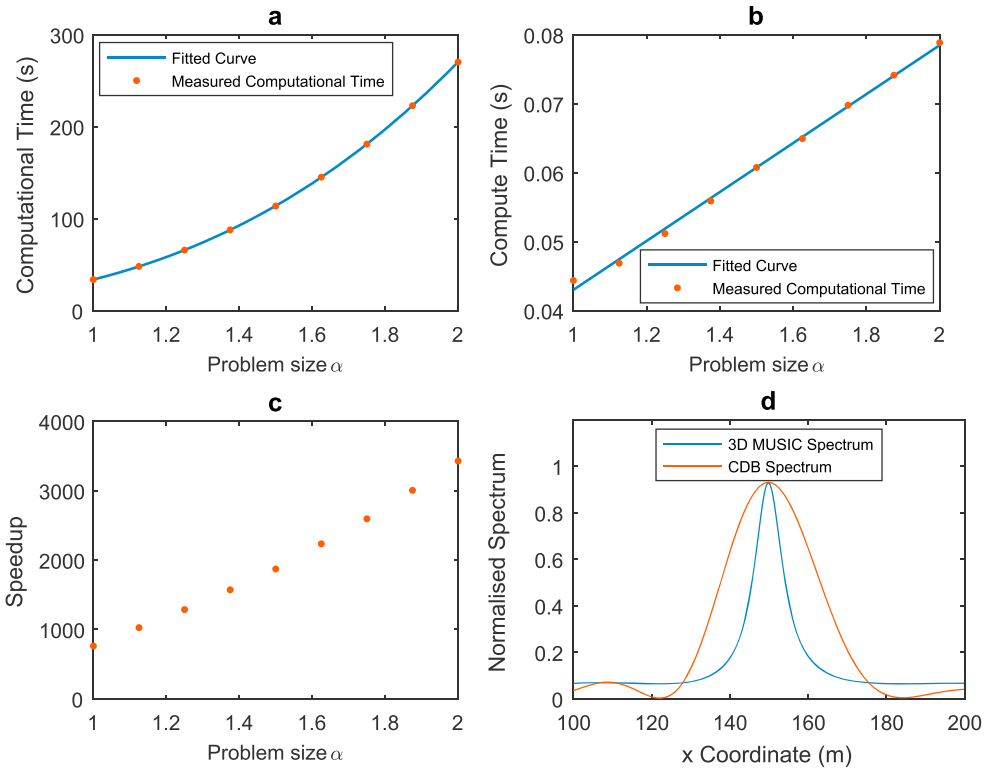

Figure 9. The problem size α is the factor by which the resolution is increased. (a) Computational time using the 3-D MUSIC algorithm with a fitted cubic polynomial. (b) Proposed algorithm with a fitted straight line. (c) Speedup of proposed algorithm relative to 3-D MUSIC. (d) Normalized spectrums for classical delay beamformer (CDB) and 3-D MUSIC with *y* and *z* coordinates fixed for data from the hexacopter measurement, see Section 7.

8. Performance Comparison Between Proposed Algorithm and 3-D MUSIC

To compare the performance of the proposed algorithm to 3-D MUSIC, a simulation was preformed where the computational time was measured for different search grid sizes. The starting search grid size of $[N_r, N_\theta, N_\phi] = [128, 128, 128]$ was scaled by $\alpha \in [1, 2]$. As expected, the computational time of the 3-D MUSIC algorithm increased cubic with search grid size, while the new proposed algorithm increases linearly; see Figures 9a and 9b, respectively. A significant speedup of at least 2 orders of magnitude was achieved using a desktop computer with an Intel Core i5-2500k chip; see Figure 9c.

Both 3-D MUSIC and the proposed algorithm have the same accuracy, since they both converge to the same peak, see Figure 9d. The lower resolution of the CDB is not a concern, since the preprocessing in stage 1 separates the RFI sources.

9. Conclusion

A new localization algorithm for interferometric arrays with low-array beam sidelobes is proposed. The algorithm is validated using simulations and has a similar accuracy to the 3-D MUSIC algorithm. The advantage of the proposed algorithm is that the computational complexity is reduced from $\mathcal{O}(N_r \times N_\theta \times N_\phi)$ to $\mathcal{O}(N_r + N_\theta + N_\phi)$. The drawback is that the algorithm introduces weighting matrices that have to be calculated once a priori and stored. The method was also applied to uncalibrated data generated by a LOFAR station while a hexacopter was flying around the array and broadcasting a continuous-wave signal. For this data, the mean distance between the estimated positions of the hexacopter and the corresponding real positions is 2 m (with mean absolute deviation of 1.16 m) which is less than the wavelength of 6.7 m. These results clearly demonstrate the accuracy and precision of the proposed algorithm to locate RFI sources.

10. Special Functions

In this paper, we use several special functions, which are briefly introduced below. The Exponential integral, denoted by E_1 is given by

$$\mathrm{E}_1(z) = \int_z^\infty \frac{e^{-t}}{t}\mathrm{d}t = -\gamma - \ln(z) - \sum_{k=1}^{\infty}\frac{(-z)^k}{kk!}, \tag{34}$$

where $\{z \in \mathbb{C}:|\angle z| < \pi\}$ and γ is the Euler-Mascheroni constant. The Bessel function of the first kind, denoted by J_0, is given by

$$J_0(x) = \frac{2}{\pi}\int_0^{\pi/2}\cos(x\sin(\theta))\mathrm{d}\theta = \sum_{k=0}^{\infty}(-1)^k\frac{\left(\frac{1}{4}x^2\right)^k}{(k!)^2}, \tag{35}$$

where $x \in \mathbb{R}$. The Modified Bessel function of the first kind, denoted by I_0 is given by

$$I_0\left(\sqrt{-x^2-y^2}\right) = \frac{1}{2\pi}\int_0^{2\pi} e^{i(x\sin(\theta)+y\cos(\theta))}\mathrm{d}\theta = \sum_{k=0}^{\infty}(-1)^k\frac{\left(\frac{1}{4}(x^2+y^2)\right)^k}{(k!)^2}, \tag{36}$$

where $x, y, \in \mathbb{R}$. The Struve function, denoted by H_0 is, given by

$$H_0(x) = \frac{2}{\pi}\int_0^{\pi/2}\sin(x\sin(\theta))\mathrm{d}\theta = \frac{2}{\pi}\sum_{k=1}^{\infty}\frac{(-1)^k}{[(2k+1)!!]^2}x^{2k+1}, \tag{37}$$

where $x \in \mathbb{R}$.

Notation

- $\mathbf{A}$ Bold upper-case letters are matrices. The jkth element is indicated by $\mathbf{A}_{jk}$.
- $\mathbf{a}$ Bold lower-case letters are column vectors. The jth element is indicated by $\mathbf{a}_j$.
- $\mathbf{I}$ Identity matrix.
- $\odot$ Hadamard product.
- $||\cdot||$ Euclidean norm of a vector.
- $\mathrm{diag}(\cdot)$ Converts a vector into a diagonal matrix.
- $\angle$ Argument of a complex number.
- i Square root of -1.
- c Speed of light.
- $\{\cdot\}^H$ Hermitian transpose of a matrix.
- $\{\cdot\}^T$ Transpose of a matrix.
- $\{\cdot\}^*$ Complex conjugate of a scalar.
- $\Re(\cdot)$ Real part of a complex number.
- $\mathbb{E}\{\cdot\}$ Expectation operator.

Acknowledgments
This work is funded and supported by IBM, ASTRON, the Dutch Ministry of Economic Affairs and the Province of Drenthe, SKA South Africa, the South African Research Chairs Initiative of the Department of Science and Technology, the National Research Foundation of South Africa, and the Netherlands Organisation for Scientific Research. Data and MATLAB code can be found at https://www.dropbox.com/sh/qiea2tck9vtqonq/AACPfMEzdlbY3aVNlWCBg0d8a?dl=0.

References

Balanis, C. A., & Ioannides, P. I. (2007). *Introduction to smart antennas*. San Rafael, CA: Morgan & Claypool Publishers.

Bolli, P., Wijnholds, S. J., de Lera Acedo, E., Lingua, A., Monari, J., Paonessa, F., … Virone, G. (2017). In-situ characterization of international low-frequency aperture arrays by means of an UAV-based system. In *URSI General Assembly and Scientific Symposium (URSI GASS)*. Montreal (Canada).

Challa, R., & Shamsunder, S. (1995). High-order subspace-based algorithms for passive localization of near-field sources. *Proceedings of ASILOMAR-29*, *2*, 777–781. https://doi.org/10.1109/ACSSC.1995.540806

Grosicki, E., Abed-Meraim, K., & Hua, Y. (2005). A weighted linear prediction method for near-field source localization. *IEEE Transactions on Signal Processing*, *53*(10), 3651–3660. https://doi.org/10.1109/TSP.2005.855100

Huang, Y. D., & Barkat, M. (1991). Near-field source localization by passive sensor array. *IEEE Transactions on Antennas and Propagation*, *39*(7), 968–975. https://doi.org/10.1109/8.86917

Hung, H., Chang, S., & Wu, C. (1996). 3-D MUSIC with polynomial rooting for near-field source localization. *ICASSP*, *6*, 3065–3068. https://doi.org/10.1109/ICASSP.1996.550523

Sardarabadi, A. M., van der Veen, A., & Boonstra, A. (2015). Spatial filtering of RF interference in radio astronomy using a reference antenna array. *IEEE Transactions on Signal Processing*, *64*(2), 432–447. https://doi.org/10.1109/TSP.2015.2483481

Sardarabadi, A. M. (2016). Covariance matching techniques for radio astronomy (PhD Thesis), Delft University of Technology. https://doi.org/10.4233/uuid:3eb46b5b-126c-4d95-8821-fb71ce404cac

Starer, D., & Nehorai, A. (1994). Passive localization of near-field sources by path following. *IEEE Transactions on Signal Processing*, *42*(3), 677–680. https://doi.org/10.1109/78.277864

Thompson, A. R., Moran, J. A., & Swenson Jr., G. W. (2004). *Interferometry and synthesis in radio astronomy second edition*. Weinheim, Germany: WILEY-VCH Verlag GmbH & Co. KGaA. https://doi.org/10.1002/9783527617845

van der Tol, S., & van der Veen, A. (2005). Performance analysis of spatial filtering of RF interference in radio astronomy. *IEEE Transactions on Signal Processing*, *53*(3), 896–910. https://doi.org/10.1109/TSP.2004.842177

van der Veen, A., Leshem, A., & Boonstra, A. (2004). Signal processing for radio astronomical arrays. In *Sensor Array and Multichannel Signal Processing Workshop Proceedings* (pp. 1–10). Barcelona, Spain, Spain. https://doi.org/10.1109/SAM.2004.1502901

van Haarlem, M. P., Wise, M. W., Gunst, A. W., Heald, G., McKean, J. P., Hessels, J. W. T., … van Zwieten, J. (2013). LOFAR: The low frequency array. *Astronomy & Astrophysics*, *556*(A2), 1–53. https://doi.org/10.1051/0004-6361/201220873

Weiss, A. J., & Friedlander, B. (1993). Range and bearing estimation using polynomial rooting. *IEEE Journal of Oceanic Engineering*, *18*(2), 130–137. https://doi.org/10.1109/48.219532

Wijnholds, S. J., Pupillo, G., Bolli, P., & Virone, G. (2016). UAV-aided calibration for commissioning of phased array radio telescopes. In *URSI Asia-Pacific Radio Science Conference (URSI AP-RASC)* (pp. 228–231). Seoul, South Korea. https://doi.org/10.1109/URSIAP-RASC.2016.7601375

Yuen, N., & Friedlander, B. (1998). Performance analysis of higher order ESPRIT for localization of near-field sources. *IEEE Transactions on Signal Processing*, *46*(3), 709–719. https://doi.org/10.1109/78.661337

Zatman, M. (1998). How narrow is narrowband? *IEE Proceedings-Radar, Sonar and Navigation*, *145*(2), 85–91. https://doi.org/10.1049/ip-rsn:19981670

2.5 Journal Paper - Mitigation of Non-Narrowband Radio Frequency Interference

2nd URSI AT-RASC, Gran Canaria, 28 May – 1 June 2018

Mitigation of Non-Narrowband Radio Frequency Interference

Jan-Willem W. Steeb*(1), David B. Davidson(2)(1), and Stefan J. Wijnholds(3)(1)
(1) Department of Electrical & Electronic Engineering, Stellenbosch University, South Africa
(2) International Centre for Radio Astronomy Research (ICRAR), Curtin University, Australia
(3) Netherlands Institute for Radio Astronomy (ASTRON), The Netherlands

Abstract

The rapid development and implementation of wireless communication standards put increasing pressure on spectrum allocation and therefore threatens the efficacy of radio astronomy. For example, digital audio broadcasting (DAB) is a wide-bandwidth broadcast technology that is now being implemented and has spectrum allocated in the L band. We demonstrate that standard narrowband subspace subtraction methods may provide insufficient suppression of such signals. We therefore propose two algorithms that take into account the non-narrowband nature of these signals. The first proposed algorithm is based on a flat frequency response model and the second is an approximation of the first that makes use of two frequency-shifted monochromatic sources (Zatman's model). An experimental demonstration of both proposed algorithms yielded an increase of approximately a factor six in bandwidth per channel that can be processed when compared to conventional narrowband techniques (for the same attenuation of the RFI signal). The performance of the two methods is identical for LOFAR station configurations with bandwidths between 763 Hz and 195 kHz. However, the Zatman's model based algorithm requires less operations (a speed-up of 1.3 was achieved). An equation is derived which gives the direction of arrival for a far-field non-narrowband signal that causes the greatest distortion of the visibilities. Another equation is derived for the appropriate frequency channel bandwidth at which to implement the proposed non-narrowband RFI mitigation algorithms.

1 Introduction

In the development of radio frequency interference (RFI) mitigation methods, the assumption that the RFI is narrowband, is usually made. If this is the case, spatial RFI mitigation methods such as orthogonal projection, orthogonal projection with subspace bias correction, oblique projection and subspace subtraction [1, 2, 3] can be applied. When the signal is not narrowband, the model for the array response vector becomes a function of bandwidth. The result is that the RFI will appear as an extended source that can be modelled as multiple sources, albeit with rapidly decreasing power. To evaluate the proposed RFI mitigation methods, the layout of High Band Antenna (HBA) station RS407 in the Low Frequency Array (LOFAR) [4] is used. The HBA stations in LOFAR have an operating band from 110 to 240 MHz, which contains many digital audio broadcasts.

To demonstrate the effect of bandwidth on a sky image a simulation was done using the layout of a LOFAR HBA station. In figure 1a the skymap is dominated by the RFI source. When a first order orthogonal projection filter is applied, the skymap in figure 1b is obtained. The orthogonal projector reduces the power of the RFI source by 40 dB and reveals two sources which are seperated along the radial direction. These two sources are not real physical sources, but are caused by frequency smearing [5].

Two signal models are used, a flat frequency response model and Zatman's approximation [6]. Furthermore, equations will be derived for the RFI covariance matrix's eigenvalues, as well as for the direction of arrival that causes the largest deviation from the narrowband point source model, the appropriate bandwidth at which to apply spatial filtering and the RFI covariance matrix's vector space. Two new subspace subtraction algorithms, that make use of the two models developed for the RFI covariance matrix's vector space, are subsequently presented and evaluated.

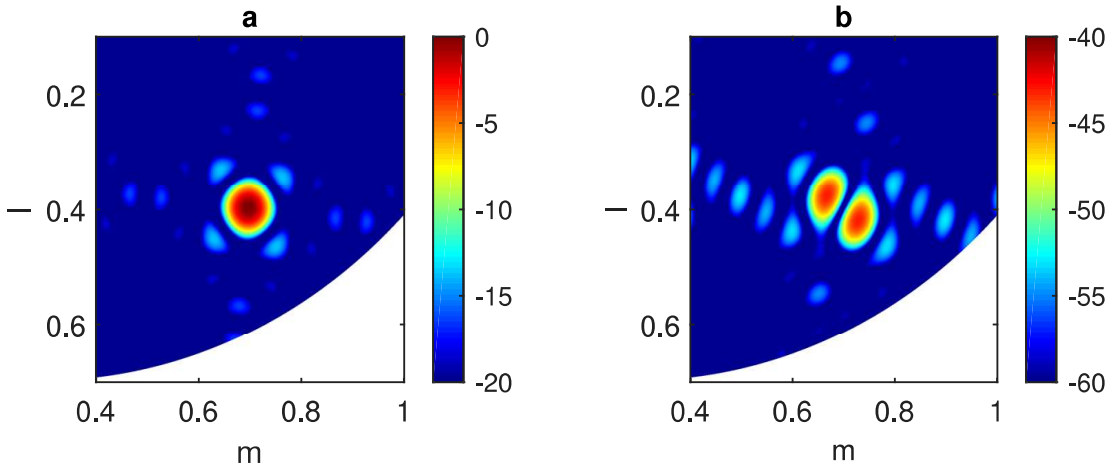

Figure 1. (a) Skymap with non-narrowband RFI source visible in dB (the RFI source is the 0 dB point). **(b)** Skymap with non-narrowband RFI source removed, using a first order orthogonal projection filter. Two weaker sources adjacent to the location of the RFI are now visible and are caused by the bandwidth of the RFI source.

2 Notation

$\mathbf{A}$	Bold upper-case letters are matrices. The jk^{th} element is indicated by $\mathbf{A}_{jk}$.
$\mathbf{a}$	Bold lower-case letters are column vectors. The j^{th} element is indicated by $\mathbf{a}_j$.
$\mathbf{I}$	Identity matrix.
$\odot$	Hadamard product.
$\lvert\cdot\rvert$	Absolute value of a scalar.
$\text{Tr}(\cdot)$	Trace of a matrix.
$\text{diag}(\cdot)$	Converts a vector into a diagonal matrix.
$\angle$	Phase of a complex number.
i	Square root of -1.
c	Speed of light.
$\{\cdot\}^H$	Hermitian transpose of a matrix.
$\{\cdot\}^T$	Transpose of a matrix.
$\{\cdot\}^*$	Complex conjugate of a scalar.
$\text{sinc}(x)$	$= \sin(\pi x)/(\pi x)$, normalized sinc function.
$\delta(x)$	Dirac delta function.

3 Narrowband Signal Model

If omnidirectional antennas are used, then the normalized array response vector for an array with N_e elements and a continuous wave source with frequency ν is given by

$$\mathbf{a} = \begin{bmatrix} b_1 e^{-\text{i}2\pi\nu\tau_1} \\ \vdots \\ b_{N_e} e^{-\text{i}2\pi\nu\tau_{N_e}} \end{bmatrix}. \tag{1}$$

If the source lies in the far-field, then the geometrical delays and normalization constants are

$$\tau_j = -(l_s x_j + m_s y_j + n_s z_j)/c, \tag{2}$$
$$b_j = 1/\sqrt{N_e}, \tag{3}$$

where x_j, y_j, z_j are the Cartesian coordinates of the j^{th} antenna and the directional cosines are defined as

$$l_s = \sin(\theta_s)\cos(\phi_s), \tag{4}$$
$$m_s = \sin(\theta_s)\sin(\phi_s), \tag{5}$$
$$n_s = \cos(\theta_s), \tag{6}$$

where θ_s and ϕ_s are, respectively, the polar and azimuthal angles of the spherical coordinates of the source (ISO convention). The array covariance matrix for a single source without noise is given by

$$\mathbf{R} = \sigma_s^2 \mathbf{a}\mathbf{a}^H, \tag{7}$$

$$\mathbf{R}_{jk} = b_j b_k \sigma_s^2 e^{-i2\pi\tau_{jk}\nu}, \tag{8}$$

where σ_s^2 is the signal power, $\mathbf{R}_{jk}$ is the jk^{th} element in the covariance matrix and $\tau_{jk} = \tau_j - \tau_k$.

All examples in this paper make use of sources in the far-field. However, any of the presented methods can be used for near-field sources by setting $\tau_j = r_{sj}/c$ and $b_j = 1/\left[r_{sj}\sqrt{\sum_{n=1}^{N_c} 1/r_{sn}^2}\right]$, where the distance between the j^{th} antenna and the source is denoted by r_{sj} [7].

4 Non-Narrowband Signal Model

If the channel bandwidth is not sufficiently narrow, the dependence of the array response vector on frequency becomes significant. The frequency dependent covariance matrix $\mathbf{R}(\nu)$ with only a single interferer (no noise or cosmic sources), that is modelled as a point source, can be written as

$$\mathbf{R}(\nu) = \sigma_s^2(\nu)\mathbf{a}(\nu)\mathbf{a}^H(\nu), \tag{9}$$

where $\mathbf{a}(\nu)$ is the normalized frequency dependent array response vector. When the different frequency components are uncorrelated, the total covariance matrix is found by integrating over the entire bandwidth

$$\mathbf{R} = \frac{1}{\Delta\nu}\int_{\nu_0-\Delta\nu/2}^{\nu_0+\Delta\nu/2} \sigma_s^2(\nu)\mathbf{a}(\nu)\mathbf{a}^H(\nu)d\nu, \tag{10}$$

where $\Delta\nu$ is the bandwidth and ν_0 is the center frequency. For a flat frequency response, the integral in equation (10) can be calculated and the jk^{th} element is given by

$$\mathbf{R}_{jk} = \frac{\sigma_s^2 b_j b_k}{\Delta\nu}\int_{\nu_0-\Delta\nu/2}^{\nu_0+\Delta\nu/2} e^{-i2\pi\tau_{jk}\nu}d\nu = \sigma_s^2 b_j b_k \,\mathrm{sinc}(\tau_{jk}\Delta\nu)e^{-i2\pi\tau_{jk}\nu_0}. \tag{11}$$

By taking the bandwidth into consideration (and assuming a flat frequency response) this covariance matrix model differs from the narrowband model (see equation (8)) with a sinc function that is dependent on the delay τ_{jk} and the bandwidth $\Delta\nu$. As the bandwidth increases from a single frequency, the sinc function starts to decrease from unity and the effect is that the covariances start to decorrelate. This causes the eigenvalue structure of the array covariance matrix to change. For a single frequency signal there will only be one non-zero eigenvalue. For a non-zero bandwidth signal the covariance matrix will be of full rank, since it is an infinite sum of frequencies. As the bandwidth increases, the largest eigenvalue will decrease and the other eigenvalues will increase, as can be seen in figure 2a (where, even though the largest eigenvalue appears constant due to the log scale of the figure, it is decreasing). However, most of the eigenvalues will be so small relative to the cosmic sources and the noise in the system, that they can be approximated by zero. The effective rank of the RFI covariance matrix (no noise or cosmic sources) is then defined to be equal to the number of eigenvalues that are significant when compared to the eigenvalues of the covariance matrix that contains only the cosmic sources and noise.

The entire fractional bandwidth range used to generate figure 2a would be considered narrowband in the traditional signal processing sense. However, the power of some RFI sources is so high that it can be more than 70 dB above the noise and even 60 dB above a bright radio source such as Cassiopeia A. Therefore, the contribution of the RFI source to the second eigenvalue can still be significant relative to that of the cosmic sources. Figure 2b shows a plot of the three largest eigenvalues from an observation using LOFAR HBA station RS407 as a function of center frequency. The bandwidth used for the observation is 195 kHz and the DAB signal can be clearly seen from 182.9 to 184.4 MHz. The second eigenvalue for the DAB signal is at approximately -40 dB and agrees with the simulated results in figure 2a. There is however no agreement between the simulated and measured third eigenvalue. This is due to calibration errors and the frequency response not being perfectly flat.

5 Zatman's Approximation Based Model

If a covariance matrix has an effective rank of two, it can be approximated by the sum of two discrete uncorrelated signals

$$\mathbf{R} \approx \sigma_1^2 \mathbf{a}_1\mathbf{a}_1^H + \sigma_2^2 \mathbf{a}_2\mathbf{a}_2^H. \tag{12}$$

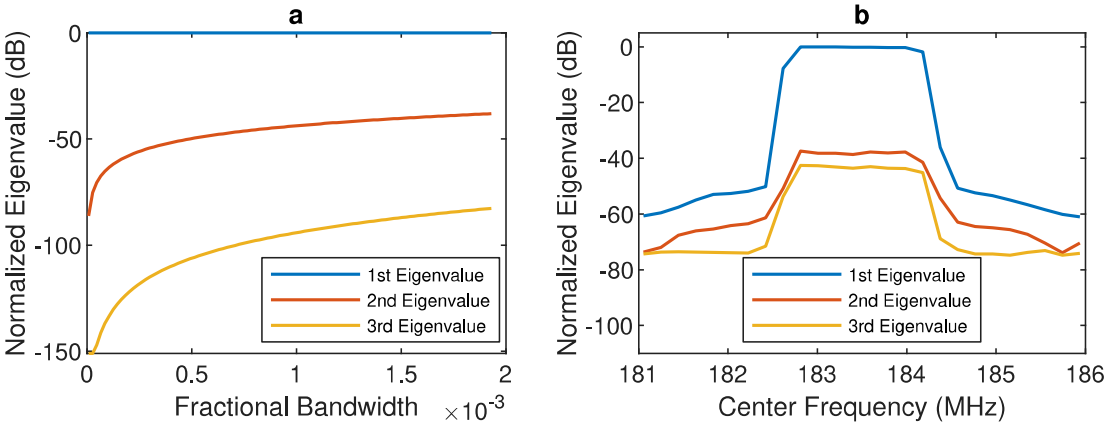

Figure 2. **(a)** A plot of the simulated (assuming a flat frequency response) three largest normalized eigenvalues as a function of fractional bandwidth using the layout of the LOFAR HBA station RS407 and an RFI source on the horizon. The center frequency is 183 MHz and the bandwidth was varied from 763 Hz to 195 kHz. **(b)** The three largest normalized eigenvalues as a function of center frequency calculated from the covariance matrices obtained from an observation using LOFAR station RS407 with a bandwidth of 195 kHz. The elevated flat spectrum of a DAB signal can clearly be seen between 182.9 to 184.4 MHz.

The closed form solution for the eigenvalues of the system given in equation (12) are [3, p. 65]

$$\lambda_{1,2} = \frac{1}{2}(\sigma_1^2 + \sigma_2^2)\left(1 \pm \sqrt{1 - 4\frac{\sigma_1^2\sigma_2^2(1 - |\mathbf{a}_1^H\mathbf{a}_2|^2)}{(\sigma_1^2 + \sigma_2^2)^2}}\right). \tag{13}$$

In the model proposed by Zatman the signals are required to have equal power ($\sigma_1^2 = \sigma_2^2 = \sigma^2$) [6]. The equal power criterion is achieved when the discrete sources are arranged in such a way that the instantaneous frequency spectrum mean and variance correspond to the mean and variance of the non-zero bandwidth signal, respectively. Consequently, the distance from the center frequency ν_0 is given by

$$\kappa = \frac{\Delta\nu}{2\sqrt{3}}. \tag{14}$$

Thus, the model in equation (12) becomes

$$\mathbf{R} \approx \sigma^2\mathbf{a}(\nu_0 + \kappa)\mathbf{a}^H(\nu_0 + \kappa) + \sigma^2\mathbf{a}(\nu_0 - \kappa)\mathbf{a}^H(\nu_0 - \kappa) = \sigma^2(\mathbf{a}_1\mathbf{a}_1^H + \mathbf{a}_2\mathbf{a}_2^H). \tag{15}$$

Zatman's approach is now generalized from a uniform linear array to an array of any shape using the normalized response vector in equation (1) and the assumption that $\sigma_1^2 = \sigma_2^2 = \sigma^2$. Consequently, equation (13) simplifies to

$$\lambda_{1,2} = \sigma^2[1 \pm |\psi|], \tag{16}$$

where $\psi = \mathbf{a}_1^H\mathbf{a}_2$. In figure 3a the power spectral density of the flat frequency model, as well as the Zatman's approximation based model, is plotted. In the frequency domain the Zatman's approximation based model is represented by two frequency shifted Dirac deltas. The total covariance matrix for the Zatman's approximation based model is found by integrating over the entire bandwidth (see equation (11) for the flat frequency model case)

$$\begin{aligned}\mathbf{R}_{jk} &\approx \frac{\sigma_s^2 b_j b_k}{2}\left[\int_{-\infty}^{\infty}\delta(\nu - \nu_0 + \kappa)e^{-\mathrm{i}2\pi\tau_{jk}\nu}d\nu + \int_{-\infty}^{\infty}\delta(\nu - \nu_0 - \kappa)e^{-\mathrm{i}2\pi\tau_{jk}\nu}d\nu\right] \\ &= \sigma_s^2 b_j b_k \cos\left(\pi\tau_{jk}\Delta\nu/\sqrt{3}\right)e^{-i2\pi\tau_{jk}\nu_0}.\end{aligned} \tag{17}$$

Where the flat frequency model causes a $\mathrm{sinc}(\tau_{jk}\Delta\nu)$ decorrelating function to appear, the Zatman's approximation based model results in a $\cos\left(\pi\tau_{jk}\Delta\nu/\sqrt{3}\right)$ decorrelating function for the total covariance matrix (see figure 3b for plots of the decorrelating functions). There is agreement between the models for the peak centred at $\Delta\nu = 0$, however as the bandwidth increases the Zatman decorrelating function oscillates and the flat frequency decorrelating function attenuates. At a bandwidth of $\Delta\nu = 1/\tau_{jk}$ the flat frequency decorrelating function is zero. Using the LOFAR HBA sation RS407 longest baseline and assuming the longest delay possible, yields $\Delta\nu = 7.65$ MHz, which is far larger than any LOFAR channel bandwidth. For the standard channel bandwidth of 195 kHz the difference between the two models' decorrelating function (in the case of the longest possible delay) is only -1.52×10^{-7}. Therefore, the Zatman's approximation based model is adequate for modelling LOFAR HBA signals with a flat frequency response.

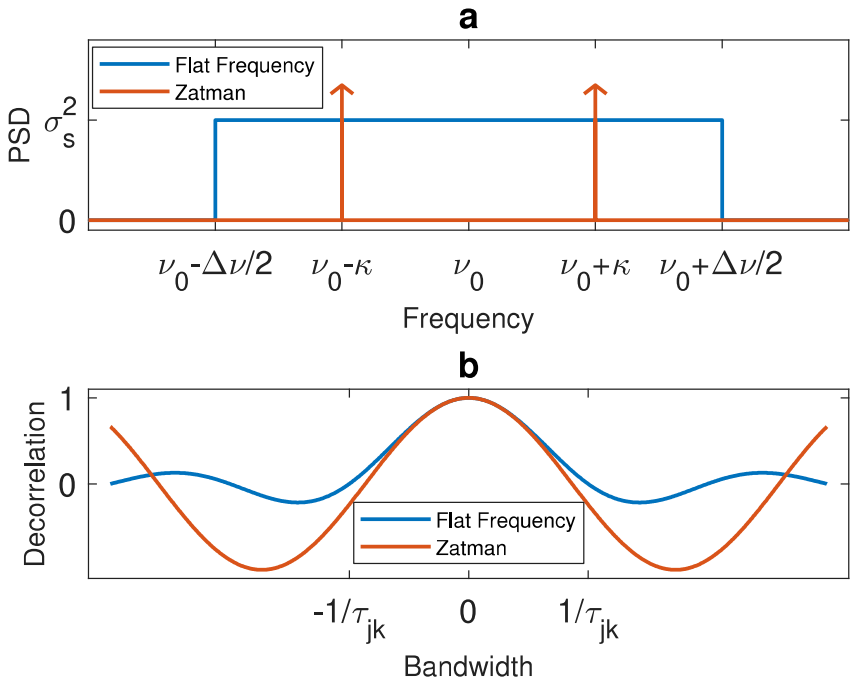

Figure 3. **(a)** Power Spectral Density (PSD) as a function of frequency. The flat frequency model is represented by a square pulse and the Zatman's approximation based model is represented by two frequency shifted Dirac deltas. **(b)** Decorrelation as a function of bandwidth. The decorrelating function for the flat frequency model covariance matrix is $\text{sinc}(\tau_{jk}\Delta\nu)$ and for the Zatman's approximation based model it is $\cos\left(\pi\tau_{jk}\Delta\nu/\sqrt{3}\right)$.

5.1 Worst Case Scenario

Minimizing $|\psi|$ maximizes λ_2, which is the worst case scenario. Also, minimizing $|\psi|^2$ is the same as minimizing $|\psi|$, since it is a positive function. After expanding and simplifying

$$|\psi|^2 = \sum_{p=1}^{N_e} b_p^4 + \sum_{j=1}^{N_e-1}\sum_{k=j+1}^{N_e} 2b_j^2 b_k^2 \cos\left(4\pi\tau_{jk}\kappa\right). \tag{18}$$

We will make the following assumptions:

- The array is planar (that is, $z_{jk} = 0$).
- The RFI source lies in the far-field (therefore use equations (2) and (3)).
- The argument $4\pi\tau_{jk}\kappa << \pi/2$, therefore the Taylor expansion $\cos(x) \approx 1 - \frac{x^2}{2}$ can be used.

Using these assumptions, equation (18) simplifies to

$$|\psi|^2 = 1 - \frac{16\pi^2\kappa^2}{N_e^2}\left[\sum_{j=1}^{N_e-1}\sum_{k=j+1}^{N_e}\tau_{jk}^2\right] = 1 - \frac{16\pi^2\kappa^2}{N_e^2}[\alpha_1 l^2 + \alpha_2 lm + \alpha_3 m^2] = 1 - \frac{16\pi^2\kappa^2}{N_e^2}\zeta(l,m), \tag{19}$$

where

$$\alpha_1 = \sum_{j=1}^{N_e-1}\sum_{k=j+1}^{N_e}\frac{x_{jk}^2}{c^2}, \quad \alpha_2 = 2\left(\sum_{j=1}^{N_e-1}\sum_{k=j+1}^{N_e}\frac{x_{jk}y_{jk}}{c^2}\right), \quad \alpha_3 = \sum_{j=1}^{N_e-1}\sum_{k=j+1}^{N_e}\frac{y_{jk}^2}{c^2}, \quad \zeta(l,m) = \alpha_1 l^2 + \alpha_2 lm + \alpha_3 m^2.$$

Therefore, to minimize $|\psi|^2$ the positive function $\zeta(l,m)$ must be maximized. Substituting equations (4) to (6) into ζ yields

$$\zeta(\theta,\phi) = \sin^2\theta(\alpha_1\cos^2\phi + \alpha_2\cos\phi\sin\phi + \alpha_3\sin^2\phi). \tag{20}$$

Clearly, the positive function ζ is maximized when $\theta = \pi/2$. The partial derivative of ζ with respect to ϕ is

$$\begin{aligned}\frac{\delta\zeta}{\delta\phi} &= \sin^2\theta(-2\alpha_1\cos\phi\sin\phi - \alpha_2\sin^2\phi + \alpha_2\cos^2\phi + 2\alpha_3\sin\phi\cos\phi) \\ &= \sin^2\theta[(\alpha_3-\alpha_1)\sin(2\phi) + \alpha_2\cos(2\phi)]. \end{aligned} \tag{21}$$

Setting $\theta = \pi/2$ and $\frac{\delta\zeta}{\delta\phi} = 0$, ζ is maximized by

$$\phi = \frac{1}{2}\tan^{-1}\left(\frac{\alpha_2}{\alpha_1-\alpha_3}\right) \tag{22}$$

if $\frac{\delta^2\zeta}{\delta\phi^2} < 0$, that is

$$[(\alpha_3-\alpha_1)\cos(2\phi) - \alpha_2\sin(2\phi)] < 0. \tag{23}$$

By maximizing ζ, the arrival direction is found so that the mean delay for the RFI signal between the antennas is maximized, which then gives the largest second eigenvalue.

6 Appropriate Bandwidth for Spatial Filtering

Spatial nulling techniques work by modifying eigenvalues in the measured covariance matrix that are associated with the RFI subspace. For example, orthogonal projection makes those eigenvalues zero. As the number of eigenvalues that are modified increases, so does the loss in information [1]. Therefore, the lowest order filter that sufficiently suppresses the RFI is desired. This criterion can be met by setting the channel bandwidth so that the second eigenvalue lies sufficiently below the noise floor

$$\lambda_2 << \sigma_n^2\left(1+\sqrt{N_e/N_t}\right)^2, \tag{24}$$

where N_t is the number of samples used to estimate the array covariance matrix [1].

For a planar array, the required bandwidth can be calculated by substituting equation (19) into the equation for the ratio λ_2/λ_1 (see equation (16)) and solving for the bandwidth

$$\Delta\nu = 2\sqrt{3}\sqrt{\left[1-\left(\frac{1-\lambda_2/\lambda_1}{1+\lambda_2/\lambda_1}\right)^2\right]\frac{N_e^2}{16\pi^2\zeta(l,m)}}. \tag{25}$$

A suitable value for λ_2 can be determined by using equation (24). An approximate estimate for λ_1 can be obtained from a covariance matrix, constructed from a signal with the default array bandwidth, by computing the eigenvalue decomposition and subtracting the noise power from the largest eigenvalue. Using the default bandwidth, which is usually larger than the one calculated in equation (25), causes the estimate of λ_1 to be slightly lower and has little effect on the ratio λ_2/λ_1, since $\lambda_1 >> \lambda_2$. The l and m coordinates can either be the worst case scenario (see section 5.1) or the coordinates of the RFI, which is often known in the case of a DAB broadcast.

Increasing the bandwidth so that the second eigenvalue is above the noise and then using second order spatial filtering will not sufficiently remove the RFI. The reason is that the third eigenvalue will then have a significant impact, because no array is perfectly calibrated and the frequency response is not completely flat, which causes the third eigenvalue to be substantially higher than predicted by the model (see figure 2a and b). To increase the bandwidth that can be processed or the RFI suppression, the algorithms that are proposed in section 8 construct a second order filter that does not require the second eigenvalue to be above the noise.

7 Approximating RFI Vector Space

The RFI covariance matrix in equation (15) can be rewritten in terms of its eigenvalue decomposition

$$\mathbf{R} \approx \sigma^2(\mathbf{a}_1\mathbf{a}_1^H + \mathbf{a}_2\mathbf{a}_2^H) = \lambda_1\mathbf{v}_1\mathbf{v}_1^H + \lambda_2\mathbf{v}_2\mathbf{v}_2^H, \tag{26}$$

which maximizes the power in the direction of $\mathbf{v}_1$, with the remaining power contained in the direction of $\mathbf{v}_2$. Both vectors are linear combinations of $\mathbf{a}_1$ and $\mathbf{a}_2$,

$$\mathbf{v}_{1,2} = \beta_{1,2}\mathbf{a}_1 + \gamma_{1,2}\mathbf{a}_2, \tag{27}$$

with the following properties:

- $\mathbf{v}_1^H \mathbf{v}_1 = \mathbf{v}_2^H \mathbf{v}_2 = 1$ ($\mathbf{v}_1$ and $\mathbf{v}_2$ are unit vectors),
- $\mathbf{v}_1^H \mathbf{v}_2 = \mathbf{v}_2^H \mathbf{v}_1 = 0$ ($\mathbf{v}_1$ and $\mathbf{v}_2$ are orthogonal).

Using the definition of an eigenvector and eigenvalue

$$\mathbf{R}\mathbf{v} \approx \sigma^2(\mathbf{a}_1\mathbf{a}_1^H + \mathbf{a}_2\mathbf{a}_2^H)(\beta\mathbf{a}_1 + \gamma\mathbf{a}_2) = \sigma^2(\beta\mathbf{a}_1 + \gamma\psi\mathbf{a}_1 + \beta\psi^*\mathbf{a}_2 + \gamma\mathbf{a}_2) = \lambda\mathbf{v} = \lambda\beta\mathbf{a}_1 + \lambda\gamma\mathbf{a}_2.$$

Comparing the coefficients of $\mathbf{a}_1$ and $\mathbf{a}_2$, respectively, yields

$$\lambda\beta = \sigma^2(\beta + \gamma\psi), \tag{28}$$
$$\lambda\gamma = \sigma^2(\beta\psi^* + \gamma). \tag{29}$$

Substituting $\lambda = \lambda_{1,2} = \sigma^2(1 \pm |\psi|)$, $\beta = \beta_{1,2}$ and $\gamma = \gamma_{1,2}$ into equations (28) and (29) yields

$$\beta_{1,2} = \pm\frac{\gamma_{1,2}\psi}{|\psi|}, \tag{30}$$
$$\gamma_{1,2} = \pm\frac{\beta_{1,2}\psi^*}{|\psi|}, \tag{31}$$
$$|\beta_{1,2}|^2 = |\gamma_{1,2}|^2. \tag{32}$$

Using the property that $\mathbf{v}$ is a unit vector gives

$$\begin{aligned}\mathbf{v}^H\mathbf{v} = 1 &= (\beta^*\mathbf{a}_1^H + \gamma^*\mathbf{a}_2^H)(\beta\mathbf{a}_1 + \gamma\mathbf{a}_2) \\ &= |\beta|^2 + \beta^*\gamma\psi + \gamma^*\beta\psi^* + |\gamma|^2,\end{aligned} \tag{33}$$

and substituting equations (31) and (32) yields

$$|\beta_{1,2}|^2 = \frac{1}{2(1 \pm |\psi|)}. \tag{34}$$

The phase of either β or γ can be arbitrarily chosen (see equations (30) to (33)). There is also no phase relationship between β_1, γ_1 and β_2, γ_2 as can be seen by expanding $\mathbf{v}_1^H\mathbf{v}_2 = 0$. The phase of $\beta_{1,2}$ is fixed to 0 and thus $\beta_{1,2} = 1/\sqrt{2(1 \pm |\psi|)}$. Substituting equation (31) into equation (27) yields

$$\mathbf{v}_1 = \frac{1}{\sqrt{2(1 + |\psi|)}}\left[\mathbf{a}_1 + \frac{\psi^*}{|\psi|}\mathbf{a}_2\right], \tag{35}$$
$$\mathbf{v}_2 = \frac{1}{\sqrt{2(1 - |\psi|)}}\left[\mathbf{a}_1 - \frac{\psi^*}{|\psi|}\mathbf{a}_2\right]. \tag{36}$$

To construct $\mathbf{v}_2$ from equation (36), the direction of arrival of the RFI (this can be obtained by using algorithms such as MUSIC and ESPRIT) as well as the signal bandwidth are required.

8 Proposed RFI Mitigation Algorithms

Two new spatial RFI mitigation algorithms based on subspace subtraction are presented in this section. These algorithms are designed for non-narrowband RFI that is stationary, such as DAB broadcasts. The channel bandwidth should be selected so that the second eigenvalue, of the sample covariance matrix $\widehat{\mathbf{R}}$, is lower or equal to the power of the cosmic sources being observed and can be computed using equation (25). The first algorithm is based on the flat frequency response model (see equation (11)) and the second on Zatman's approximation to that model (see equation (36)). The following preprocessing steps are required (see figure 4 for an activity diagram of the preprocessing stage):

- Use the power iteration method on $\widehat{\mathbf{R}}$ to find the largest eigenvalue s_1 with the accompanying eigenvector $\mathbf{v}_1$.
- Obtain the location of the RFI source. For example, the location of DAB towers can be easily obtained and used as the initial guess for a fast iterative algorithm such as Minimum Error Convergence [8]. If no initial guess can be made, algorithms such as MUSIC or ESPRIT can be used [9, p. 80-82].

- Estimates for the two largest eigenvalues of the RFI only covariance matrix can be obtained by using the estimated location of the RFI and equation (16)

$$s_{r1} = s_1 - \frac{\mathrm{Tr}(\widehat{\mathbf{R}}) - s_1}{N_e - 1}, \tag{37}$$

$$s_{r2} = s_{r1}\left(\frac{1-|\psi|}{1+|\psi|}\right). \tag{38}$$

Use these two new eigenvalue estimates to create the matrix $\mathbf{S}_r = \mathrm{diag}([s_{r1}, s_{r2}]^T)$.

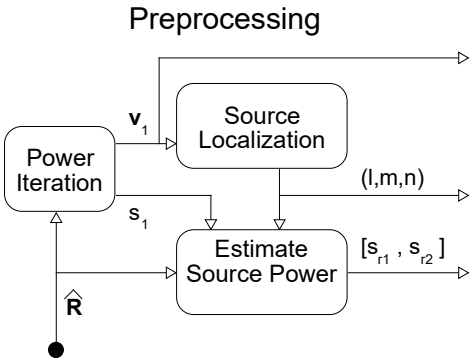

Figure 4. Activity Diagram of Preprocessing stage.

Algorithm 1: Flat frequency response model based algorithm (FF algorithm, see figure 5a for activity diagram)

- Calculate the normalized flat frequency covariance matrix model of the RFI source $\mathbf{R}_f$, using equation (11). Note that this model covariance matrix does not include any noise and that $\sigma_s^2 = 1$.
- Use the power iteration method on $\mathbf{R}_f$ to find the second largest eigenvalue's eigenvector $\mathbf{v}_{2f}$.
- Apply subspace subtraction to obtain the flat frequency model based RFI mitigated covariance matrix

$$\widehat{\mathbf{R}}_{mf} = \widehat{\mathbf{R}} - [\mathbf{v}_1, \mathbf{v}_{2f}]\mathbf{S}_r[\mathbf{v}_1, \mathbf{v}_{2f}]^H. \tag{39}$$

Algorithm 2: Zatman's approximation based algorithm (ZA algorithm, see figure 5b for activity diagram)

- Calculate the normalized Zatman's approximation based model eigenvector $\mathbf{v}_{2z}$ using equation (36).
- Apply subspace subtraction to obtain the Zatman's approximation model based RFI mitigated covariance matrix

$$\widehat{\mathbf{R}}_{mz} = \widehat{\mathbf{R}} - [\mathbf{v}_1, \mathbf{v}_{2z}]\mathbf{S}_r[\mathbf{v}_1, \mathbf{v}_{2z}]^H. \tag{40}$$

9 Evaluation of RFI Mitigation Algorithms

To evaluate the performance of both proposed algorithms, an estimated covariance matrix was created by adding an estimated noise and cosmic source covariance matrix $\widehat{\mathbf{R}}_{nc}$ to an estimated RFI covariance matrix $\widehat{\mathbf{R}}_r$. The matrix $\widehat{\mathbf{R}}_{nc}$ was obtained from a real observation done with LOFAR HBA station RS407 where there is no RFI present. A software defined radio was used to record a DAB signal with the power spectrum shown in figure 6a and has a reasonably flat frequency spectrum. Finite impulse response filters were used to produce 70 signals with bandwidths ranging from 763 Hz to 195 kHz (typical values for LOFAR). Each filtered signal was used to generate a delayed signal for each antenna in the array. The delay was added by computing the fast Fourier transform of the filtered signal and multiplying each frequency component with the appropriate delay and then computing the inverse fast Fourier transform. For each bandwidth a $\widehat{\mathbf{R}}_r$ covariance matrix was created by correlating the delayed signals for 1.5 s.

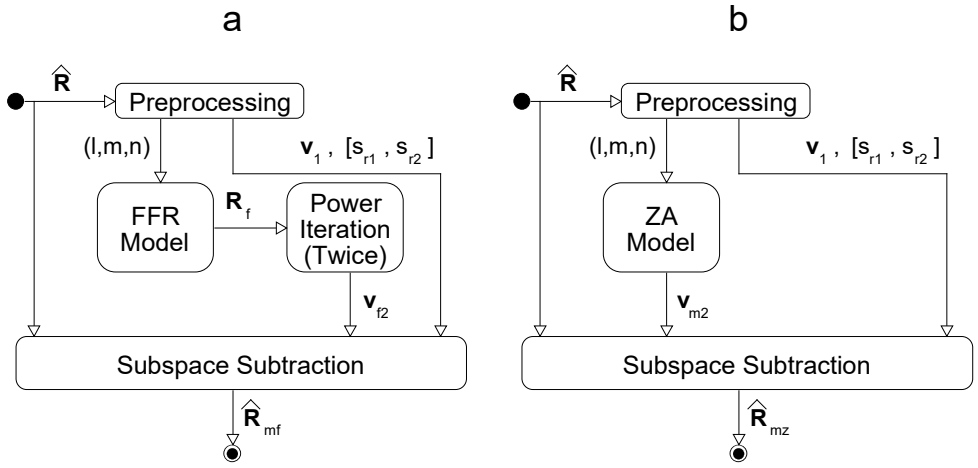

Figure 5. **(a)** Activity diagram for algorithm 1 which uses the flat frequency model in equation (11). **(b)** Activity diagram for algorithm 2 which uses the Zatman's approximation in equation (36).

To measure the performance of the proposed algorithms, the Frobenius norm of the difference between the recovered covariance matrix $\widehat{\mathbf{R}}_{\mathrm{m}}$ and matrix $\widehat{\mathbf{R}}_{\mathrm{nc}}$ is calculated

$$\mathrm{FN} = \sqrt{\sum_{j=1}^{N_{\mathrm{e}}} \sum_{k=1}^{N_{\mathrm{e}}} \left| \widehat{\mathbf{R}}_{\mathrm{nc},jk} - \widehat{\mathbf{R}}_{\mathrm{m},jk} \right|^2} \tag{41}$$

In figure 6b, a plot is given of the Frobenius norm as a function of fractional bandwidth. The difference in performance of the FF and the ZA algorithms is less than 10^{-13} and both are represented by the proposed 2nd order line. The 1st order line is the performance achieved by using single frequency subspace subtraction. Close to zero fractional bandwidth, the performance of the 1st order method and that of the 2nd order methods is the same. As the bandwidth increases, so does the Frobenius norm for the 1st order method, since the second eigenvalue becomes significant, however the FN for the 2nd order methods shows very little increase. The minimum achievable FN is 6.7×10^{-3} and is due to the estimation errors in $\mathbf{v}_1$ and s_{r1}. Channels with larger bandwidth can be processed using the 2nd order methods, while achieving the same level of mitigation as the 1st order method, which requires channels with smaller bandwidth. This is shown in figure 6c where the bandwidth required by the 2nd order methods is given as a function of the bandwidth of the 1st order method. Using a fitted straight line indicates an increase by approximately a factor six in bandwidth that can be processed.

The FF algorithm and the ZA algorithm have the same performance for the bandwidths selected. Both algorithms have computational complexity $\mathcal{O}(N_{\mathrm{e}}^2)$ (which includes the preprocessing step making use of the Minimum Error Convergence algorithm). However, the FF algorithm requires an additional calculation of an eigenvector and the computational complexity of the FF algorithm's equation (11) is $\mathcal{O}(N_{\mathrm{e}}^2)$ compared to the ZA algorithm's equation (36) which has computational complexity $\mathcal{O}(N_{\mathrm{e}})$. The quadratic growth of computational time as a function of the number of antennas is shown in figure 6d. The ZA algorithm achieved a median speed-up of 1.3.

10 Conclusion

Strong non-narrowband RFI cannot be modelled as a single point source, but rather as an infinite sum of sources that rapidly decrease in power. For traditional spatial filtering to work on powerful non-narrowband RFI, it must be filtered into frequency channels which are sufficiently narrow so that for each frequency channel, the RFI source is a single point source. This greatly increases the computational cost. To reduce this cost, the FF and ZA algorithms are presented that combine a non-narrowband signal model with a subspace subtraction method and, in so doing, decreases the number of frequency channels that must be processed. The proposed algorithms are able to process approximately six times more bandwidth than conventional spatial filtering methods. For bandwidths between 763 Hz and 195 kHz and a LOFAR HBA station layout, the performance of the proposed methods is similar. However, the ZA algorithm showed a speed-up of 1.3 relative to the FF algorithm.

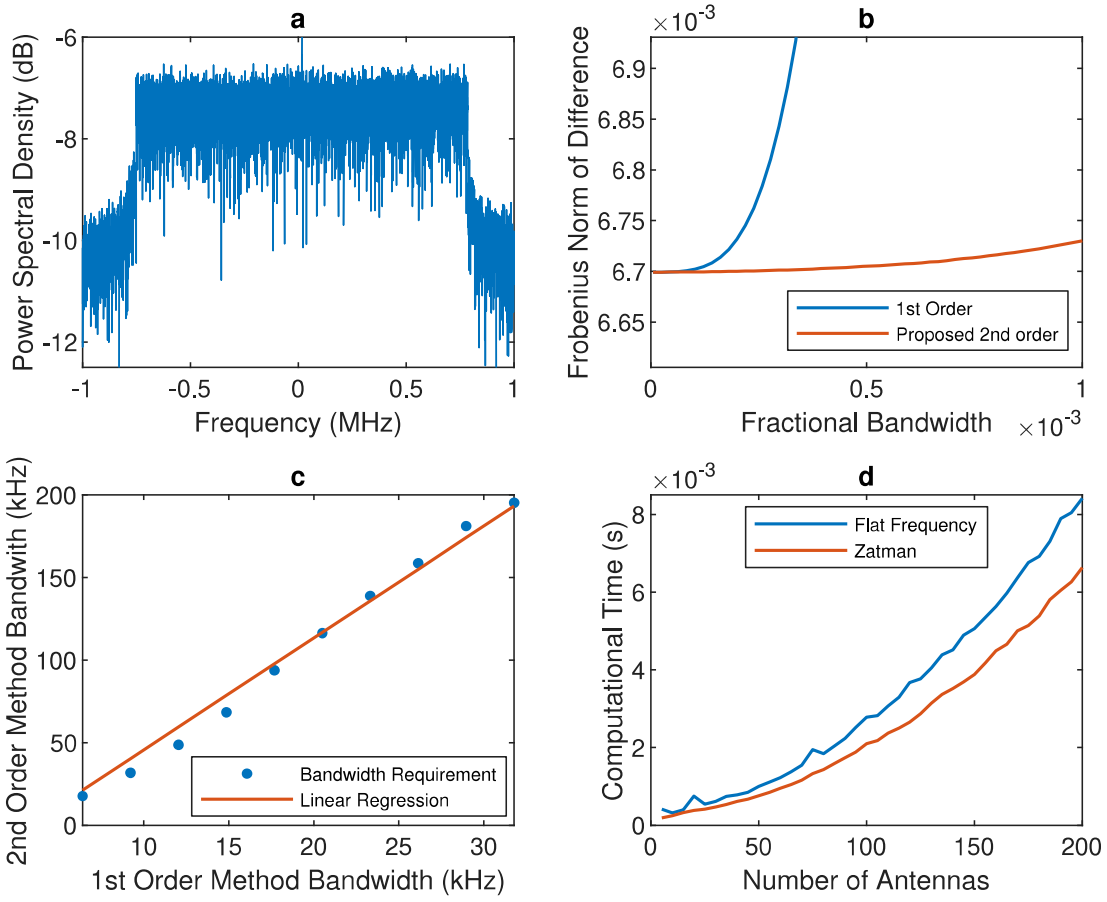

Figure 6. **(a)** Power spectrum of a DAB signal measured with a software defined radio. **(b)** Frobenius norm of the difference between the recovered matrices using RFI mitigation methods and the noise and cosmic source covariance matrix as a function of fractional bandwidth. The 1st order mitigation method makes use of single frequency subspace subtraction. The performance of the FF algorithm and the ZA algorithm are within 10^{-13} of each other and are both represented by the proposed 2nd order line. **(c)** A plot of the bandwidth of the 2nd order methods as a function of the bandwith of the 1st order method to achieve the same attenuation. **(d)** The computational time of both proposed mitigation algorithms as a function of the number of antennas.

11 Acknowledgements

This work is funded and supported by the South Africa Radio Astronomy Observatory, IBM, ASTRON, the Dutch Ministry of Economic Affairs and the Province of Drenthe, the South African Research Chairs Initiative of the Department of Science and Technology, the National Research Foundation of South Africa, and the Netherlands Organisation for Scientific Research.

References

[1] S. van der Tol, and A. van der Veen, "Performance Analysis of Spatial Filtering of RF Interference in Radio Astronomy," *IEEE Transactions on Signal Processing*, **53**, 3, February 2005, pp. 896–910, doi:10.1109/TSP.2004.842177.

[2] A. van der Veen, A. Leshem, and A. Boonstra, "Signal Processing for Radio Astronomical Arrays," *Proceedings of the Sensor Array and Multichannel Signal Processing Workshop*, July 2004, pp. 1–10, doi:10.1109/SAM.2004.1502901.

[3] A. J. Boonstra, "Radio Frequency Interference Mitigation in Radio Astronomy," *PhD Thesis, Delft University of Technology*, June 2005, uuid:caa1942c-4180-4a17-88db-cec359490aad.

[4] M. P. van Haarlem, et al., "LOFAR: The Low Frequency Array," *Astronomy & Astrophysics*, **556**, A2, August 2013, pp. 1–53, doi:10.1051/0004-6361/201220873.

[5] A. H. Bridle, and F. R. Schwab, "Bandwidth and Time-Average Smearing," in G. B. Taylor, C. L. Carilli and R. A. Perley (eds), *Synthesis Imaging in Radio Astronomy II*, **180**, 18, 1999, pp. 371–382, eISBN: 978-1-58381-516-8.

[6] M. Zatman, "How narrow is narrowband?," *IEE Proceedings-Radar, Sonar and Navigation*, **145**, 2, April 1998, pp. 85–91, doi:10.1049/ip-rsn:19981670.

[7] D. H. Johnson, and D. E. Dudgeon, *Array Signal Processing: Concepts and Techniques*, NJ: Prentice-Hall, 1993, pp. 113-115.

[8] J. W. Steeb, D. B. Davidson, and S. J. Wijnholds, "Computationally efficient near-field radio frequency source localisation," *2017 XXXIInd General Assembly and Scientific Symposium of the International Union of Radio Science (URSI GASS)*, August 2017, pp. 1–4, doi: 10.23919/URSIGASS.2017.8104498.

[9] C. A. Balanis, and P. I. Ioannides, *Introduction to Smart Antennas*, Morgan & Claypool Publishers, 2007, pp. 80-82.

2.6 Journal Paper - Mitigation of Non-Narrowband Radio Frequency Interference Incorporating Array Imperfections

Journal of Astronomical Instrumentation

Mitigation of Non-Narrowband Radio Frequency Interference Incorporating Array Imperfections

Jan-Willem W. Steeb[1,4], David B. Davidson[2,1] and Stefan J. Wijnholds[3,1]
[1] *Department of Electrical & Electronic Engineering, Stellenbosch University, South Africa*
[2] *International Centre for Radio Astronomy Research (ICRAR), Curtin University, Australia*
[3] *Netherlands Institute for Radio Astronomy (ASTRON), The Netherlands*

Received (to be inserted by publisher); Revised (to be inserted by publisher); Accepted (to be inserted by publisher);

In this paper we extend a non-narrowband spatial radio frequency interference (RFI) mitigation algorithm for radio astronomy arrays to include a calibration step. The algorithm constructs a second order filter by combining a first order subspace subtraction method with a non-narrowband signal model. The model is based on the assumption that the frequency response is approximately flat. In addition, an approximation of this model is presented that makes use of two frequency-shifted monochromatic sources. Array imperfections such as unknown complex gains and mutual coupling are also considered and incorporated into the non-narrowband signal models. Using the approximation of the flat frequency model, it is shown that gain calibration can be applied to improve performance. With a gain calibration step and no mutual coupling, the proposed algorithm was able to process twice the bandwidth per channel when compared to conventional narrowband techniques. This performance declines to 1.6 times more bandwidth when the effect of mutual coupling is included. The evaluation of the algorithm was done using the layout of a LOFAR High Band Antenna (HBA) station and a digital audio broadcast recorded with a software defined radio.

Keywords: RFI Mitigation, Non-narrowband, Complex Gain Calibration, Mutual Coupling.

1. Introduction

Radio astronomy as a passive service competes with the telecommunication industry for radio spectrum (3 Hz to 3 THz). For example, the Low Frequency Array (LOFAR) (van Haarlem *et al.* , 2013) operates from 10 to 240 MHz and overlaps with the digital audio broadcasting (DAB) band (174 to 228 MHz) in the Netherlands. In figure 1 a plot of the power spectral density for a LOFAR antenna shows a DAB signal that is present from 182.9 MHz to 184.4 MHz and is approximately 100 dB above the noise.

When a non-narrowband signal is received by an interferometric array and the visibilities are imaged it will appear as an extended source. This phenomena is called frequency smearing (Bridle & Schwab , 1999). In this paper we address how to model this smearing if it is assumed that the frequency response of the signal is relatively flat. Furthermore, we discuss an approximation of this model which makes use of two frequency-shifted narrowband point sources.

Most radio frequency interference (RFI) that is detected by radio astronomy arrays comprises non-narrowband signals. If the channel bandwidth of the array is sufficiently narrow, then the effects of frequency smearing will be minimal. These effectively narrowband RFI sources can be removed by using spatial RFI mitigation techniques such as orthogonal projection, orthogonal projection with subspace bias correction, oblique projection and subspace subtraction (van der Tol & van der Veen , 2005; van der Veen *et al.*, 2004; Boonstra , 2005). However, if the power of the RFI signal is far above that of the astronomical sources, then it is still possible for the frequency smearing to affect the image after a spatial RFI mitigation technique has been applied. For example, in figure 2a a simulated skymap is given of a non-narrowband RFI source with a bandwidth of 195 kHz and a center frequency of 145 MHz. For the simulation the layout of a LOFAR

[4]Corresponding author.

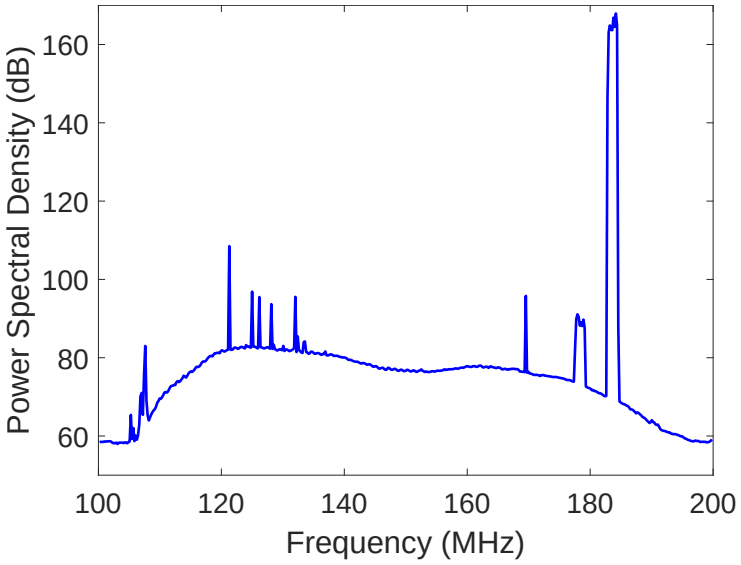

Fig. 1. Power spectral density for a LOFAR High Band Antenna (HBA) in the RS409 station. The DAB signal is clearly visible from 182.9 MHz to 184.4 MHz.

High Band Antenna (HBA) station is used. From the image it appears that the source is a narrowband point source; however, when a first order orthogonal projector is applied, this results in two sources which are separated along the radial direction (see figure 2b). These two sources are not real physical sources, but are caused by frequency smearing and in this case lie 40 dB below the RFI source. If the power of the astronomical sources are also in the region of -40 dB, then the effect of the RFI source cannot be fully mitigated using standard spatial RFI techniques.

The effect of array imperfections, such as unknown complex gains as well as mutual coupling, on non-narrowband signals is also considered. In figure 2c a skymap shows how unknown complex gains can distort the structure of the frequency smearing component. The mutual coupling effect is considerably more subtle for this simulation and in figure 2d only the side lobes are slightly distorted. The impact of mutual coupling will in general depend on the array elements and layout, as well as operating frequency.

Finally, algorithms will be presented in this paper that are able to mitigate these non-narrowband RFI signals and also take into account direction independent effects.

2. Notation

$\mathbf{A}$	Bold upper-case letters are matrices. The jk^{th} element is indicated by $\mathbf{A}_{jk}$.
$\mathbf{a}$	Bold lower-case letters are column vectors. The j^{th} element is indicated by $\mathbf{a}_j$.
$\mathbf{I}$	Identity matrix.
$\odot$	Hadamard product.
$\ominus$	Element-wise division.
$\lvert\cdot\rvert$	Absolute value of a scalar.
$\text{Tr}(\cdot)$	Trace of a matrix.
$\text{diag}(\cdot)$	Converts a vector into a diagonal matrix.
$\angle$	Phase of a complex number.
i	Square root of -1.
c	Speed of light.
$\{\cdot\}^H$	Hermitian transpose of a matrix.
$\{\cdot\}^T$	Transpose of a matrix.
$\{\cdot\}^*$	Complex conjugate of a scalar.
$\text{sinc}(x)$	$= \sin(\pi x)/(\pi x)$, normalized sinc function.
$\lVert\cdot\rVert_F$	Frobenius norm of a matrix.
$\lvert\cdot\rvert_\odot$	Element-wise absolute value of a matrix.

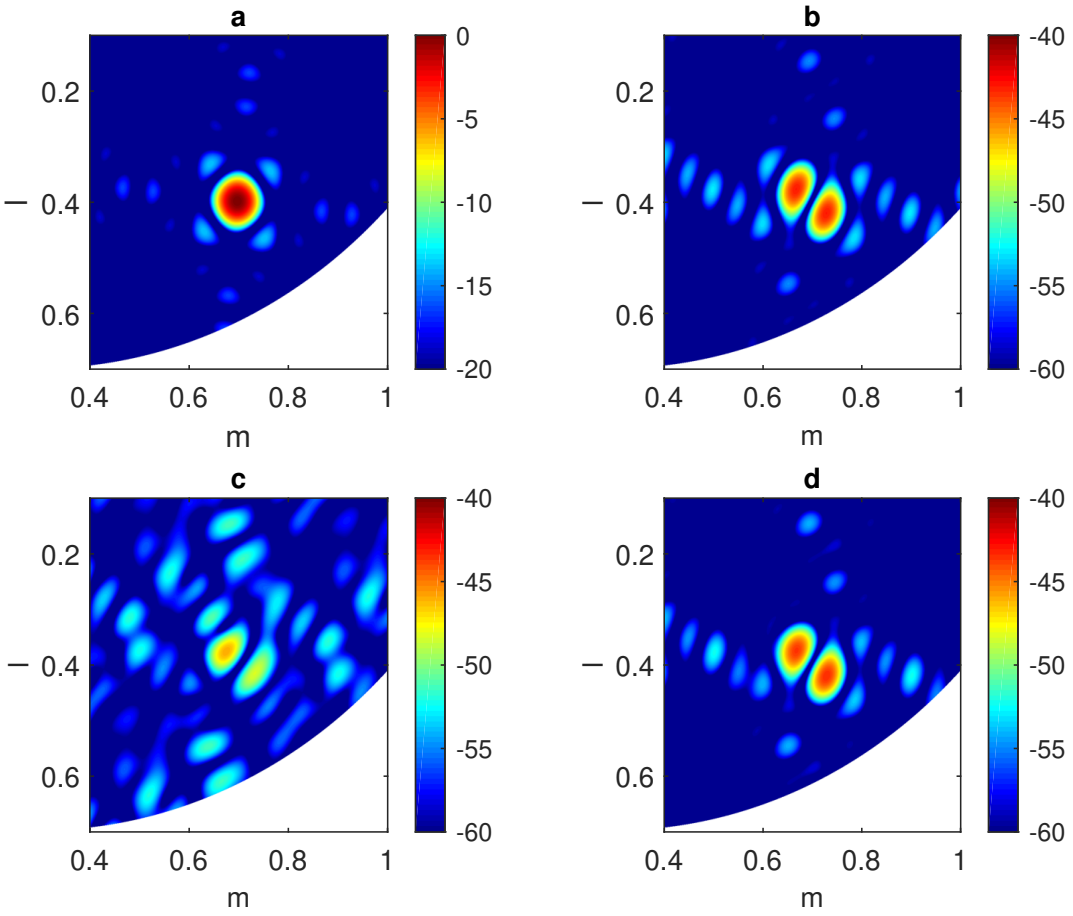

Fig. 2. **(a)** Skymap with non-narrowband RFI source in dB (the RFI source is the 0 dB point). The source has a bandwidth of 195 kHz and a center frequency of 145 MHz. **(b)** Skymap with non-narrowband RFI source removed using a first order orthogonal projection filter. Two weaker sources adjacent to the location of the RFI are now visible and are caused by the bandwidth of the RFI source. **(c)** Skymap with non-narrowband RFI source affected by unknown complex gains, removed using a first order orthogonal projection filter. The unknown complex gains distort the residual sources caused by the bandwidth. **(d)** Skymap with non-narrowband RFI source affected by mutual coupling, removed using a first order orthogonal projection filter. In this case, the mutual coupling slightly distorts the sidelobes of the residual sources caused by the bandwidth.

3. Signal Models

The standard narrowband signal model assumes that the received signal is monochromatic. In the flat frequency model, the narrowband signal model is adapted to be frequency dependant and have a uniform power spectral density. The Zatman's approximation based model approximates the flat frequency model using two monochromatic sources.

3.1. *Narrowband Signal Model*

If perfectly calibrated omnidirectional antennas are used, then the normalized array response vector for an array with N_e elements and a continuous wave source with frequency ν is given by

$$\mathbf{a} = \begin{bmatrix} b_1 e^{-\mathrm{i}2\pi\nu\tau_1} \\ \vdots \\ b_{N_\mathrm{e}} e^{-\mathrm{i}2\pi\nu\tau_{N_\mathrm{e}}} \end{bmatrix}. \tag{1}$$

If the source lies in the far-field, then the geometrical delays and normalization constants are

$$\tau_j = -(l_{\rm s}x_{_j} + m_{\rm s}y_{_j} + n_{\rm s}z_{_j})/c, \tag{2}$$

$$b_j = 1/\sqrt{N_{\rm e}}, \tag{3}$$

where x_j, y_j, z_j are the Cartesian coordinates of the j^{th} antenna and $l_{\rm s}, m_{\rm s}, n_{\rm s}$ are the directional cosines of the source. The array covariance matrix for a single source without noise is given by

$$\mathbf{R} = \sigma_{\rm s}^2 \mathbf{a}\mathbf{a}^H, \tag{4}$$

$$\mathbf{R}_{jk} = \sigma_{\rm s}^2 b_j b_k e^{-{\rm i}2\pi\tau_{jk}\nu}, \tag{5}$$

where $\sigma_{\rm s}^2$ is the signal power, $\mathbf{R}_{jk}$ is the $jk^{\rm th}$ element in the covariance matrix and $\tau_{jk} = \tau_j - \tau_k$.

All examples in this paper make use of sources in the far-field. However, any of the presented methods can be used for near-field sources by setting $\tau_j = r_{_{sj}}/c$ and $b_j = 1/\left[r_{sj}\sqrt{\sum_{n=1}^{N_{\rm e}} 1/r_{sn}^2}\right]$, where the distance between the j^{th} antenna and the source is denoted by r_{sj} (Johnson & Dudgeon , 1993).

3.2. *Flat Frequency Model*

For a non-narrowband signal, the total covariance response is obtained by integrating over the entire signal bandwidth $\Delta\nu$

$$\mathbf{R} = \frac{1}{\Delta\nu}\int_{\nu_0-\Delta\nu/2}^{\nu_0+\Delta\nu/2} \sigma_{\rm s}^2(\nu)\mathbf{a}(\nu)\mathbf{a}^H(\nu)d\nu. \tag{6}$$

If the spectrum of the signal is flat, $\sigma_s^2 = \sigma_s^2(\nu)$, then the $jk^{\rm th}$ element of the covariance matrix is given by

$$\mathbf{R}_{jk} = \frac{\sigma_{\rm s}^2 b_j b_k}{\Delta\nu}\int_{\nu_0-\Delta\nu/2}^{\nu_0+\Delta\nu/2} e^{-{\rm i}2\pi\tau_{jk}\nu}d\nu = \sigma_{\rm s}^2 b_j b_k \underbrace{\rm sinc(\tau_{jk}\Delta\nu)}_{\text{Decorrelating Function}} e^{-{\rm i}2\pi\tau_{jk}\nu_0}. \tag{7}$$

The difference between the single frequency model in Eq. (5) and the flat frequency model in Eq. (7) is $\rm sinc(\tau_{jk}\Delta\nu)$, which causes $\mathbf{R}_{jk}$ to decorrelate as the bandwidth of the signal increases.

3.3. *Zatman's Approximation Based Model*

In the approximation of the flat frequency model proposed by Zatman (1998) two equal power sources that are frequency-shifted by $\kappa = \Delta\nu/(2\sqrt{3})$, are used

$$\mathbf{R} \approx \sigma^2\mathbf{a}(\nu_0+\kappa)\mathbf{a}^H(\nu_0+\kappa) + \sigma^2\mathbf{a}(\nu_0-\kappa)\mathbf{a}^H(\nu_0-\kappa) = \sigma^2(\mathbf{a}_1\mathbf{a}_1^H + \mathbf{a}_2\mathbf{a}_2^H), \tag{8}$$

where $\sigma^2 = 0.5\sigma_{\rm s}^2$. Representing the two signals as Dirac deltas and integrating yields the total covariance matrix

$$\begin{aligned}\mathbf{R}_{jk} &\approx \frac{\sigma_{\rm s}^2 b_j b_k}{2}\left[\int_{-\infty}^{\infty}\delta(\nu-\nu_0+\kappa)e^{-{\rm i}2\pi\tau_{jk}\nu}d\nu + \int_{-\infty}^{\infty}\delta(\nu-\nu_0-\kappa)e^{-{\rm i}2\pi\tau_{jk}\nu}d\nu\right] \\ &= \sigma_{\rm s}^2 b_j b_k \underbrace{\cos\left(\pi\tau_{jk}\Delta\nu/\sqrt{3}\right)}_{\text{Decorrelating Function}} e^{-i2\pi\tau_{jk}\nu_0}.\end{aligned} \tag{9}$$

The only difference between the flat frequency model and the Zatman's approximation is the decorrelating function (see Eq. (7) and (9)). The error between the two decorrelating functions is small for the peak around $\Delta\nu = 0$. This is shown in figure 3 using LOFAR HBA station RS407 in a simulation with a center frequency of 145 MHz and varying the signal bandwidth between 0 and 2 MHz for both models. In figures 3a and b the percentage difference between the eigenvalues and one minus the cosine similarity between the eigenvectors are respectively given between the flat frequency model and the Zatman's approximation based model as a function of fractional bandwidth. The cosine similarity is the cosine of the angle between

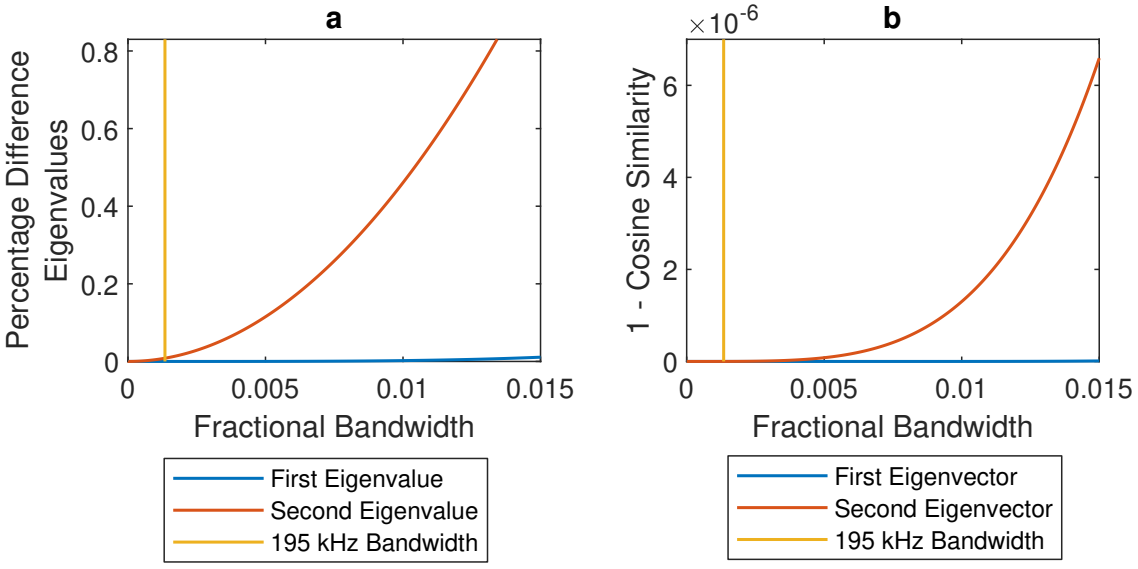

Fig. 3. Results from simulation using LOFAR HBA station RS407 at a center frequency of 145 MHz. **(a)** Percentage difference between the corresponding eigenvalues of the flat frequency model and the Zatman's approximation based model. **(b)** One minus the cosine similarity between the corresponding eigenvectors of the flat frequency model and the Zatman's approximation based model as a function of fractional bandwidth. A score of zero indicates that the eigenvectors are parallel.

two vectors. These plots clearly show that there is minimal error between the models even if the typical channel bandwidth of 195 kHz is increased tenfold.

The covariance matrix for the Zatman's approximation $\mathbf{R}_{\mathrm{z}}$ can be written in terms of its eigenvalue decomposition

$$\mathbf{R}_{\mathrm{z}} = \lambda_1 \mathbf{v}_1 \mathbf{v}_1^H + \lambda_2 \mathbf{v}_2 \mathbf{v}_2^H, \tag{10}$$

where λ_1 and λ_2 are the largest and second largest eigenvalues and $\mathbf{v}_1$ and $\mathbf{v}_2$ are the corresponding eigenvectors. Both the eigenvectors and eigenvalues can be written in terms of the Zatman's approximation sources' power σ^2 and array response vectors $\mathbf{a}_1$ and $\mathbf{a}_2$

$$\lambda_{1,2} = \sigma^2[1 \pm |\psi|], \tag{11}$$

$$\psi = \mathbf{a}_1^H \mathbf{a}_2 = \frac{1}{N_{\mathrm{e}}} \sum_{p=1}^{N_{\mathrm{e}}} e^{i4\pi\kappa\tau_p}, \tag{12}$$

$$\mathbf{v}_{1,2} = \frac{1}{\sqrt{2(1 \pm |\psi|)}} \left[\mathbf{a}_1 \pm \frac{\psi^*}{|\psi|} \mathbf{a}_2 \right]. \tag{13}$$

A detailed derivation of these equations can be found in Steeb *et al.* (2018). The covariance matrix for each subspace is then given by

$$\mathbf{R}_1 = \mathbf{v}_1 \mathbf{v}_1^H = \frac{1}{2(1 + |\psi|)} \left[\mathbf{a}_1 \mathbf{a}_1^H + \frac{\psi^*}{|\psi|} \mathbf{a}_2 \mathbf{a}_1^H + \frac{\psi}{|\psi|} \mathbf{a}_1 \mathbf{a}_2^H + \mathbf{a}_2 \mathbf{a}_2^H \right], \tag{14}$$

$$\mathbf{R}_2 = \mathbf{v}_2 \mathbf{v}_2^H = \frac{1}{2(1 - |\psi|)} \left[\mathbf{a}_1 \mathbf{a}_1^H - \frac{\psi^*}{|\psi|} \mathbf{a}_2 \mathbf{a}_1^H - \frac{\psi}{|\psi|} \mathbf{a}_1 \mathbf{a}_2^H + \mathbf{a}_2 \mathbf{a}_2^H \right]. \tag{15}$$

Expanding the jk^{th} element for each matrix, using $(\mathbf{a}_1)_j = e^{-i2\pi(\nu_0+\kappa)\tau_j}/\sqrt{N_{\mathrm{e}}}$, $(\mathbf{a}_2)_j = e^{-i2\pi(\nu_0-\kappa)\tau_j}/\sqrt{N_{\mathrm{e}}}$

and $\psi = \mathbf{a}_1^H \mathbf{a}_2 = 1/N_\mathrm{e} \sum_{p=1}^{N_\mathrm{e}} e^{i4\pi\kappa\tau_p}$, yields

$$
\begin{aligned}
(\mathbf{R}_1)_{jk} &= \frac{1}{2(1+|\psi|)} \left[e^{-i2\pi\kappa\tau_{jk}} + \frac{\psi^*}{|\psi|} e^{i2\pi\kappa(\tau_j+\tau_k)} + \frac{\psi}{|\psi|} e^{-i2\pi\kappa(\tau_j+\tau_k)} + e^{i2\pi\kappa\tau_{jk}} \right] \frac{e^{-i2\pi\nu_0\tau_{jk}}}{N_\mathrm{e}} \\
&= \underbrace{\frac{1}{(1+|\psi|)} \left[\cos(2\pi\kappa\tau_{jk}) + \frac{1}{N_\mathrm{e}|\psi|} \sum_{p=1}^{N_\mathrm{e}} \cos(2\pi\kappa(\tau_{pj}+\tau_{pk})) \right]}_{\text{Positive Real Value if } 2\pi\kappa\tau_{jk}<\pi/2 \text{ and } 2\pi\kappa(\tau_{pj}+\tau_{pk})<\pi/2} \underbrace{\frac{e^{-i2\pi\nu_0\tau_{jk}}}{N_\mathrm{e}}}_{\text{Point Source Model}}, \qquad (16)
\end{aligned}
$$

$$
\begin{aligned}
(\mathbf{R}_2)_{jk} &= \frac{1}{2(1-|\psi|)} \left[e^{-i2\pi\kappa\tau_{jk}} - \frac{\psi^*}{|\psi|} e^{i2\pi\kappa(\tau_j-\tau_k)} - \frac{\psi}{|\psi|} e^{-i2\pi\kappa(\tau_j+\tau_k)} + e^{i2\pi\kappa\tau_{jk}} \right] \frac{e^{-i2\pi\nu_0\tau_{jk}}}{N_\mathrm{e}} \\
&= \underbrace{\frac{1}{(1-|\psi|)} \left[\cos(2\pi\kappa\tau_{jk}) - \frac{1}{N_\mathrm{e}|\psi|} \sum_{p=1}^{N_\mathrm{e}} \cos(2\pi\kappa(\tau_{pj}+\tau_{pk})) \right]}_{\text{Real Value}} \underbrace{\frac{e^{-i2\pi\nu_0\tau_{jk}}}{N_\mathrm{e}}}_{\text{Point Source Model}}. \qquad (17)
\end{aligned}
$$

For both $(\mathbf{R}_1)_{jk}$ and $(\mathbf{R}_2)_{jk}$ the complex exponential part is the narrowband point source model for the signal. The real part of $(\mathbf{R}_1)_{jk}$ is positive, therefore the phase of the point source is not changed and its structure is maintained (see figure 2a). For $(\mathbf{R}_2)_{jk}$ the real part can be negative, which causes a π phase shift. This phase shift, in some of the elements, in $\mathbf{R}_2$ causes the single point source structure to change to two adjacent sources (see figure 2b).

4. Unknown Complex Gain Model

In section 3.1 the assumption was made that there are no array imperfections or external effects on the signal. However, in reality signals are affected by direction dependent effects such as path loss, the polarization mismatch factor, the gain of the antennas and atmospheric effects. Furthermore, direction independent effects include the receiver electronics, in particular the low noise amplifiers. Direction independent and dependant effects can be combined into one unknown complex gain per antenna if only one non-narrowband RFI signal is assumed to be impinging on the array for a given band of the spectrum.

The Zatman's model will now be expanded to include unknown complex gains, $\mathbf{g} = [g_1 \dots g_{N_\mathrm{e}}]^T$. The two discrete signals from Eq. (8) are now given by

$$\mathbf{a}_{1\mathrm{g}} = \sqrt{N_\mathrm{e}}(\mathbf{a}_1 \odot \mathbf{g}), \qquad (18)$$

$$\mathbf{a}_{2\mathrm{g}} = \sqrt{N_\mathrm{e}}(\mathbf{a}_2 \odot \mathbf{g}). \qquad (19)$$

The complex gain vector $\mathbf{g}$ is defined as normalized and the inverse of the normalization factor is absorbed into the signal's eigenvalues (the ratio between the eigenvalues remains the same). Since the array response vectors $\mathbf{a}_{1,2}$ represent plane waves (where each element is a phasor multiplied by $1/\sqrt{N_\mathrm{e}}$) the factor $\sqrt{N_\mathrm{e}}$ is introduced to normalize both $\mathbf{a}_{1\mathrm{g}}$ and $\mathbf{a}_{2\mathrm{g}}$ in Eq. (18) and (19).

Eq. (11) which describes the relationship between the signal's power and eigenvalues, is then given by

$$\lambda_{1g,2g} = \sigma_g^2[1 \pm |\psi_g|], \qquad (20)$$

where $\psi_g = \mathbf{a}_{1\mathrm{g}}^H \mathbf{a}_{2\mathrm{g}} = \sum_{p=1}^{N_\mathrm{e}} |g_p|^2 e^{i4\pi\kappa\tau_p}$ and σ_g^2 is the signal's power multiplied by the inverse of the normalization factor. The normalized covariance matrix for the first subspace (see Eq. (14)), including the effect of $\mathbf{g}$, can be expressed as

$$
\begin{aligned}
\mathbf{R}_{1\mathrm{g}} = \mathbf{v}_{1\mathrm{g}}\mathbf{v}_{1\mathrm{g}}^H &= \frac{1}{2(1+|\psi_\mathrm{g}|)} \left[\mathbf{a}_{1\mathrm{g}}\mathbf{a}_{1\mathrm{g}}^H + \frac{\psi_\mathrm{g}^*}{|\psi_\mathrm{g}|}\mathbf{a}_{2\mathrm{g}}\mathbf{a}_{1\mathrm{g}}^H + \frac{\psi_\mathrm{g}}{|\psi_\mathrm{g}|}\mathbf{a}_{1\mathrm{g}}\mathbf{a}_{2\mathrm{g}}^H + \mathbf{a}_{2\mathrm{g}}\mathbf{a}_{2\mathrm{g}}^H \right] \\
&= \frac{N_\mathrm{e}}{2(1+|\psi_\mathrm{g}|)} \left[\mathbf{a}_1\mathbf{a}_1^H + \frac{\psi_\mathrm{g}^*}{|\psi_\mathrm{g}|}\mathbf{a}_2\mathbf{a}_1^H + \frac{\psi_\mathrm{g}}{|\psi_\mathrm{g}|}\mathbf{a}_1\mathbf{a}_2^H + \mathbf{a}_2\mathbf{a}_2^H \right] \odot \mathbf{g}\mathbf{g}^H, \qquad (21)
\end{aligned}
$$

where

$$(\mathbf{R}_{1\mathrm{g}})_{jk} = \underbrace{\frac{N_\mathrm{e}}{(1+|\psi_g|)}\left[\cos(2\pi\kappa\tau_{jk}) + \frac{1}{N_\mathrm{e}|\psi_g|}\sum_{p=1}^{N_\mathrm{e}}|g_p|^2\cos(2\pi\kappa(\tau_{pj}+\tau_{pk}))\right]}_{\text{Complex Gain Distorted Non-Narrowband Component}} \underbrace{g_j g_k^H}_{\text{Complex Gain}} \underbrace{\frac{e^{-i2\pi\nu_0\tau_{jk}}}{N_\mathrm{e}}}_{\text{Point Source Model}} . \quad (22)$$

The first component of $(\mathbf{R}_{1\mathrm{g}})_{jk}$ is caused by the non-narrowband nature of the signal and is distorted by the complex gains, since ψ is replaced by ψ_g. Furthermore, the complex gain distorted non-narrowband component is still real valued like the undistorted non-narrowband component (see Eq. (16)). The other two components form the model for a point source that is distorted by complex gains.

To explore the effect of the complex gains on the non-narrowband factor in $(\mathbf{R}_{1\mathrm{g}})_{jk}$, a simulation was done using the layout of LOFAR HBA station RS407 with a channel bandwidth of 195 kHz and an RFI source at the horizon. To calculate $\mathbf{g}$, a normal distribution was used to generate phases and a uniform distribution was used to generate amplitudes. Different distributions are used to reflect the distinct physical effects that lead to amplitude gains and phase errors (Brossard *et al.*, 2018; de Gasperin *et al.*, 2018). Furthermore, the uniform distribution used ensured that the generated amplitudes are positive. The normal distribution used had mean 0 and the standard deviation was varied between 0 and $\pi/3$ radians. At the final standard deviation of $\pi/3$, 99.73 % of the values lie within a π-rad band around the mean. The uniform distribution used had an upper bound fixed at 1 and the lower bound was varied from 1 to 0.0001, giving a standard deviation ranging from 0 to 0.29. The normal and uniform distributions were paired according to increasing standard deviation and for each pair 1000 realizations for each antenna were generated. Figure 4a shows plots of $1-|\psi_g|$ where the maximum and minimum values for $|\psi_g|$ were found for the 1000 realizations as a function of the distributions' standard deviations. Even in the worst case, the distorted $|\psi_g|$ deviates only by 0.004 %. The largest percentage error simulated for the non-narrowband factor (see Eq. (22)) for each element in the covariance matrix is plotted in figure 4b. This plot was obtained by fixing the standard deviation of the normal distribution and uniform distribution to $\pi/3$ and 0.29, respectively. For the 1000 realizations used, the largest error for each element in the covariance matrix was selected for the plot. The pattern obtained is a function of the position of the RFI source. The maximum error in the plot is only 0.006 %. Therefore, for the LOFAR HBA case, the non-narrowband factor is minimally affected by the complex gains and the complex gains can be recovered by using $\mathbf{g}\mathbf{g}^H \approx \mathbf{R}_{1g} \ominus \mathbf{R}_1$ or calibration algorithms such as StEFCal (Salvini & Wijnholds , 2014).

Once the complex gains $\mathbf{g}$ have been recovered, the flat frequency model in Eq. (7) can be updated to include its effect

$$(\mathbf{R}_g)_{jk} = \frac{\sigma_\mathrm{s}^2 g_j g_k}{N_\mathrm{e}}\,\mathrm{sinc}(\tau_{jk}\Delta\nu)e^{-\mathrm{i}2\pi\tau_{jk}\nu_0}. \quad (23)$$

The Zatman's approximation in Eq. (13) can also be updated to

$$\mathbf{v}_{1g} = \frac{1}{\sqrt{2(1\pm|\psi_g|)}}\left[\mathbf{a}_{1g} \pm \frac{\psi_g^*}{|\psi_g|}\mathbf{a}_{2g}\right]. \quad (24)$$

5. Mutual Coupling Model

The mutual coupling in the array cannot be modelled by complex gains, since the signal in each antenna is a weighted sum of the signals in all other antennas. Doing a full electromagnetic simulation of a LOFAR HBA is computationally expensive. Therefore, the multiple input multiple output model developed in Wijnholds (2008) is used to find qualitative results. The model assumes that the signals are narrowband and that the antennas are dipoles.

The mutual coupling matrix $\mathbf{M}$ is calculated in two steps. The first is to calculate $\mathbf{M}_0$ which describes how initially each antenna signal is the weighted sum of the direct signal each antenna receives

$$(\mathbf{M}_0)_{jk} = -m_a\frac{c}{r_{jk}\nu_0}(1-m_d|\cos(\phi_{jk})|)e^{-i2\pi r_{jk}\nu_0/c}, \quad (25)$$

$$(\mathbf{M}_0)_{jj} = 1, \quad (26)$$

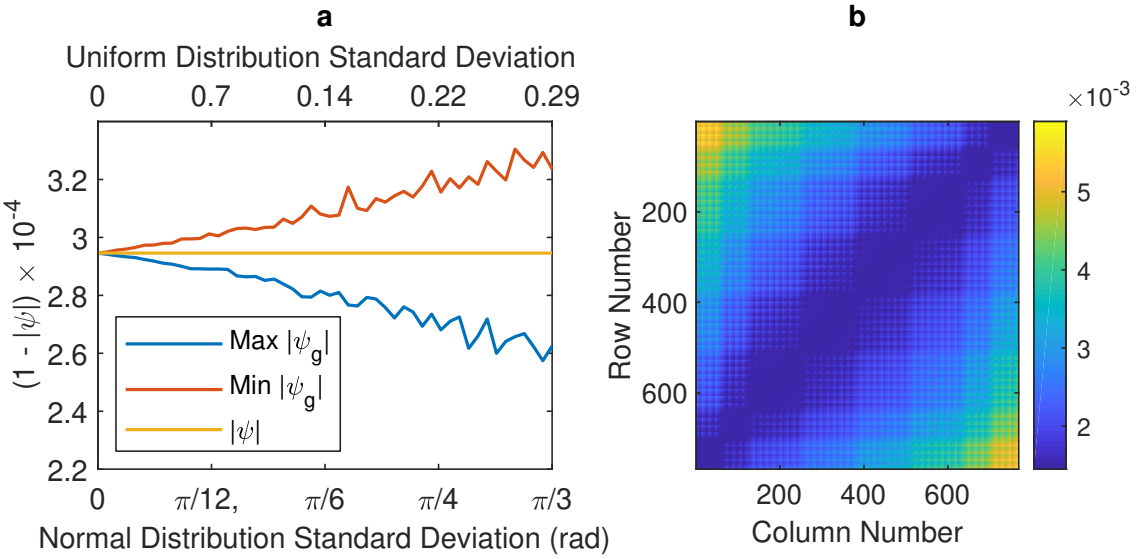

Fig. 4. **(a)** Plots of $1 - |\psi_g|$ where the maximum and minimum value of $|\psi_g|$ was found for a 1000 realizations as a function of the distributions' standard deviations, used to generate $\mathbf{g}$. **(b)** Highest percentage error of the non-narrowband factor (see Eq. (22)) for each element in the covariance matrix $\mathbf{R}_{1g}$. A 1000 realizations were generated where the normal distribution and uniform distribution had a standard deviation of $\pi/3$ and 0.29, respectively (the worst case).

where

m_a is the proportionality constant which determines the strength of the coupling,
r_{jk} is the distance between the j^{th} and k^{th} antenna,
m_d is a directivity parameter,
ϕ_{jk} is the orientation of the line-of-sight between j^{th} and k^{th} antenna.

The initial superposition of signals will be re-radiated by each antenna, which will induce (albeit weaker) signals in each antenna, which will in turn be again re-radiate, and so forth. To describe this iterative process the following infinite sum can be used

$$\mathbf{M} = \mathbf{I} + \sum_{i=1}^{\infty} (\mathbf{M}_0 - \mathbf{I})^i. \tag{27}$$

This series will converge if $\mathbf{M}_{0,jk} << 1$. The mutual coupling matrix $\mathbf{M}$ should be scaled so that the total power is conserved, that is $\text{Tr}(\mathbf{R}) = \text{Tr}(\mathbf{MRM}^H)$.

In Wijnholds (2008) values of $m_a = 0.07$ and $m_d = 0.9$ are found to give good qualitative results compared to full-EM simulations for the LOFAR HBA. Simulating the effect of m_a and m_d on the eigenvalues and eigenvectors revealed that m_d has very little effect compared to m_a. Therefore, m_d was fixed at 0.9 and m_a was varied between 0 and 0.085. The value of m_a cannot be increased above 0.085, because Eq. (27) then no longer converges in the case of a LOFAR HBA. For the simulation six different cases were considered:

- **Ideal**: no complex gain errors or mutual coupling,
- **Uncal**: the covariance matrix is uncalibrated and there is no mutual coupling,
- **MC**: mutual coupling is present and there are no complex gain errors,
- **MC Uncal**: mutual coupling is present and the covariance matrix is uncalibrated,
- **Cal**: there are complex gain errors that have been calibrated,
- **MC Cal**: mutual coupling is present and complex gain errors have been calibrated.

In figures 5a and b the effect of m_a on the first and second eigenvalues are shown. For the first eigenvalue, in figure 5, the three lines where mutual coupling is present, **MC**, **MC Uncal** and **MC Cal**, all monotonically decrease with m_a. As the first eigenvalue decreases, the second eigenvalue increases in figure 5b. In addition, for the cases where unknown complex gains are present, the first eigenvalue is smaller than the first

eigenvalue of the **Ideal** case and the second eigenvalue is larger than the second eigenvalue of the **Ideal** case. Therefore, an increase in mutual coupling and unknown complex gains causes decorrelation in the signal. Even with the calibration step, the power of the first eigenvector is not completely recovered. The reason for this is that the LOFAR HBA station RS407 consists of 48 tiles with 16 antennas, each of which is analogue beamformed and only one gain solution per tile can be calculated with the recorded data.

In figure 6a the cosine similarity between the first eigenvector of the **Ideal** case and all the other cases' eigenvectors is shown as a function of m_a. The same is done for the second eigenvector in figure 6b. In figures 6a and b the cosine similarities decrease as m_a increases. The largest effect however, is caused by the unknown complex gains.

The most realistic case is **MC Cal** where there are complex gains as well as mutual coupling and a calibration step is applied. The largest error between the first eigenvalue of **Ideal** and **MC Cal** is 5×10^{-5} which is lower than all the values of the second eigenvalues. The cosine similarity between **Ideal** and **MC Cal** is one. Therefore, the effect of mutual coupling on the first eigenvalue and eigenvector is minimal. However, the effect of mutual coupling and gain calibration is relatively more pronounced on the second eigenvalue and eigenvector. This is because the gain calibration procedure outlined in section 4 provides only a rank one solution $\mathbf{g}\mathbf{g}^H$, using only the first eigenvalue and eigenvector pair, while the mutual coupling matrix $\mathbf{M}$ has full rank. The effect of mutual coupling is therefore included in the evaluation of the proposed algorithms in section 7.

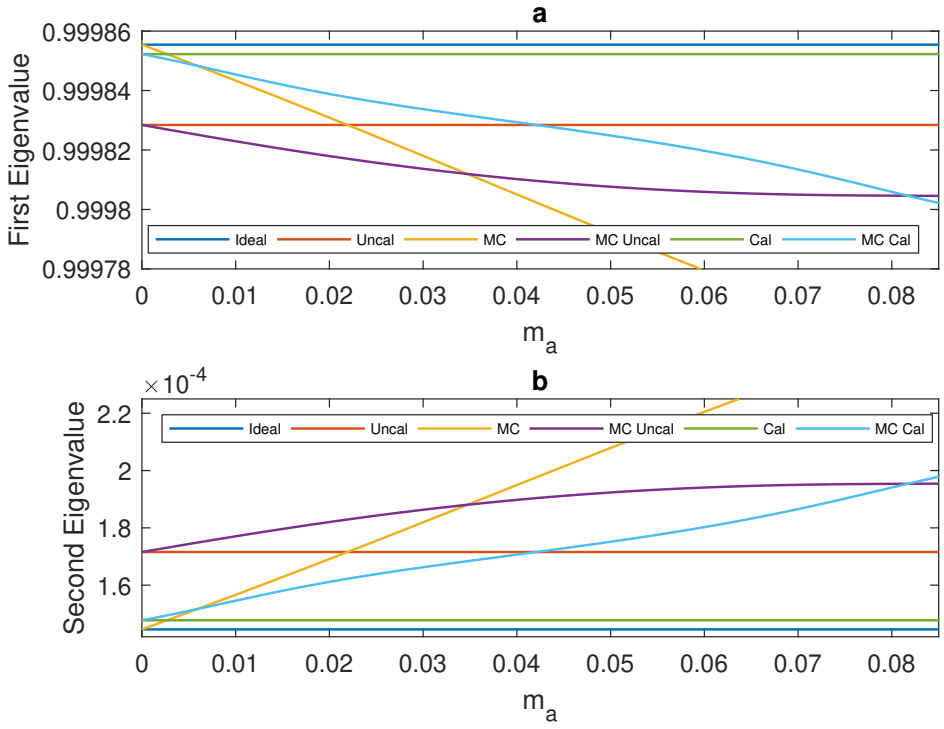

Fig. 5. **Ideal**: no complex gain errors or mutual coupling. **Uncal**: the covariance matrix is uncalibrated and there is no mutual coupling. **MC**: mutual coupling is present and there are no complex gain errors. **MC Uncal**: mutual coupling is present and the covariance matrix is uncalibrated. **Cal**: there are complex gain errors that have been calibrated. **MC Cal**: mutual coupling is present and complex gain errors have been calibrated. Figures **(a)** and **(b)** show the first and second eigenvalues, respectively, as a function of the proportionality constant m_a for different array conditions. The three horizontal straight lines **Ideal**, **Uncal** and **Cal** have no mutual coupling, therefore $m_a = 0$. All matrices have been normalized such that $\mathrm{Tr}(\mathbf{R}) = 1$.

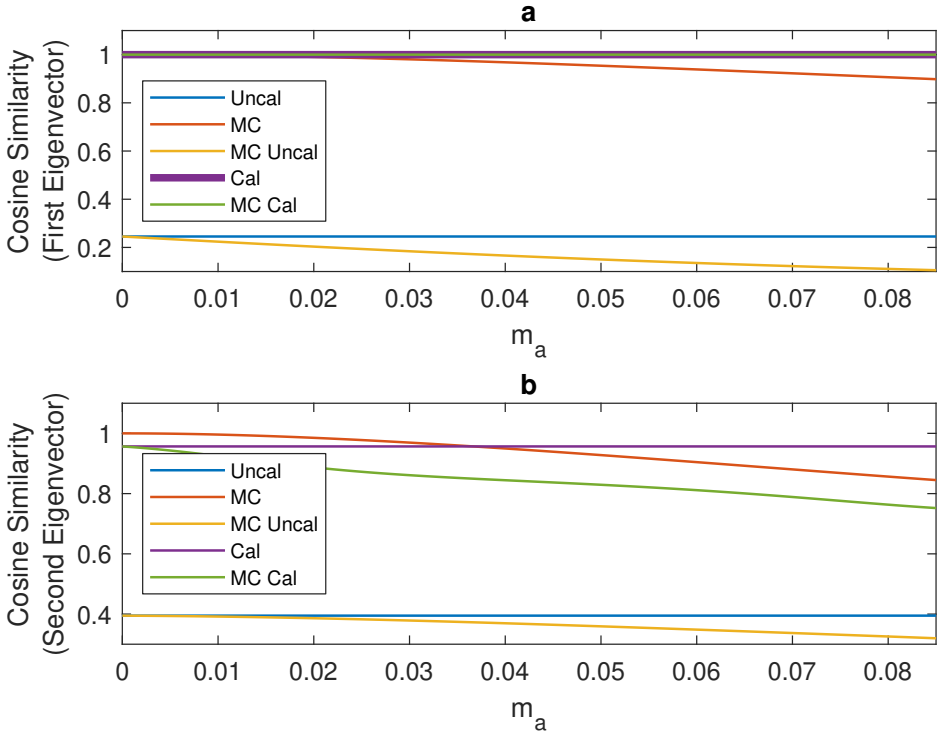

Fig. 6. See figure 5 for definitions of the legend notation. Figure **(a)** shows the cosine similarity between the first eigenvector of the **Ideal** case (no complex gain errors or mutual coupling) and different array conditions as a function of the proportionality constant m_a. Similar to figure **(a)**, figure **(b)** considers the second eigenvector. The three horizontal straight lines **Ideal**, **Uncal** and **Cal** have no mutual coupling, therefore $m_a = 0$. A cosine similarity of 1 indicates that the two vectors are parallel, while a cosine similarity of 0 indicates that the vectors are orthogonal.

6. Proposed RFI Mitigation Algorithms

The two spatial RFI mitigation algorithms based on subspace subtraction presented in Steeb *et al.* (2018) are extended by adding a gain calibration step. These algorithms are designed for wideband RFI which is stationary, such as DAB broadcasts. The channel bandwidth should be selected such that the second eigenvalue of the sample covariance matrix $\widehat{\mathbf{R}}$ is lower or equal to the power of the cosmic sources being observed. The first algorithm is based on the flat frequency response model with unknown complex gains (see Eq. (23)) and the other on Zatman's approximation to that model (see Eq. (24)). The following preprocessing steps are required (see figure 7 for an activity diagram of the preprocessing stage):

- Obtain the location of the RFI source, (l, m, n). For example, the location of DAB towers are fixed and can be easily obtained from relevant authorities. Algorithms such as MUSIC or ESPRIT can also be used, however this will bias the gain calibration step.
- Use the power iteration method on $\widehat{\mathbf{R}}$ to find the largest eigenvalue s_1 with the accompanying eigenvector $\mathbf{v}_1$.
- Estimates for the two largest eigenvalues of the RFI-only covariance matrix can be obtained by using the estimated location of the RFI and Eq. (11)

$$s_{\mathrm{r}1} = s_1 - \frac{\mathrm{Tr}(\widehat{\mathbf{R}}) - s_1}{N_{\mathrm{e}} - 1}, \tag{28}$$

$$s_{\mathrm{r}2} = s_{\mathrm{r}1}\left(\frac{1 - |\psi|}{1 + |\psi|}\right). \tag{29}$$

  Use these two new eigenvalue estimates to create the matrix $\mathbf{S}_{\mathrm{r}} = \mathrm{diag}([s_{\mathrm{r}1}, s_{\mathrm{r}2}]^T)$.
- An algorithm such as StEFCal can be used to calculate the complex gains in $\mathbf{g}$.

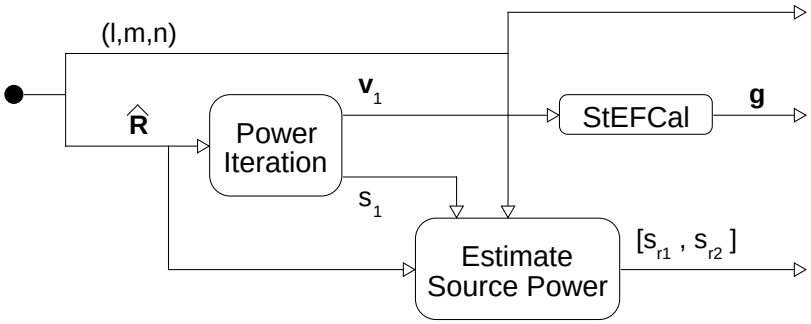

Fig. 7. Activity Diagram of the Preprocessing stage.

Algorithm 1: Flat frequency response model based algorithm (see figure 8a for activity diagram)

- Calculate the complex gains' distorted normalized flat frequency covariance matrix model of the RFI source $\mathbf{R}_{\text{fg}}$, using Eq. (23). Note that this model's covariance matrix does not include any noise and that $\sigma_{\text{s}}^2 = 1$.
- Use the power iteration method on $\mathbf{R}_{\text{fg}}$ to find the second largest eigenvalue's eigenvector $\mathbf{v}_{2\text{fg}}$.
- Apply subspace subtraction to obtain the flat frequency model based RFI mitigated covariance matrix

$$\widehat{\mathbf{R}}_{\text{mf}} = \widehat{\mathbf{R}} - [\mathbf{v}_1, \mathbf{v}_{2\text{fg}}]\mathbf{S}_{\text{r}}[\mathbf{v}_1, \mathbf{v}_{2\text{fg}}]^H. \tag{30}$$

Algorithm 2: Zatman's approximation based algorithm (see figure 8b for activity diagram)

- Calculate the normalized Zatman's approximation based model eigenvector $\mathbf{v}_{2\text{zg}}$ using Eq. (24).
- Apply subspace subtraction to obtain the Zatman's model based RFI mitigated covariance matrix

$$\widehat{\mathbf{R}}_{\text{mz}} = \widehat{\mathbf{R}} - [\mathbf{v}_1, \mathbf{v}_{2\text{zg}}]\mathbf{S}_{\text{r}}[\mathbf{v}_1, \mathbf{v}_{2\text{zg}}]^H. \tag{31}$$

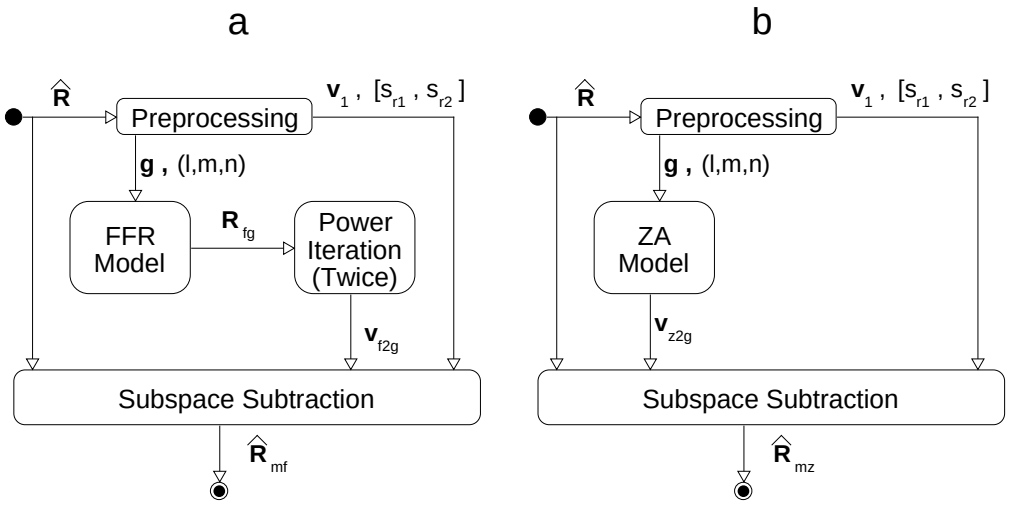

Fig. 8. **(a)** Activity diagram for algorithm 1 which uses the flat frequency model in Eq. (23). **(b)** Activity diagram for algorithm 2 which uses the Zatman's approximation in Eq. (24).

7. Evaluation of RFI Mitigation Algorithms

To evaluate the performance of both proposed algorithms, an estimated covariance matrix was created by adding an estimated noise and cosmic source covariance matrix $\widehat{\mathbf{R}}_{\text{cn}}$ to an estimated RFI covariance matrix $\widehat{\mathbf{R}}_{\text{r}}$. The matrix $\widehat{\mathbf{R}}_{\text{cn}}$ was obtained from a real observation done with LOFAR HBA station RS407 (see figure 9a) where there is no RFI present. A software defined radio was used to record a DAB signal with the power spectrum as shown in figure 9b which has a reasonably flat frequency spectrum. Finite impulse response filters were used to produce 300 signals with bandwidths ranging from 763 Hz to 218 kHz. Each filtered signal was used to generate a delayed signal for each antenna in the array (768 antennas). The delay was added by computing the fast Fourier transform of the filtered signal and multiplying each frequency component with the appropriate delay and then computing the inverse fast Fourier transform. For each bandwidth a covariance matrix was created (with an integration time of 1.5 s) and reduced from a 768×768 matrix to a 48×48 matrix by beamforming groups of 16 antennas. The effect of complex gains and mutual coupling is applied before the beamforming step.

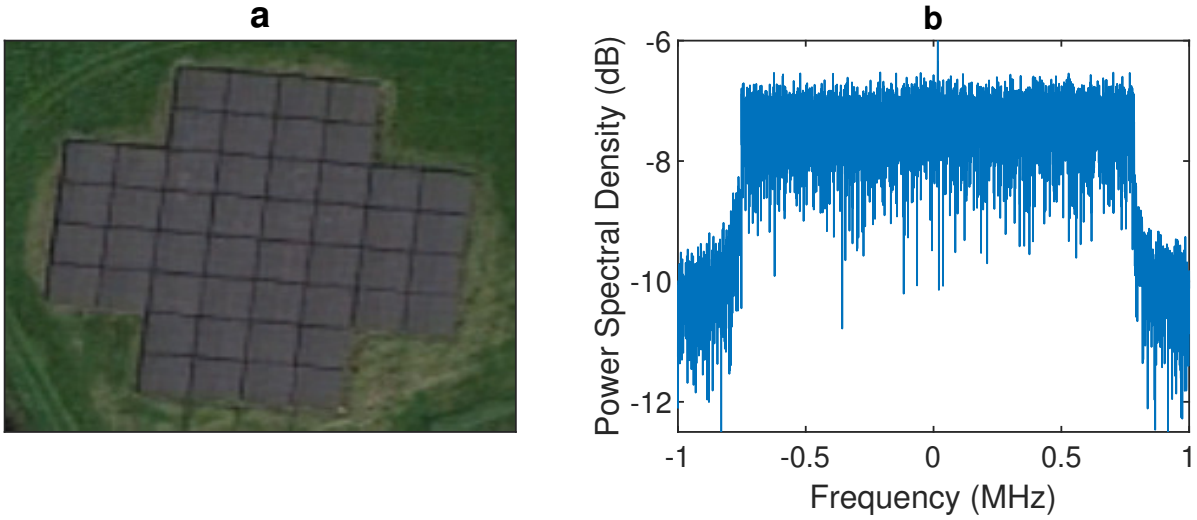

Fig. 9. **(a)** Satellite image of LOFAR HBA station RS407. **(b)** Power spectral density of a DAB signal measured with a software defined radio.

To measure the performance of the proposed algorithms, the Covariance Matrix Distance (**CMD**, see Herdin *et al.* (2005)) and the Attenuation (**ATT**) are used

$$\mathbf{CMD} = 1 - \frac{\text{Tr}(\widehat{\mathbf{R}}_{\text{cn}}\widehat{\mathbf{R}}_{\text{m}})}{\left\|\widehat{\mathbf{R}}_{\text{cn}}\right\|_F \left\|\widehat{\mathbf{R}}_{\text{m}}\right\|_F}, \tag{32}$$

$$\mathbf{ATT} = 10 \log \left[\frac{\text{Tr}(|\widehat{\mathbf{R}}_{\text{m}} - \widehat{\mathbf{R}}_{\text{cn}}|_{\odot})}{\text{Tr}(\widehat{\mathbf{R}}_{\text{r}})} \right], \tag{33}$$

where $\widehat{\mathbf{R}}_{\text{m}}$ is the recovered matrix. The **CMD** and **ATT** measure, respectively, how well the eigenvectors and eigenvalues of $\widehat{\mathbf{R}}_{\text{cn}}$ are recovered. If the **CMD** is zero, then the matrices are equal up to a scaling factor. At negative infinity the **ATT** indicates that the total power (sum of eigenvalues) for $\widehat{\mathbf{R}}_{\text{m}}$ and $\widehat{\mathbf{R}}_{\text{cn}}$ are the same.

To test the effect of unknown complex gains the generated values for $\mathbf{g}$ in section 4 were used as well as $\widehat{\mathbf{R}}_{\text{r}}$ and $\widehat{\mathbf{R}}_{\text{cn}}$ at a fixed bandwidth of 195 kHz. In figures 10a and b, respectively, the **CMD** and **ATT** are plotted for three different cases as a function of the normal and uniform distributions' standard deviations. The 1st order lines are the performance achieved by subtracting the estimate of the subspace associated with the largest eigenvalue $\widehat{\mathbf{R}}_{\text{r}}$. Using the **FF Alg** without a calibration step causes the performance to

decline due to an increase in the distributions' standard deviations. Introducing a calibration step greatly improves the performance, but there is still a slightly increasing trend. This is caused by the beamforming stage for the LOFAR HBA station which consists of 48 tiles with 16 antennas, each of which is analogue beamformed and only one gain solution per tile can be calculated. Furthermore, the assumption made in section 4 that the complex gains non-narrowband component of Eq. (22) is minimally affected by the unknown complex gains, adds to the trend.

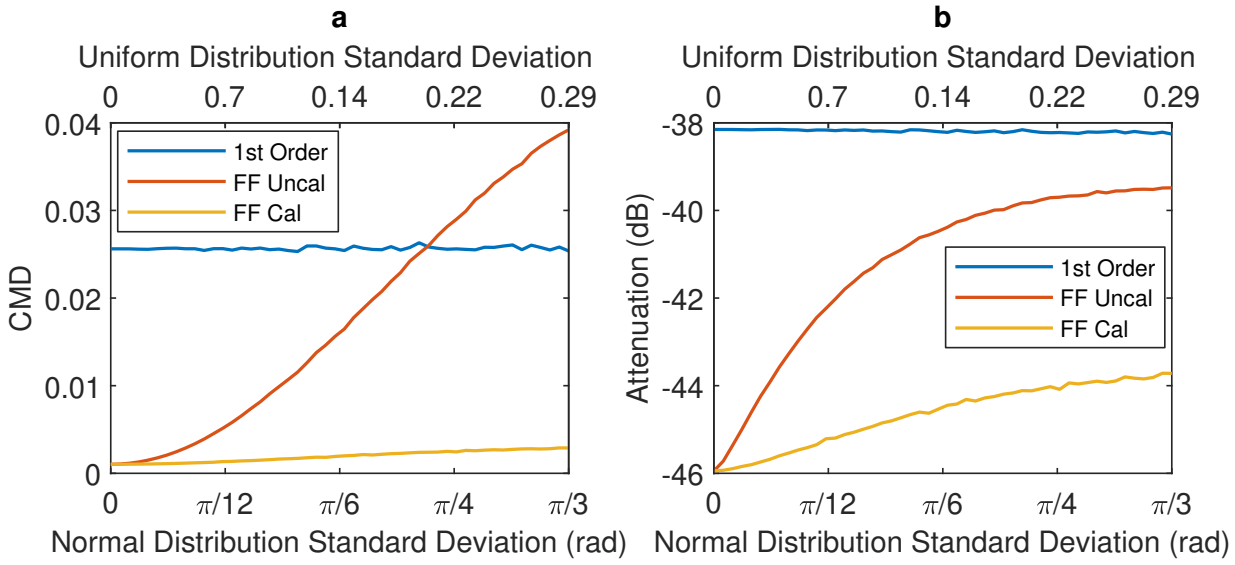

Fig. 10. **1st Order**: Subtracting the estimate of the subspace associated with the largest eigenvalue of $\widehat{\mathbf{R}}_{\mathrm{r}}$ from $\widehat{\mathbf{R}}_{\mathrm{cn}}$. **FF Uncal**: Using the Flat Frequency Algorithm without a calibration step. **FF Cal**: Using the Flat Frequency Algorithm with a calibration step. In figure **(a)** the covariance matrix distance and in figure **(b)** the attenuation is plotted for three RFI mitigation methods as a function of the distributions' standard deviations, used to generate $\mathbf{g}$.

Now the entire set of covariance matrices at different bandwidths are used. The mutual coupling matrix was generated by setting $m_a = 0.07$ and $m_d = 0.9$ and the unknown complex gains were generated using a uniform distribution (standard deviation 0.29) for the magnitude and a normal distribution (standard deviation $\pi/3$) for the phase (only one set of complex gains was used). In figures 11a and b the performances of four algorithms are given:

- **1st Order**: Subtracting the estimate of the subspace associated with the largest eigenvalue of $\widehat{\mathbf{R}}_{\mathrm{r}}$ from $\widehat{\mathbf{R}}_{\mathrm{cn}}$.
- **2nd Order**: Subtracting the estimate of the largest and second largest eigenvalue of $\widehat{\mathbf{R}}_{\mathrm{r}}$ and the accompanying eigenvectors from $\widehat{\mathbf{R}}_{\mathrm{cn}}$.
- **FF Alg**: Using the Flat Frequency Algorithm with a calibration step.
- **Zatman Alg**: Using the Zatman's Approximation Based Algorithm with a calibration step.

At close to zero fractional bandwidth, all methods have the same performance, since the estimate of the second eigenvector of $\widehat{\mathbf{R}}_{\mathrm{r}}$ is almost zero and all methods are effectively only subtracting the first subspace. The error for the **2nd Order** increases until a fractional bandwidth of approximately 8×10^{-4}. This is due to eigenvalue decomposition that cannot differentiate between the second eigenvector of $\widehat{\mathbf{R}}_{\mathrm{r}}$ and the noise. After a fractional bandwidth of 8×10^{-4}, the **2nd Order** method's performance improves, however it does not reach the same level of performance achieved at smaller fractional bandwidths. This is caused by the third eigenvalue that becomes significant due to the bandwidth and the non-perfectly flat spectrum of the signal. For all bandwidths the **FF Alg** and **Zatman Alg** methods have the same performance and both have superior **CMD** performance to the **1st Order** and **2nd Order** subtraction methods until approximately a fractional bandwidth of 11×10^{-4}. For the **ATT** performance the **FF Alg**

and **Zatman Alg** methods have superior performance for the entire fractional bandwidth considered.

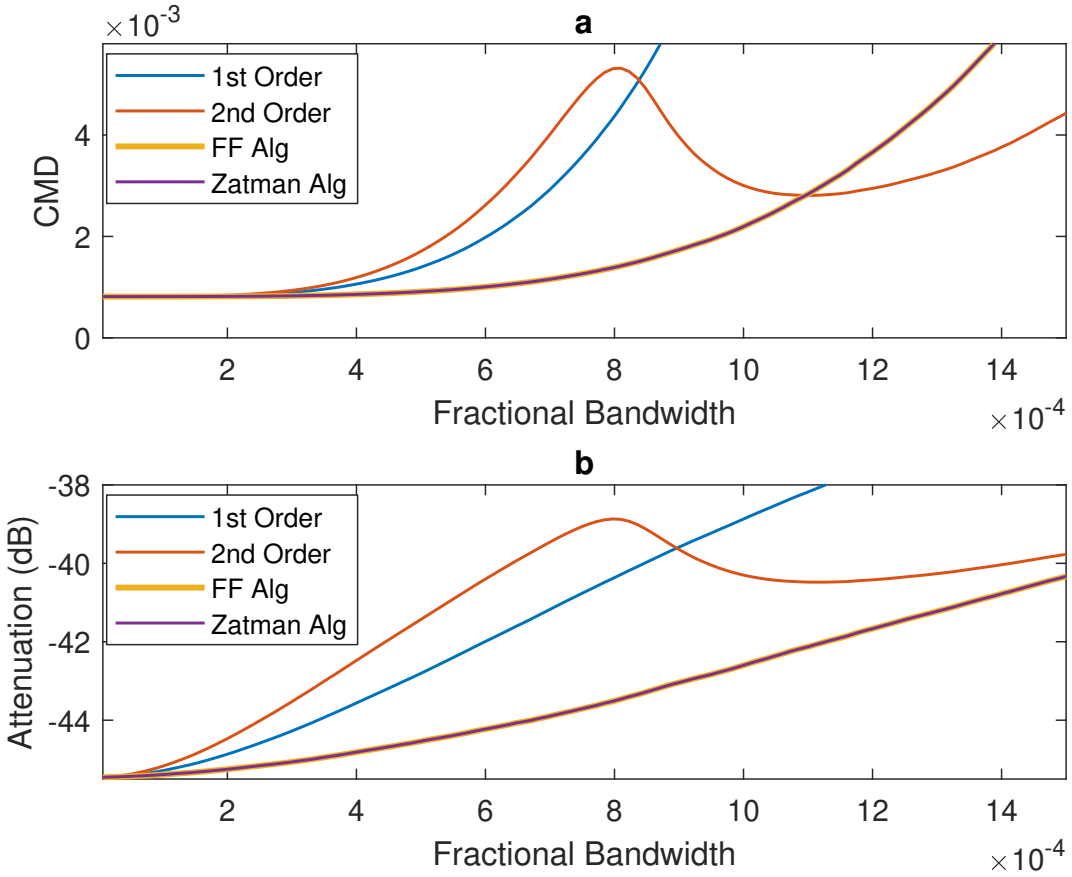

Fig. 11. **1st Order**: Subtracting the estimate of the largest eigenvalue of $\widehat{\mathbf{R}}_{\mathrm{r}}$ and its accompanying eigenvector from $\widehat{\mathbf{R}}_{\mathrm{cn}}$. **2nd Order**: Subtracting the estimate of the largest and second largest eigenvalue of $\widehat{\mathbf{R}}_{\mathrm{r}}$ and the accompanying eigenvectors from $\widehat{\mathbf{R}}_{\mathrm{cn}}$. **FF Alg**: Using the Flat Frequency Algorithm with a calibration step. **Zatman Alg**: Using the Zatman Approximation Based Algorithm with a calibration step. In figures **(a)** and **(b)** the covariance matrix distance and attenuation, respectively, for four RFI mitigation methods as a function of fractional bandwidth are plotted.

Channels with larger bandwidth can be processed using the **FF Alg** or **Zatman Alg**, while achieving the same level of mitigation as the 1st order method which requires channels with smaller bandwidth. This is shown in figure 12 where the bandwidth required by **FF Alg** is given as a function of the bandwidth of the **1st Order** method. When no array imperfections are present, approximately six times as much bandwidth can be processed. When unknown complex gains are present and a calibration step is added, the performance reduces to twice as much bandwidth. Finally, if mutual coupling is also present the performance reduces further to 1.6 times more bandwidth.

In the simulations completed, both **FF Alg** and **Zatman Alg** provide the same results for mitigation. However, the **Zatman Alg** is slightly computationally less expensive, because unlike **FF Alg** it does not have to complete the power iteration method twice (see figure 7a and b). See Steeb *et al.* (2018) for the computational complexity analysis.

8. Conclusion

The proposed algorithm extends a previously developed algorithm that now includes a gain calibration step. The algorithm combines a first order subspace subtraction filter and a non-narrowband signal model, that may be used to mitigate powerful RFI signals for which the second eigenvalue is below the noise, but which has a power that is competing with the astronomical sources. Array imperfections such as unknown

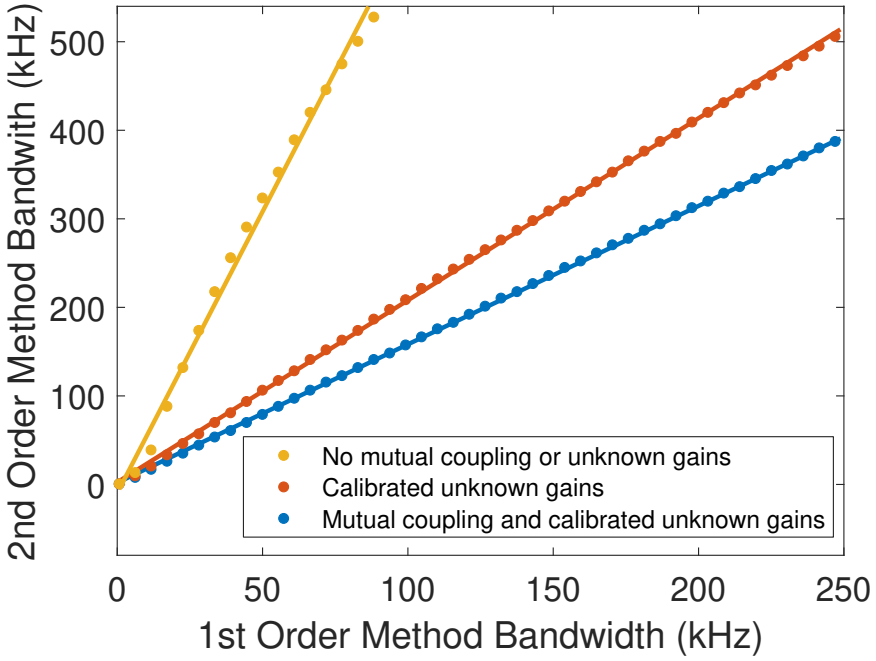

Fig. 12. A plot of the bandwidth required by the **FF Alg** as a function of the bandwidth of the **1st Order** method to achieve the same attenuation for three cases: there is no mutual coupling or unknown gains, there are unknown gains that have been calibrated for and finally unknown gains that have been calibrated for and mutual coupling.

complex gains and mutual coupling reduce the performance of the algorithm. It was shown that a standard gain calibration step can be applied to improve performance, since the non-narrowband factor is minimally affected by the complex gains. With a gain calibration step and no mutual coupling the proposed algorithm was able to process twice the bandwidth per channel that can be processed when applying conventional narrowband techniques. This performance declines to 1.6 times more bandwidth when the effect of mutual coupling is included.

9. Acknowledgements

This work was funded and supported by the South Africa Radio Astronomy Observatory, the South African Research Chairs Initiative of the Department of Science and Technology, the National Research Foundation of South Africa, and the Netherlands Organisation for Scientific Research.

References

Boonstra, A. J. [2005] *Radio Frequency Interference Mitigation in Radio Astronomy*, PhD Thesis, Delft University of Technology, uuid:caa1942c-4180-4a17-88db-cec359490aad.

Bridle, A. H., Schwab, F. R. [1999] *Bandwidth and Time-Average Smearing*, In G. B. Taylor, C. L. Carilli and R. A. Perley, editors, "Synthesis Imaging in Radio Astronomy II," **180**, 18, p. 371–382, eISBN: 978-1-58381-516-8.

Brossard, M., El Korso, M. N., Pesaventoc, M.,Boyer, R., Larzabal, P., Wijnholds, S.J. [2018] *Parallel multi-wavelength calibration algorithm for radio astronomical arrays*, Signal Processing, **145**, p. 258–271, April 2018, doi:10.1016/j.sigpro.2017.12.014.

de Gasperin, F., Mevius, M., Rafferty, D. A., Intema, H. T., Fallows, R. A. [2018] *The effect of the ionosphere on ultra-low-frequency radio-interferometric observations*, Astronomy & Astrophysics, **615**, no. A179, July 2018, doi:10.1051/0004-6361/201833012.

Herdin, M., Czink, N., Ozcelik, H., Bonek, E. [2005] *Correlation Matrix Distance, a Meaningful Measure for Evaluation of Non-Stationary MIMO Channels*, IEEE 61st Vehicular Technology Conference, Stockholm, Sweden, doi:10.1109/VETECS.2005.1543265.

Johnson, D. H., Dudgeon, D. E. [1993] "Array Signal Processing: Concepts and Techniques," NJ: Prentice-Hall, p. 113–115.

Salvini, S., Wijnholds, S. J. [2014] *Fast gain calibration in radio astronomy using alternating direction implicit methods: Analysis and applications*, Astronomy & Astrophysics, **571**, p. 1–14, doi: 10.1051/0004-6361/201424487.

Sardarabadi, A. M. [2016] *Covariance Matching Techniques for Radio Astronomy*, PhD Thesis, Delft University of Technology, doi:10.4233/uuid:3eb46b5b-126c-4d95-8821-fb71ce404cac.

Steeb, J. W., Davidson, D. B., Wijnholds, S. J. [2018] *Mitigation of Non-Narrowband Radio Frequency Interference*, submitted to Radio Science Bulletin.

van der Tol, S., van der Veen, A. [2005] *Performance Analysis of Spatial Filtering of RF Interference in Radio Astronomy*, IEEE Transactions on Signal Processing, **53**, 3, p. 896–910, doi:10.1109/TSP.2004.842177.

van der Veen, A., Leshem, A., Boonstra, A. [2004] *Signal Processing for Radio Astronomical Arrays*, Procceedings of the Sensor Array and Multichannel Signal Processing Workshop, p. 1–10, doi:10.1109/SAM.2004.1502901.

van Haarlem, M. P., *et al.* [2013] *LOFAR: The Low Frequency Array*, Astronomy & Astrophysics, **556**, A2, p. 1–53, doi:10.1051/0004-6361/201220873.

Wijnholds, S. J. [2008] *Mutual Coupling, Inter-tile Spacing and Inter-station Rotation in the HBA Array*, Technical Report, LOFAR-ASTRON-MEM-245.

Zatman, M. [1998] *How narrow is narrowband?*, IEE Proceedings-Radar, Sonar and Navigation, **145**, 2, p. 85–91, doi:10.1049/ip-rsn:19981670.